# Lurking in ULIRGs:

# Molecular Gas in local Merging Galaxies

Thesis by

Swarnima Manohar

In Partial Fulfillment of the Requirements

for the Degree of

Doctor of Philosophy


California Institute of Technology

Pasadena, California

2016

(Defended January 12, 2016)

# Acknowledgments

Studying astronomy had always been a dream that finally came true when I was accepted to Caltech. A place that has been the home of many great astronomers; astronomers who set the standard, who discovered and invented and changed the face of the field. It has been a privilege to walk its corridors.

None of this would have been possible without the encouragement and motivation of my wonderful advisor Nick Scoville. Nick, your patience, your deep knowledge of all things astronomy and your absolute enjoyment of the subject have made my graduate career an incredible one. I have learned so much from you. Thank you for guiding and motivating me through all of this.

There is another faculty member here at Caltech who I would like to thank. Anneila Sargent has been a very important influence in my time here. I have interacted with her as a student, as a TA, as a graduate RA, as a scientist. From her I have learned to be a teacher and an educator, a mentor. I have learned to listen, to be patient, learned how to lead, how to be a scientist and how to be endlessly charming, cheerful and optimistic. While our conversations have been limited, but she has always listened and has always been very supportive.

My time at Caltech has been unbelievably fabulous because of the many amazing people I had the opportunity to meet here. My classmates Shriharsh, Ryan and Dmitriy made our first year such an enjoyable experience. We had some good times in that dungeon we called our office in our first year.

I had the best officemates, some of who might have questioned my sanity when I talked to plants. Ryan, Tucker, Anne-Marie, Matt, Trevor, Marin and Katie. I have had some of the most entertaining conversations with you, about conspiracy theories, and cats, and aliens, and really everything. I enjoyed coming to work everyday because I always had so much fun with you all.

I also had some pretty fabulous mentors who were my seniors here at Caltech. Mansi, Varun, Elisabeth, Laura and Matthew, your wisdom and encouragement have been invaluable. And how can I forget my juniors who have all taught me something about myself: Coco, Jackie, Sebastian, Mike, Sirio, Becky, Marta, Michael, Allison, Gina, Donal, Jake, Yi, Nicha, Rachel, Melodie and all others. All of you are absolutely amazing.

I met some pretty amazing people here at Caltech, both within the department and outside. Shriharsh, Varun, Abhilash, Kartiki, Teja and Pinkesh, we have had many exploits together. You

have cheered me, supported me, debated with me, endured my OCD and accepted me just as I am. Thank you for being such fabulous friends.

It was not only the students and professors who made my time in Caltech so marvelous. I would be remiss if I did not thank our very lovely administrators Gita, Gina, Althea and Sandy. Then there are Patrick and Anu who really saved the day after the debacle that was my computer. Thank you for answering emails on January 1st when I was hyperventilating and trying to print a poster. I must also thank Efrain Hernandez with who I had some of the most philosphical discussions at Caltech.

In the time at Caltech, I have also had the fantastic opportunity to work as an RA and to be a member of the Graduate Honor Council. I was exposed to new ideas, met incredible people and made new friends. I first met Felicia Hunt in her capacity as the Director of the Women's Center and not long after that she became the Associate Grad Dean. Working with her as an RA was a very fulfilling experience. She has been a true advocate of grad students at Caltech. Her compassion and patience has made the grad experience for a lot of people a much better one, including mine. I want to thank Larissa, Taso, Suzzane, Devin, Dorothy, Beau, Corey, Wendy and Christine. It was truly a pleasure to work with all of you and I learned something about myself from the whole experience. I also want to thank the past and current members of the GRB/GHC, who all came from varied fields at Caltech. We had many delightful and thoughtful discourses about ethics and law. The conversations always made me evaluate my stance on multitude of topics and definitely made me a better scientist and colleague.

The CARMA observatory, which unfortunately is no more, was an unparalleled teaching ground for me. I spent many weeks there. The people and the place both hold a dear spot in my heart. Every trip to CARMA was a learning experience. The beauty of the 23 antennas atop the mountain was truly enthralling. While the beautiful view is no more, I will always cherish the memory and be thankful that I got to experience it.

Through the years, I have had many truly amazing teachers who have instilled the love of learning in me and who took the time to answer my endless questions. I like to thank my high school teachers Mrs. Mulla, Mr. Dhaiya and Mr. Narayanan who taught with grace and passion everyday in the face teenage indifference. My undergraduate professors, both in the Physics and Astronomy Department and the Aerospace Engineering Department at USC, fostered my interest in many subjects and encouraged me to reach higher and do better. I would like to thank Prof. Erwin, Prof. Dravinski, Prof. Pierpaoli, Prof. Rhodes, Prof. Kunc and Prof. Pilch, who all made learning so much fun. I would especially like to thank Prof. Gene Bickers who championed me and mentored me in my time at USC and who had complete faith in me being the next Caltech graduate student. I hope that some day I can be a truly good teacher like you.

I met my closest friends Chinmayi and Lara at very different stages of my life. We are so very

different from each other and yet we have always made each other laugh. That laughter has carried us through so much. I can only hope you gained as much from our friendship as I did.

Last but most importantly I want to thank my very awesome family. My family has been through this all with me. Mom and dad, your unfailing love and unconditional support have sustained me through many adventures and rough patches. You have nurtured my love of astronomy from the very day the 9-year-old me wrote an essay expressing my ambition to be an astronomer. I could not have done this without you.

My sister, Anubhuti has always been a great source of inspiration for me and I have always looked up to her. She has motivated me and pushed me to be the very best, always. Didi, you have listened, you have cheered, you have prodded and you have scolded. You truly are the very best sister anyone could ever hope to have.

Although my grandmother is not here with us anymore to see me finish my Ph.D. as she had always hoped to, this section would not be complete without me thanking her. She taught me one of the most important lessons ever, to never stop learning. It is a mantra that I carry with me everyday. I do miss you very much, Nani.

To my parents and my sister,

All that I am,

All that I have achieved,

Would not have been possible without you.

*It is the chiefest point of happiness that a man is willing to be what he is.*

—*Desiderius Erasmus*

*It is not growing like a tree*
*In bulk doth make Man better be;*
*Or standing long an oak, three hundred year,*
*To fall a log at last, dry, bald, and sere:*
*A lily of a day*
*Is fairer far in May,*
*Although it fall and die that night*
*It was the plant and flower of light.*
*In small proportions we just beauties see;*
*And in short measures life may perfect be.*

—*Benjamin Johnson*

# Abstract

Mergers and interacting galaxies are pivotal to the evolution of galaxies in the universe. They are the sites of prodigious star formation and key to understanding the starburst processes: the physical and chemical properties and the dynamics of the molecular gas. ULIRGs or Ultraluminous Infrared Galaxies are a result of many of these mergers. They host extreme starbursts, AGNs, and mergers. They are the perfect laboratory to probe the connection between starbursts, black hole accretion and mergers and to further our understanding of star formation and merging.

NGC 6240 and Arp 220 can be considered the founding members of this very active class of objects. They are in different stages of merging and hence are excellent case studies to further our understanding about the merging process. We have imaged the dense star-forming regions of these galaxies at sub-arcsec resolution with CARMA C and B Configurations ($2''$ and 0.5 - $0.8''$). Multi-band imaging allows excitation analysis of HCN, $HCO^+$, HNC, and CS along with CO transitions to constrain the properties of the gas. Our dataset is unique in that we have observed these lines at similar resolutions and high sensitivity which can be used to derive line ratios of faint high excitation lines.

Arp 220 has not had confirmed X-ray AGN detections for either nuclei. However, our observations indicate HCN/HNC ratios consistent with the chemistry of X-ray Dominated Regions (XDRs) – a likely symptom of AGN. We calculated the molecular Hydrogen densities using each of the molecular species and conclude that assuming abundances of HNC and $HCO^+$ similar to those in galactic sources are incorrect in the case of ULIRGs. The physical conditions in the dense molecular gas in ULIRGs alter these abundances. The derived $H_2$ volume densities are $\sim 5 \times 10^4$ cm$^{-3}$ in both Arp 220 nuclei and $\sim 10^4$ cm$^{-3}$ in NGC 6240.

# Contents

# List of Figures

# List of Tables

# Chapter 1

# Introduction

The cosmos is brimming with an assortment of active and passive objects. They are all integral to the workings of the universe, therefore, learning about one class adds to our knowledge of the other and about how they co-evolve and interact in this ever-altering universe. An essential part of the active set of objects is what are called Ultra Luminous Infra-Red Galaxies or ULIRGs. These are exotic galaxies that emit as much as 90% of their luminosity in the infrared ($L_{IR} > 10^{12} L_{\odot}$), in comparison to our own galaxy which emits a bolometric luminosity of the order of 2 x $10^{10} L_{\odot}$. These extreme luminosities are caused by enhanced levels of activity: star formation and AGN fueling.

As indicated by the IR luminosity, these galaxies host star formation rates (SFRs) that are boosted by 10-100 times the rates observed in typical disk galaxies. The vigorous starburst activity is probably linked to extraordinary concentrations of gas in the nuclei of the merging systems and/or the dynamical compression of the ISM caused by the merger. These systems often also exhibit elevated AGN activity (Sanders et al., 1988). During the merging process the pre-existing ISM sinks rapidly to the center of the system due to dissipation of kinetic energy in the gas and the torques generated by the offset stellar and gas bars structures (e.g. Barnes & Hernquist, 1992).

The *IRAS* all sky survey was first used to generate a sample of 12 galaxies in the local universe with $L_{IR} > 10^{12} L_{\odot}$ at z< 0.1 and was followed up with ground based optical observations, which demonstrated that almost all galaxies were either merging or post merging (Sanders et al., 1988; Sanders & Mirabel, 1996). These systems were also shown to be very gas rich, with molecular gas masses deduced from CO observations on the order 2–20 x $10^{9} M_{\odot}$ (Sanders et al., 1991).

In the local universe, LIRGs (Luminous Infra-Red Galaxies) and ULIRGs are rare (< 1% of the total galaxy population), exotic objects. For low-z LIRGs, numerous investigations indicate that the majority of the IR luminosity is spatially extended and powered by star formation with clear evidence of galaxy interactions in only $\sim$ 50% of the objects. For ULIRGs, the luminosity is strongly concentrated in the nuclear regions – $\sim$50% show evidence of a luminous AGN and nearly all the objects appear to have undergone a recent merger (Sanders & Mirabel, 1996; Veilleux et al., 2002). At higher redshifts the LIRGs and ULIRGs become much more common and start to dominate the

cosmic star formation rate density at z > 0.7 (e.g., Le Floc'h et al. 2005). At still higher redshifts (z > 1), ULIRGs dominate the overall star formation in the galaxy population (Caputi et al., 2007; Magnelli et al., 2009) and likely play a critical role at the z ∼ 2 peak of SF and AGN activity. Thus, these galaxies are quite the hub of activity with escalated star formation and black hole accretion as well as being in the process of merging, resulting in the assembly of more massive systems.

Evidence of ongoing or recent mergers in a substantial portion of these objects indicates the merger process to be an essential trigger for these energetic and active galaxies. Merging is a key step in the evolution and buildup of galaxies in the universe. Merging is strongly associated/correlated with the most luminous AGN activity and high star formation rates. While the mergers have been studied in detail, both in theory and observations, for a long time, a great deal still has to be determined about the process. The interaction of molecular gas in a merger is an important aspect of what triggers the intense star formation in these systems and thus is crucial to our understanding of galactic merging. An ideal way to study this part of the merging process is to observe such mergers in different stages of the process.

There are many unanswered questions about the merging process of galaxies. Mergers are messy, complicated processes. Understanding the process requires study through varied means. As mergers, starbursts, and black hole accretion are interconnected and co-exist in environments such as ULIRGs, it makes the process of untangling the physical processes in effect in each of these a difficult process. Therefore, a multi-pronged mutli-wavelength approach is the best means to further our understanding of the physical phenomena. There are many questions about the smaller scale molecular gas disk behavior during the merging process.

1. How molecular gas properties (densities, opacities, temperature) evolve with different stages of merger (i.e., time)?
2. How molecular gas properties evolve as function of position and velocity within each merger?
3. How Star formation activity evolves as a function of radius and merger state?
4. Can dense gas be mapped by CO observations alone?
5. Is dense gas clumped or smoothly distributed in the larger structures probed by CO or is it confined to smaller radii?
6. What is the nature of the starburst-AGN connection in mergers?
7. What are the chemical properties of the molecular gas in late-state mergers?

The aim of this thesis is to explore some of these questions through observations of two local merging galaxies. High resolution molecular gas observations are key to answering all of these questions. The molecular gas plays a central role in the merging process: it is the medium that is

most concentrated in the merger nuclei, as it is the fuel for star formation and presumably feeds the black hole accretion. Therefore, molecular gas observations of merging galaxies enhance our understanding of the physics of merging galaxies, and the evolution of galaxies. In this thesis, I present imaging of the large scale distribution of molecular gas and the very dense molecular core regions, which are the sites of starbursts in HCN and CS. There are many theoretical models that have been developed as a means to explore our questions about galaxy interactions and star formation. This thesis is dual-minded, in that it uses models to explore the data obtained from the observations and gives back contraints to enhance future models.

Carbon Monoxide or CO has long been the go-to molecular species to probe molecular hydrogen gas in galaxies. Molecular hydrogen, $H_2$, is difficult to study directly, and therefore astronomers have used CO as a proxy for $H_2$. However, CO is not the only choice. We also want to probe the densest molecular regions where the CO emission may saturate, and in this thesis present the first imaging of other molecular species such HCN and CS, which have higher dipole moments and probe this density regime.

In this thesis we are using various molecular species as tracers of the densest $H_2$, which will also probe the varied chemical and physical process that are in effect. While CO will map $H_2$ in general, Hydrogen Cyanide (HCN) will map gas with ∼100 times higher density. Hydrogen Isocyanide (HNC) is expected to probe molecular gas with similar densities as HCN but with different physical processes at play. HCN and HNC can be used to probe the presence of an obscured AGN. Carbon monosulfide (CS) traces high excitation molecular gas while $HCO^+$, some studies indicate, might trace dense gas in starburst driven winds. Isotopomers like $H^{13}CN$ trace densities and temperatures of the most optically thick regions.

A key feature of the observations presented in this thesis is the fact that all of the different molecular transitions are observed with the same interferometer configurations, similar spectral resolutions, and with simultaneous calibrators. Thus, these data can produce comparable measurements of the emission lines to be used in analyzing the line ratios. Those line ratios provide constraints on the excitation properties of the dense molecular gas and the chemical abundances.

## 1.1 Case Studies: ARP 220 & NGC 6240

To further our understanding of the merging process, I observed and analyzed two well known systems that are in the process of merging. NGC 6240 ($L_{IR} \sim 10^{11.9} L_\odot$) & Arp 220 ($L_{IR} \sim 2$ x $10^{12} L_\odot$) are often viewed as the prototypical ULIRGs, albeit at slightly different stages of merging. The relative proximity of these galaxies in addition to the abundance of their observations in many wavelength regimes makes them the perfect case studies. Both these objects show signs of AGN activity and high levels of star formation and are in the late stages the merging process.

Arp 220 is the quintessential ULIRG with $L_{IR} \sim 2 \times 10^{12} L_\odot$ and apparent V magnitude of ∼13.9 mag. It is in the Serpens constellation, only about 77 Mpc away (z = 0.0181). Near infrared imaging of Arp 220 reveals two nuclei (see Fig. 1.1) separated by 1″ (projected distance of 300pc) and one of these has recently been detected in X-rays (Iwasawa et al., 2005). The west nucleus shows greatly increased extinction to the south and has been modeled as a dense dust disk tilted to the line of sight (Scoville et al., 1998).

CO imaging at 0.5″ resolution detected counter-rotating disks in both nuclei with radii ∼ 100 pc, and dynamical masses of 2 x $10^9 M_\odot$ for each and ∼ 50% gas mass fractions in the nuclei (Scoville et al., 1997; Sakamoto et al., 1999; Downes & Eckart, 2007). Much of the nuclear disk ISM is very dense ($> 10^{4-5} cm^{-3}$) and highly excited (T > 75K), based on the strong HCN & $HCO^+$ line emission and high CO brightness and dust color temperatures (Greve et al., 2009; Downes & Eckart, 2007). The inferred visible extinctions perpendicular to the disks are $A_V \sim$ 500-2000 mag, precluding the use of optical/near infrared tracers of the star formation in the nuclei. Near Infrared integral field spectroscopy of Arp 220 indicates a starburst population less than 10 Myr old (Tecza et al., 2000; Engel et al., 2010, 2011) and ∼200 star clusters are seen (Wilson et al., 2006). Its SFR is estimated to be about ∼ 240 $M_\odot$/yr from its infrared luminosity (Anantharamaiah et al., 2000; Beswick et al., 2001; Sanders et al., 2003).

NGC 6240 is located within the constellation Ophiuchus. It is a bit further at 101 Mpc (z = 0.0245) than Arp 220. With a $L_{IR} \sim 10^{11.9} L_\odot$ and an apparent V Magnitude 12.8 mag, it is a bright galaxy both optically and in the IR.NGC 6240 exhibits two clearly separated nuclei (see Fig. 1.3) ∼ 2″(about 500pc) apart, both showing a hard X-ray source AGN (Komossa et al., 2003) with high reddening in the region between them.

The major gas concentration lies between the two nuclei in the overlap region (Tacconi et al., 1999; Scoville et al., 2000; Engel et al., 2010). NGC 6240 exhibits a highly disturbed structure, including extensions and loops, indicating a complex coalescing of the molecular gas from the merging galaxies. The gas concentration between the nuclei can be modelled as a rotating disk with dynamical mass 7 x $10^9 M_\odot$ and molecular gas mass fraction ∼ 50% (Tacconi et al., 1999). Near infrared spectroscopy of the starlight in NGC 6240 indicates a starburst population less than 20 Myr old (Tecza et al., 2000; Engel et al., 2010). Its SFR has been estimated to be ∼ 100 $M_\odot$/yr from the far infrared luminosity (Anantharamaiah et al., 2000; Beswick et al., 2001; Sanders et al., 2003).

### 1.1.1 Arp 220 vs NGC 6240

In Arp 220, major molecular gas disks are found centered on each nucleus while in NGC 6240, the major gas concentration lies between the two nuclei, suggesting a somewhat earlier stage in the merging for NGC 6240 as compared to Arp 220 (Sakamoto et al., 1999; Tacconi et al., 1999; Scoville et al., 2000; Engel et al., 2010). Since NGC 6240 and Arp 220 represent late and final coalescence

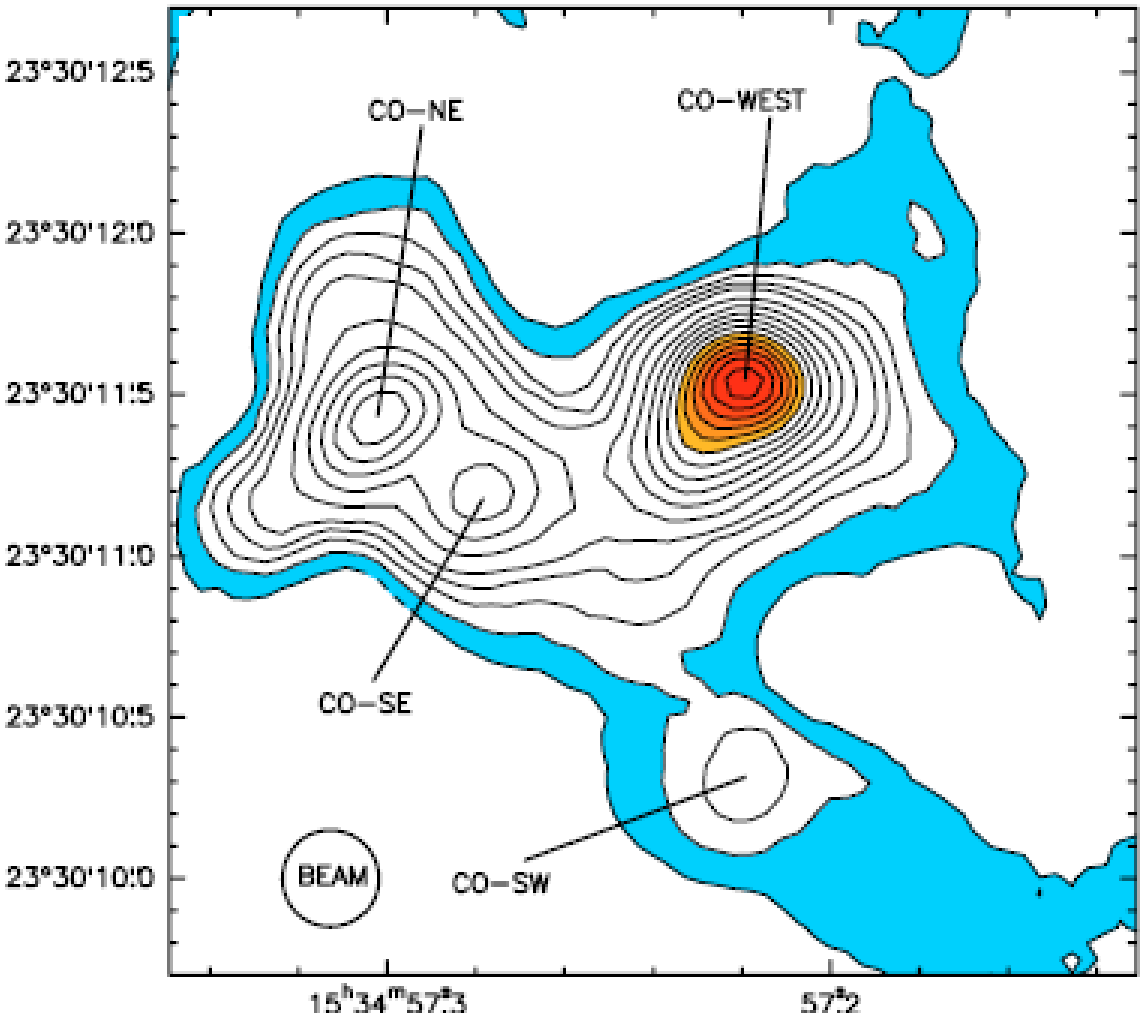


Figure 1.1: The central 3" of Arp 220 observed at IRAM interferometer in CO(2-1) integrated over 770 km $s^{-1}$, with the 1.3mm continuum subtracted. The two nuclei are labeled as CO-NE and CO-West. The beam (lower left) is 0.30″with $T_b/S$ = 266 K $beam^{-1}$. Contours are 2 to 10 separated by 2, then 14 to 54 separted by 4 (in Jy km $s^{-1}$). The CO-West peak is 56.5 Jy km $s^{-1}$; CO-NE is 33.4 Jy km $s^{-1}$ $beam^{-1}$ (Downes & Eckart, 2007).

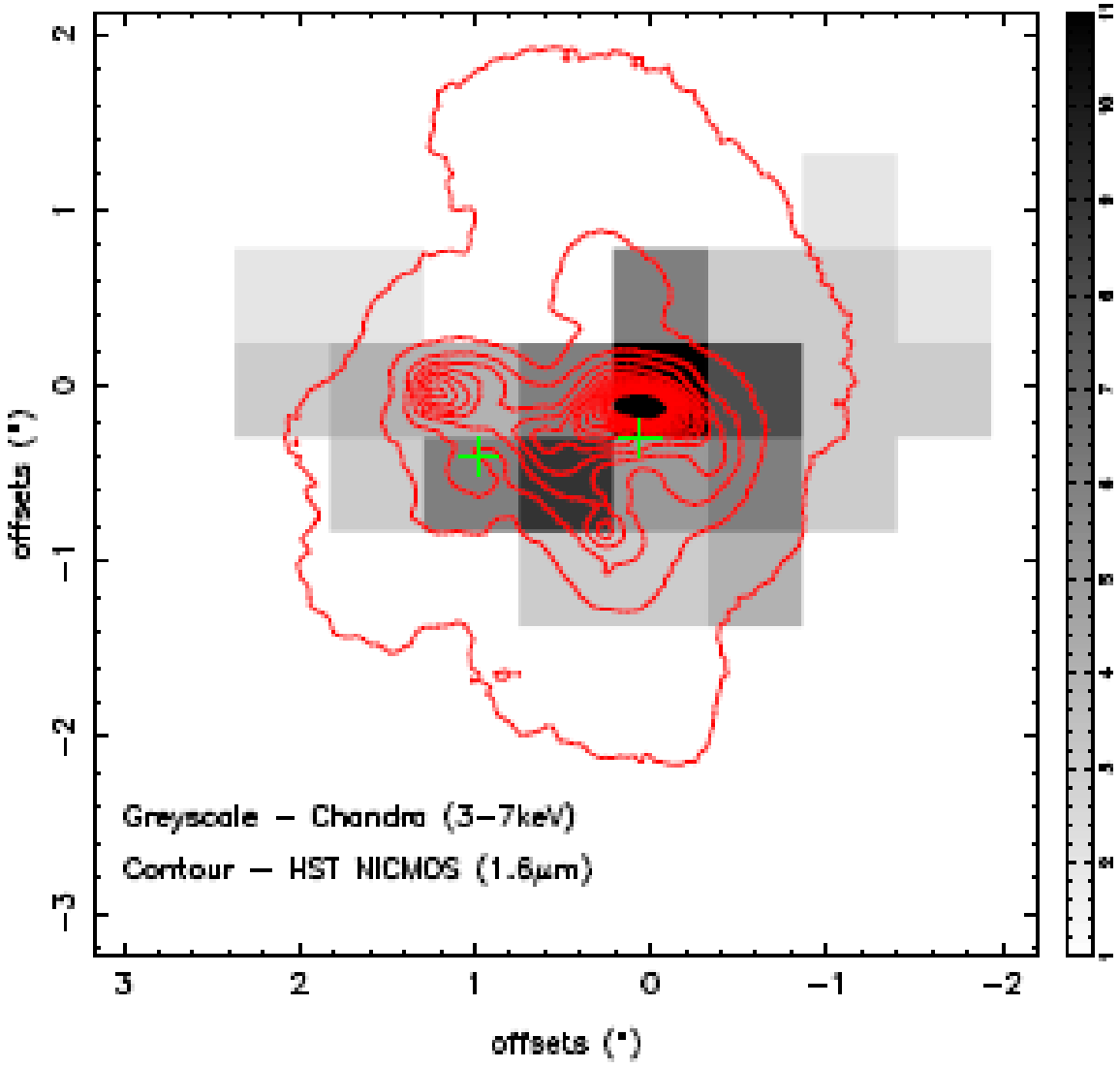


Figure 1.2: Arp 220 AGN: The Chandra 37 keV image of the double nucleus region of Arp220 overlaid with the HST NICMOS 1.6 $\mu$m contour map (Scoville et al., 2000). The positions of the double radio nuclei are indicated with plus symbols in green (Iwasawa et al., 2005).

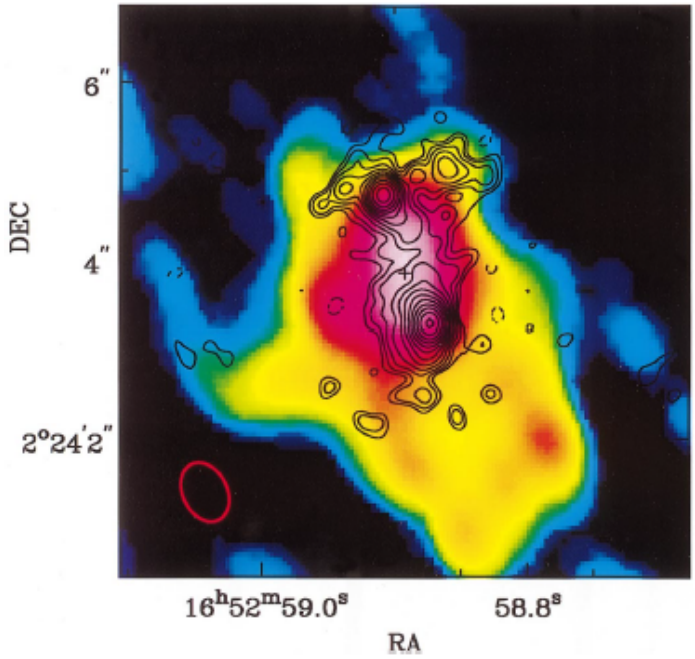


Figure 1.3: Overlay of a logarithmically spaced contour map of the 8 GHz radio continuum emission (resolution 0.15" FWHM; Colbert et al. (1994)) on a false-color map of the CO 2→1 integrated flux in NGC 6240 (Tacconi et al., 1999). Radio contours run from $10^{-1}$ to $10^{1.2}$ mJy in steps of $10^{0.2}$. The contours show the two nuclei in this system, both of which have been detected in hard X-ray emission (Komossa et al., 2003).

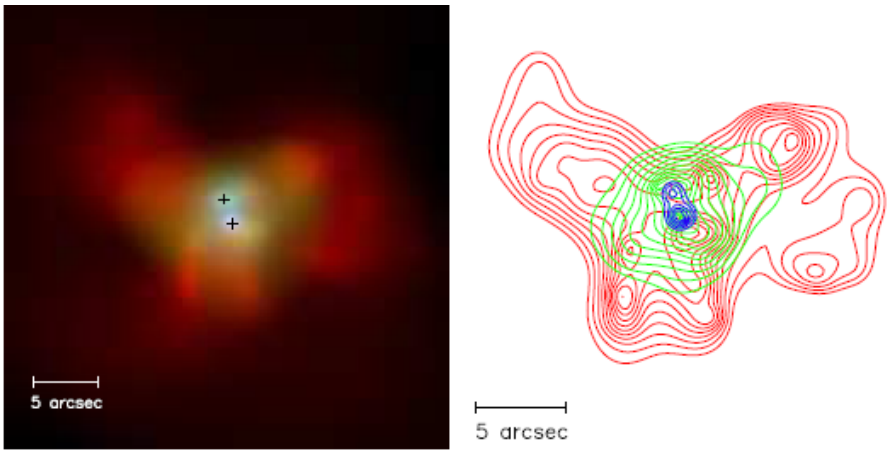


Figure 1.4: NGC 6240 AGN: Multi-colour image of NGC6240 using Chandra. Red=soft (0.5-1.5 keV), green = medium (1.5-5 keV), and blue = hard (5-8 keV) X-ray bands. The right image shows contour plots, using the same colour coding (Komossa et al., 2003).

stages, respectively, of galaxy merging, they provide an excellent opportunity to study the final merger process (See Fig. 1.5). Observations of these systems can also probe the fueling of the supermassive black holes via galactic merging, quantify gas properties, star formation activity, and dynamics on scales within ∼100pc to constrain anticipated theoretical modeling.

In Chapter 2, we discuss the details of the observations and process followed for the data reduction. The 2″ resolution observations from CARMA are discussed in Chapter 3. Chapter 4 does the same for the 0.5 - 0.8″ resolution observations from CARMA. In chapter 5, the submitted paper based on our observations, analysis and results is presented. Chapter 6 provides an overview of the Ph.D. research.

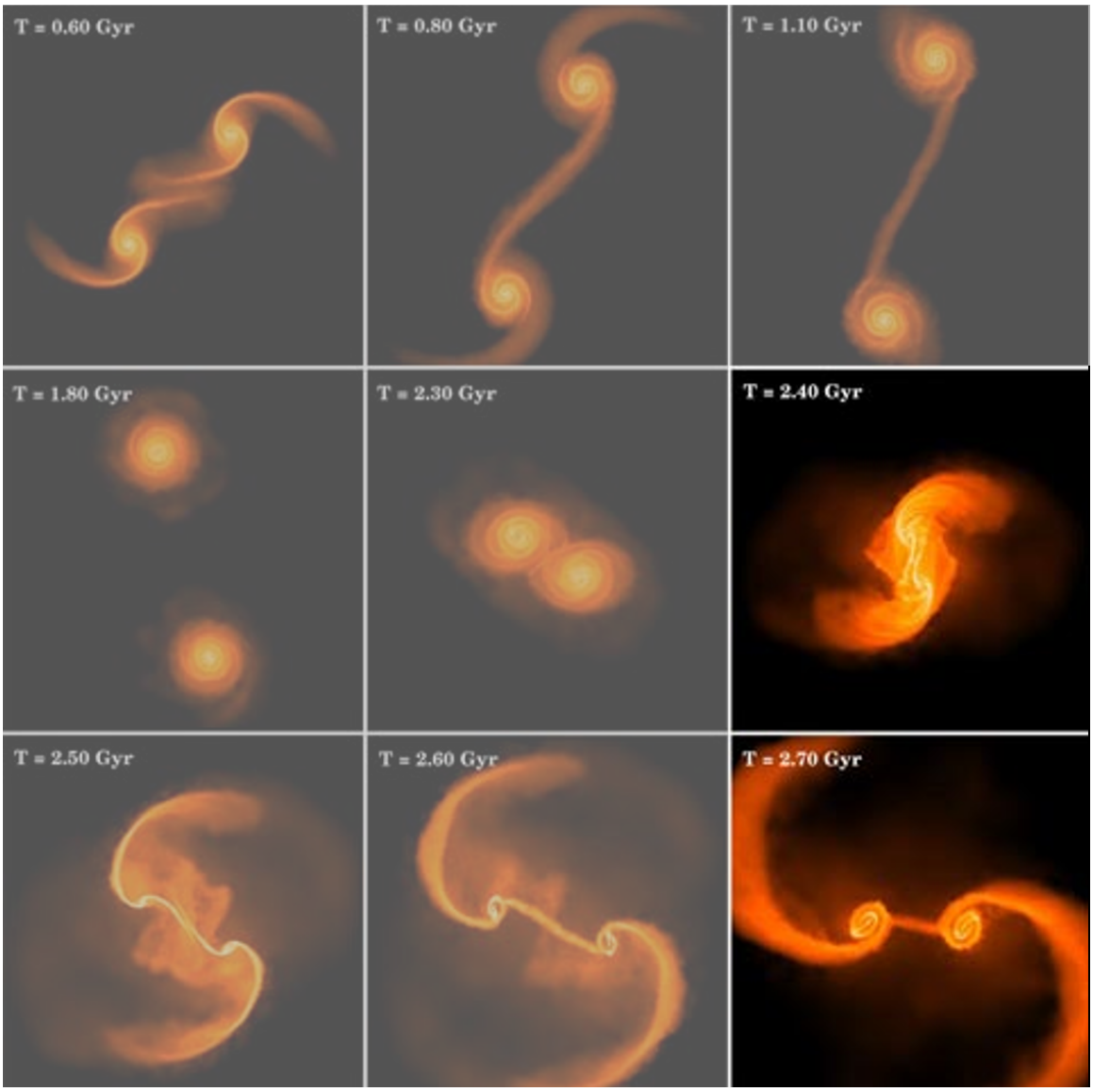


Figure 1.5: This image illustrates the complexity of a typical collision between two equal-mass disk galaxies. Only the gas component is visualized. Brighter colors indicate regions of higher gas density. The first 7 panel images measure 100 kpc on a side. The next two panels represent successive zooms on the central region. Image Credit: Stelios Kazantzidis, Ohio State University.

# Chapter 2

# Data: Observations and Reduction

The Combined Array for Research in Millimeter-wave Astronomy (CARMA) consisting of six 10.4-meter and nine 6.1-meter antennas (CARMA C array configuration, Fig. 2.1) that are used to observe CO(1-0), HCN(1-0), CS(2-1), HNC(1-0) and $HCO^+$(1-0) lines along with isotopomer lines $^{13}$CO(1-0), H$^{13}$CN(1-0) and $^{13}$CS(2-1) in Arp 220 and NGC 6240 (Table 3.1). These observations were done in good ($\tau_{112GHz} < 0.3$) to fair ($0.5 < \tau_{112GHz} < 0.3$) weather conditions receiving grades higher than C during several runs between December 2012 and November 2013. The B configuration observations were done between January 2013 and January 2014 under two proposals and several runs. The observations done in the C configuration of the antennas had antenna spacings between 26 - 370 m and a resolution of $\sim 2''$. In the B configuration, the antennas were spaced more widely at 100 - 1000 m and therefore, achieved a higher resolution of $\sim 0.8''$(Table 4.2).

## 2.1 Observations and Correlator Configuration

There are eight bands available, with a maximum of 4 GHz per sideband for the digital spectral line correlator used normally for the 10.4-meter and 6.1-meter telescopes. Sixteen bands or windows are available in cross-correlation mode as each band appears symmetrically in the upper and lower sidebands of the first local oscillator. Manipulating the frequencies of the second local oscillators, the bands were positioned independently within the IF bandpass to observe HCN(1-0), CS(2-1), HNC(1-0) and $HCO^+$(1-0) lines along with isotopomer lines H$^{13}$CN(1-0) and $^{13}$CS(2-1) in Arp 220 and NGC 6240 simultaneously.

The correlator configurations used for these observations for both the galaxies are shown in Fig. 2.2-2.5. It is possible to observe several widely-separated spectral lines simultaneously or with different velocity resolutions. The correlator was configured to have eight 500 MHz bands in the lower and upper sidebands each in the 2 bit quantization mode providing 95 channels of spectral resolution per band. Each channel corresponds to 5.208 MHz width or $\sim$15 km s$^{-1}$ in velocity space. Each band corresponds to $\sim$1500 km s$^{-1}$ in velocity space.

Figure 2.1: Antennas arranged in the C configuration at the CARMA site

For the lower frequency lines, the correlator was configured to observe HCN(1-0), HNC(1-0), $HCO^+$(1-0) and $H^{13}CN$(1-0) lines in the lower sidebands and CS(2-1) & $^{13}$CS(2-1) in upper sidebands. See Fig. 2.2 and 2.3.

For observing CO(1-0) and $^{13}$CO(1-0), the bands used were in the upper side band. In this configuration only two lines were being observed and the additional bands were located on either side, in case the lines were broader than the band. All lines were centered in the band at the $V_{LSR}$ of the respective galaxies except for the $HCO^+$(1-0) line.

For the C configuration, the phase calibrator used for these observation of ARP 220 is 1540+147. It is separated by 8.8deg from the source and has a flux of 0.6 Jy as measured by CARMA. It is the strongest nearby calibrator available for these observations. The phase calibrator used for NGC 6240 is 1658+076 which is at a 5.4deg separation and has a flux density of 0.6 Jy. For each observation cycle, 15 minutes of integration time was spent on the target and 2 minutes were spent on the phase calibrator.

For flux calibration, Mars, Neptune, 3C 273 and MWC349 were used. Flux calibrators were observed for an integration time of 5 minutes at the end of the observing period or track.

The total observation time including overheads for Arp 220 for observations of HCN(1-0), CS(2-1), HNC(1-0), $HCO^+$(1-0), $H^{13}CN$(1-0) and $^{13}$CS(2-1) lines was 48.5 hours. In the case of NGC 6240, the observation time was 36.7 hours. Observing times were 16.5 hours and 16.4 hours respectively for Arp 220 and NGC 6240 for CO(1-0) and $^{13}$CO(1-0).

For the B configuration, the same phase calibrators were used. For flux calibration Mars and MWC349 were used. For each observation cycle, 15 minutes of integration time was spent on the target and 2 minutes were spent on the phase calibrator. Flux calibrators were observed for an integration time of 5 minutes at the end of the track. The total observation time including overheads for Arp 220 for observations of HCN(1-0), CS(2-1), HNC(1-0), $HCO^+$(1-0), $H^{13}CN$(1-0) and $^{13}$CS(2-1) lines was 49 hours. In the case of NGC 6240, this observation time was 43.9 hours.

For CO(1-0) and $^{13}$CO(1-0), the total observing time was 34.4 hours . Because of bad weather, these lines could not be observed for NGC 6240 in the B configuration.

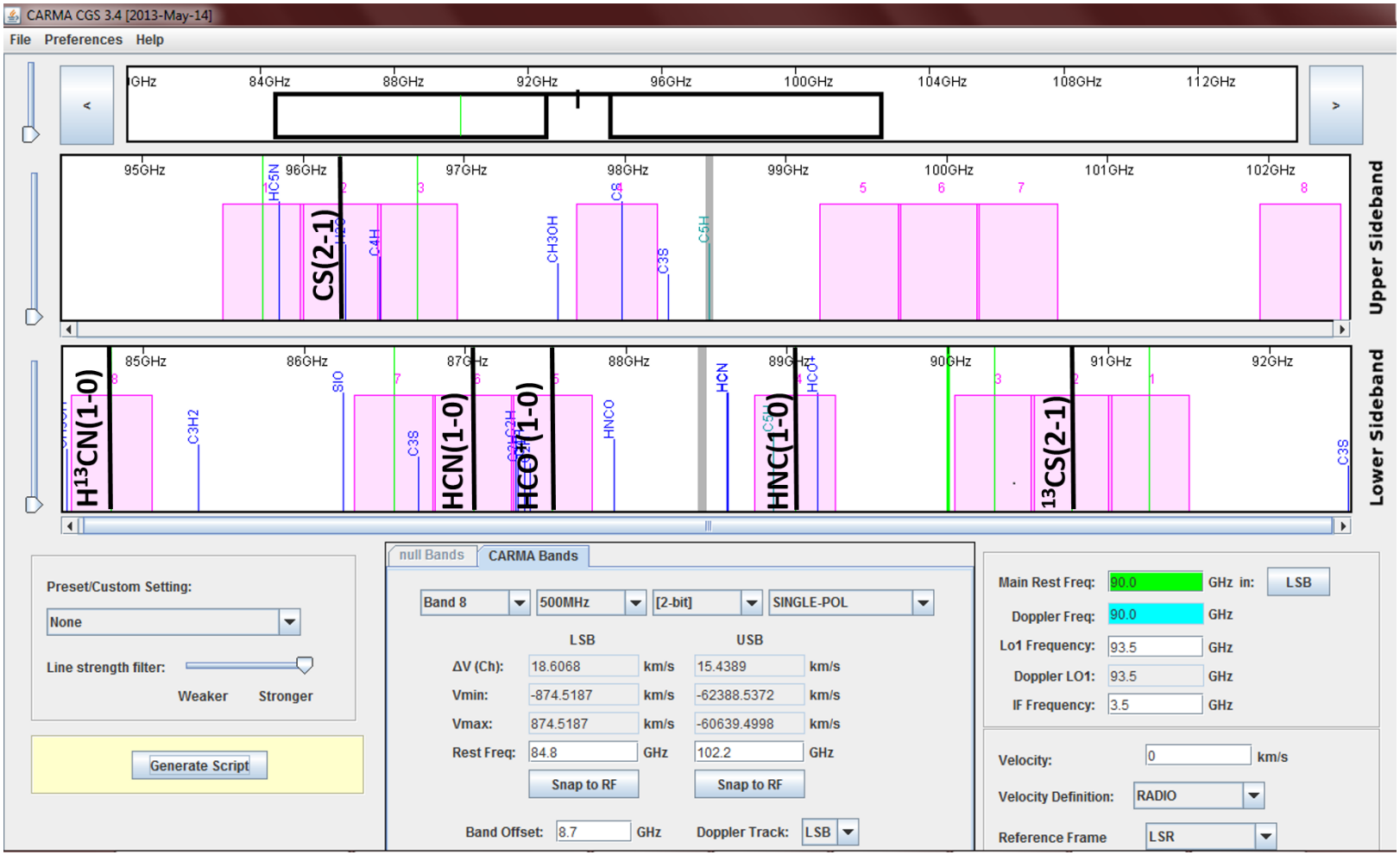


Figure 2.2: Correlator Configuration setup used for ARP 220 observations for both C and B array configurations at CARMA. In this setup, we observed HCN(1-0), CS(2-1), HNC(1-0) and $HCO^+$(1-0) lines along with isotopomer lines $H^{13}CN$(1-0) and $^{13}CS$(2-1)

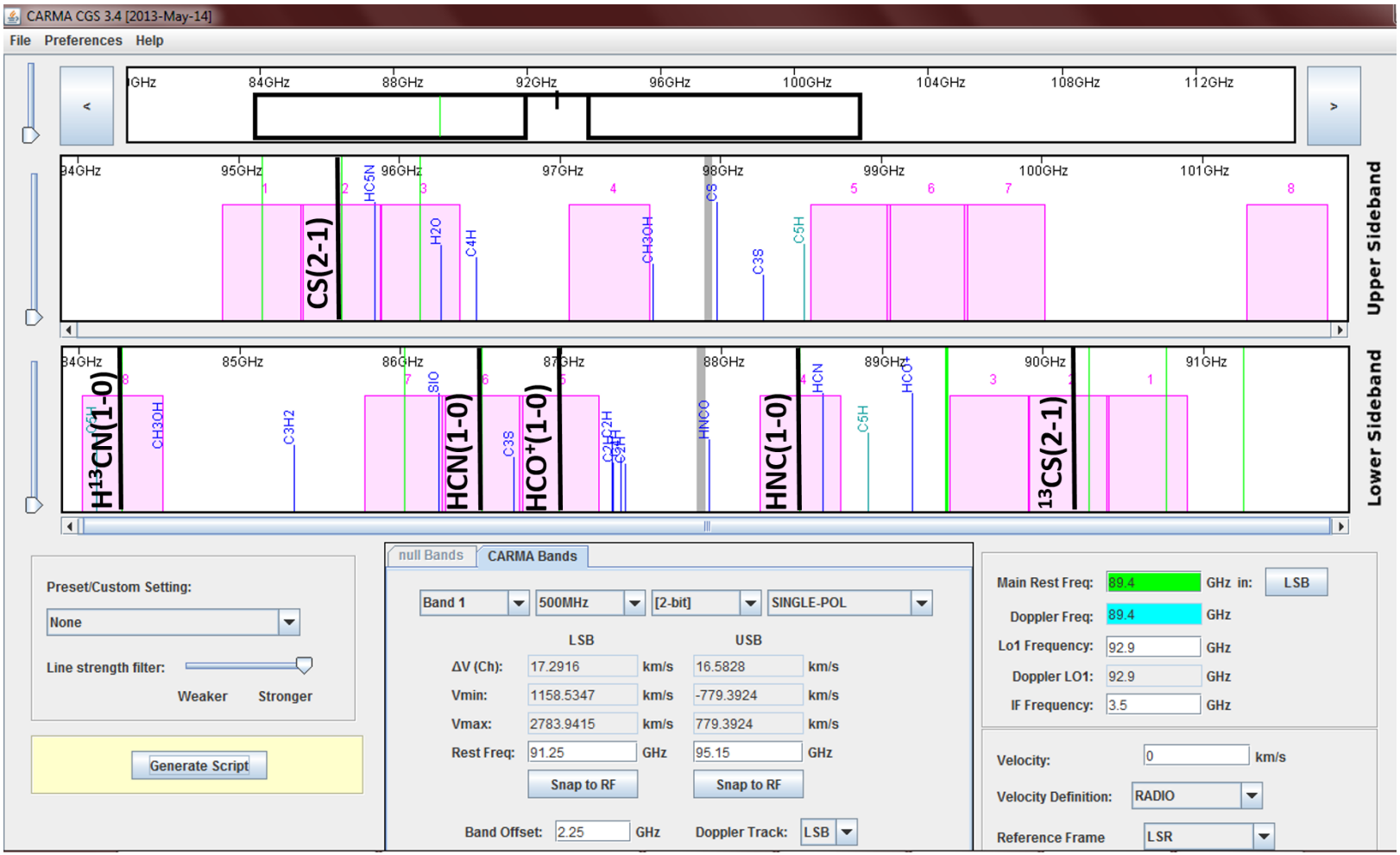


Figure 2.3: Correlator Configuration setup used for NGC 6240 observations for both C and B array configurations at CARMA. In this setup, we observed HCN(1-0), CS(2-1), HNC(1-0) and $HCO^+$(1-0) lines along with isotopomer lines $H^{13}CN$(1-0) and $^{13}CS$(2-1)

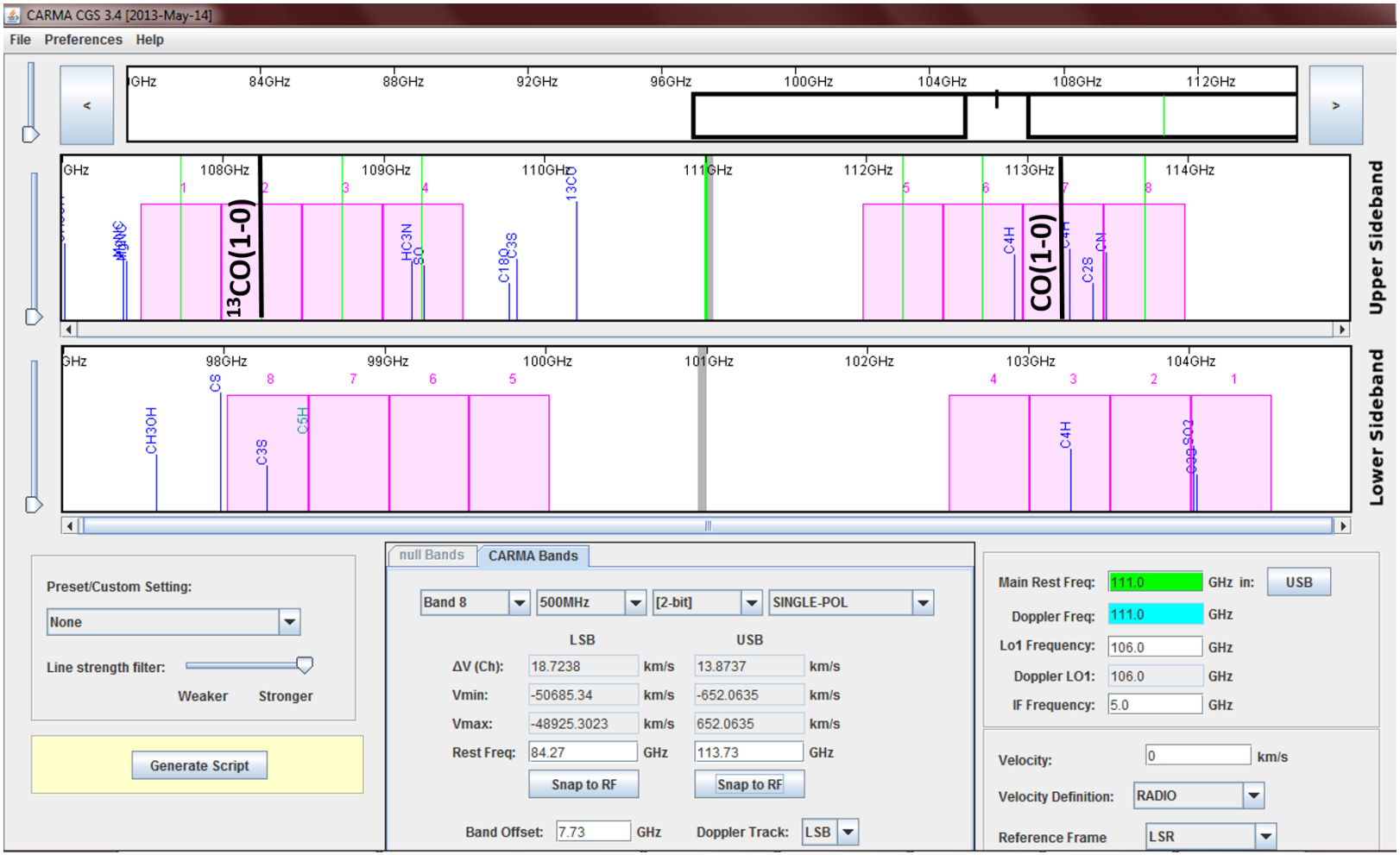


Figure 2.4: Correlator Configuration setup used for ARP 220 observations for both C and B array configurations at CARMA. In this setup, we observed $^{12}$CO(1-0) and $^{13}$CO(1-0)

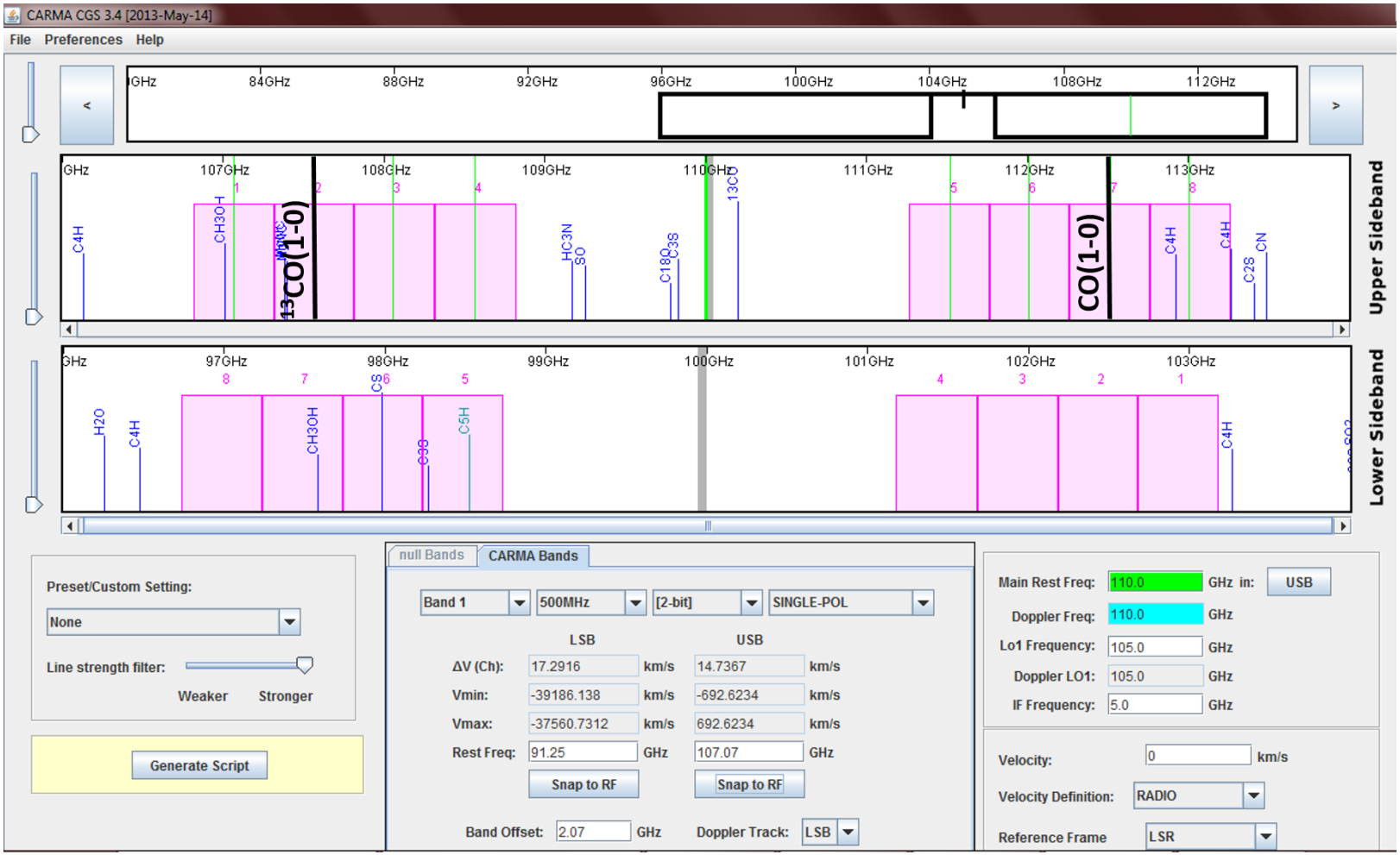


Figure 2.5: Correlator Configuration setup used for NGC 6240 observations for both C and B array configurations at CARMA. In this setup, we observed $^{12}$CO(1-0) and $^{13}$CO(1-0)

## 2.2 Data Reduction

In summary, our observations were done using 500 MHz correlator bands. We had 8 bands of 500 MHz in the Lower Side Band (LSB) and the Upper Side Band (USB). We chose wide-bands because they have the advantage of higher signal to noise ratio in each channel and because we were observing lines that were expected to be broad lines. The following sections detail the steps taken in the reduction of both B and C configuration for CARMA. The process followed for observations from both configurations is similar.

Data reduction for these data was done using the MIRIAD (Multichannel Image Reconstruction, Image Analysis and Display) package. MIRIAD can be thought of as a collection of programs or tasks that use a common interface written for CARMA users. These tasks or programs can be called directly from the UNIX command line or using a shell. MIRIAD can be used for the inspection, editing, calibration adn imaging of the u-v data. Hence, all the data reduction and image production has been performed using MIRIAD. The images produced using MIRIAD can be easily viewed using the usual viewers like ds9. Analysis of the calibrated data cube, such as line profiles and measurements of intensities was done using MATLAB.

The following sections will detail the data reduction and analysis done using the MIRIAD package.

### 2.2.1 Steps for Data Reduction

The scripts used for the data reduction were altered for this specific project from the general scripts available on the CARMA website. We began by identifying the basic information required for the reduction such the flux calibrator, passband calibrator, gain calibrator and of course, the source (ARP 220 or NGC 6240). From hereon, each band (8 in the USB and 8 in the LSB) maybe referred to as windows. Some basic flagging of data was set at the beginning of the data reduction.

For some observations, spectral windows were determined to have problems, either known at the time of the observations or noticed during data reduction. In such cases, these windows were flagged and these data segments therefore dropped from further processing. For all windows in all observations, edge channels were flagged. Time intervals for observations of source, flux, gain and passband calibrator, which had been chosen when the observation scripts were written, were also input into the script. Other inputs such as the antenna position file used for baseline solutions, any antennas to be flagged for bad observations, reference antennas for selfcal solutions etc are also determined.

The script first produces a dirty image from the observations not deconvolved for the synthesized interferometric beam point spread function. The dirty image is then later further cleaned. To produce the dirty image, parameters such as robust, which refers to the Brigg's visibility weighting

robustness parameter, need to be input. This parameter determines the weighting of visibilities in relatively sparsely filled regions of the u-v plane. The useful range tends to be between [-2,2], where values less than -2 corresponding to very little down-weighting of these sparsely filled regions, and values greater than +2 corresponding to natural weighting. Other parameters include image cell size and size of the output image size.

1. The first step is to apply the Baseline Solution. The baseline solutions for CARMA were generated at intervals of about every 2-3 weeks during each configuration and one at the outset of the configuration. These were provided online. The baseline solution employed for each of our datasets was in accordance with observer suggestion or chosen to be closest in time to when the observations were made. This made sure that antenna positions had the most appropriate values.

2. Data was flagged in accordance with the input at the beginning of the script, this included flagged windows, bad antennas, edge channels and baselines that were shadowed (with one antenna looking at the back of another antenna). This step can be repeated when additional flagging is warranted. The flagging can be in the form of specific channels, windows, time intervals (in case of weather disturbances) and antennas (such as in situations where antennas are being moved or switched off for various reasons).

3. Line correction may be applied. For our observations, this was not done. This is usually done to correct any variations that may occur in the path length along fiber optic cables. Since these don't change once the interferometer has been established into a configuration, there was no need to do this step.

4. At this point, we inspected the raw system temperature, amplitude, phase and spectra plots to determine if any additional flagging was needed.

5. The next step is the passband calibration of the data. This step corrects channel by channel any variations in amplitude and frequency. Channel by channel passband is only done for wideband windows. We see phase offsets between windows in raw data generally. Passband calibration removes these offsets. First, a non-astronomical passband was done using an internal noise source, observations of which were included in the observing script. An Astronomical source is then used to perform the final passband calibration.

6. The calibration corrections such as antenna gains, delay terms and passband responses are determined from multi-frequency observations. An average of the selected data subsets is used to determine delays and passband. Then using the time interval already set earlier in the script the gains are calculated out periodically. The basic aim is to have the same mean amplitude and phase for the point source phase calibrator as a function of time and frequency.

7. Now we need to correct any amplitude and phase fluctuation with time and this is done under Gain calibration. The flux of the gain calibrator has already been measured during flux calibration. The gain calibrator is then used to derive a gain solution which is then applied to the observations of the source. To achieve the best signal to noise ratio for the gain calibration, the wideband spectral windows are averaged.

8. Flux calibration is the next step in this process since the determination of the flux of the source being observed is an important goal of many observations. Choosing a strong flux calibrator is essential. Generally, a well known and studied one like Uranus or MWC 349 is chosen. Using the known flux, the flux measured from the flux calibrator is scaled to match. This scale factor is then used to calibrate the flux of all the sources observed in the track.

9. The last step is to make dirty images for a preliminary view of the data. At this point, the visibilities are used to form images. The images can be made to weight each visibility in inverse proportion to the noise variance. This optimizes the signal to noise ratio.

### 2.2.2 Image Production and Line Profiles

1. Once all the separate observations were reduced according to the steps described above, all data sets were concatenated. At this point, one could choose which object to select for imaging.

2. We start by making a dirty map again, choosing specific channels, averaging over them within windows, or selecting velocity ranges over which to image the source. Size of the output image, image cell size and robust are also optimized at this stage. A dirty beam and output map are both produced at this stage. This is used to clean the map.

3. Now we clean the dirty image produced in the earlier step. We used a command called 'mossdi' in MIRIAD which performs a Steer CLEAN on a mosaiced image or cube. The number of cleaning passes made depend on the number of iterations specified or when the absolute maximum residual falls below the specified flux limit.

4. At this step, we calculate residuals and convolve the source model with a Gaussian beam. We input the FWHM (full width at half max) of the gaussian beam to be used in the restoration. In all cases, this was the FWHM of the dirty beam.

5. Now, we have the cleaned image and desired measurements can be made. We can plot spectra along the velocity or frequency axis of the image. Further analysis after this step was performed on MATLAB routines I wrote.

# Chapter 3

# CARMA C Configuration: 2″ Observations and Analysis

In this section, we describe the multiple transition lines observed in Arp 220 and NGC 6240 at a higher resolution than what was achieved in previous studies (except for CO). This is the first comprehensive high resolution interferometric measurements of lower transition lines of the high dipole moment molecules for these galaxies. To compare the lines in both galaxies with each other and with earlier studies, we calculated velocity integrated fluxes and luminosities using Solomon et al. (1992b):

$$L' = 3.25 \times 10^7 (\frac{\nu_{obs}}{GHz})^{-2} (\frac{D_L}{Mpc})^2 (1+z)^3 (\frac{\int S_\nu \, dv}{Jy \, km \, s^{-1}}) \tag{3.1}$$

These numbers along with measurements from earlier studies are tabulated in Table 3.2.

## 3.1 Arp 220

### 3.1.1 CO(1-0)

The CO(1-0) emission is critical to determining the large scale molecular gas distribution and kinematics in the galaxies. The high resolution interferometric observations of CO(1-0) in Arp 220 shows a double peaked profile expected from the counter-rotating molecular gas disks observed in earlier studies (Scoville et al., 1997; Downes & Solomon, 1998) (Fig.5.2). The double horned feature seen in this study and in previous observations (Scoville et al., 1997; Downes & Solomon, 1998; Greve et al., 2009) is a result that clearly indicates the presence of double nuclei that is surrounded by a ring/disk of gas. We see a strong peak in CO(1-0) emission line at $\simeq$ -180 km s$^{-1}$ relative to the systematic $V_{LSR}$ of ARP 220 of 5434 km s$^{-1}$. The second peak, which is not as high in emission, is seen at about $\simeq$ 80 km s$^{-1}$. These peaks correspond to the blueshifted nucleus and redshifted nucleus, to the west and east, respectively, in the molecular disk. This is similar to the single-dish multitransition measurements of Greve et al. (2009) using 15 m James Clerk Maxwell Telescope

(JCMT) and to the Arp 220 observations done with the Owens Valley millimeter array by Scoville et al. (1997).

The integrated line flux for our observations is 385 ± 40 Jy km $s^{-1}$ which agrees very well with these previous measurements. OVRO interferometric observations measured it as 410 and 384 Jy km $s^{-1}$ (Scoville et al., 1997). On the other hand single dish measurements by Solomon et al. (1997) yield a total flux of 496 Jy km $s^{-1}$. Our results agree with the previous interferometric measurements more closely than the single dish measurements. For more comparisons, see Table 3.2. However, the close agreement of our interferometric data with other interferometric data and single dish measurements indicates that analysis is recovering almost all of the emission line flux for CO(1-0) in Arp 220. The FWHM of CO from our observations is 500 km $s^{-1}$, which again in good agreement with OVRO and IRAM measurements (Solomon et al., 1997). See Table 3.2 for more details.

### 3.1.2 $^{13}$CO(1-0)

$^{13}$CO(1-0) was also measured in our observations of Arp 220 (Fig.5.1(e)). It is not as strong as significant signal-to-noise ratio as CO(1-0), but it is at higher the $7\sigma$ level. The integrated flux measurement of $^{13}$CO(1-0) is 14 ± 2 Jy km $s^{-1}$. The single dish measurement for this transition (Greve et al., 2009) is 9 ± 2 Jy km $s^{-1}$. The measurements are discrepant at the $2\sigma$ level. Our $^{13}$CO line profile is similar to the single dish profile of Greve et al. (2009). It is not a double peaked profile like CO, rather a flattened profile offset from the $V_{LSR}$ of the galaxy. This indicates that the $^{13}$CO(1-0) flux is originating largely from the blueshifted western nucleus of Arp 220. The difference in profile of CO(1-0) and $^{13}$CO(1-0) indicates a difference in either the dynamics of the molecular gas from which it is originating or the optical depth of the molecular gas in the two nuclei. In this case, the profile shape difference is probably due to the $^{13}$CO(1-0) optical depth being higher in the western nuclei. The FWHM of our $^{13}$CO(1-0) observations is 380 km $s^{-1}$. This agrees with the single dish measurements done by Greve et al. (2009).

### 3.1.3 HCN(1-0)

HCN(1-0) (Fig. 5.1(a)) shows a double peaked profile similar to CO(1-0). The peaks are stronger and more clearly distinguishable in HCN(1-0) transition than in CO(1-0). The peaks are also of similar strength, unlike those seen in CO(1-0). It is a broad line, its width comparable to CO. The similarity in the strength of both the peaks indicates that the physical conditions in the densest molecular gas in the two nuclei are similar. The relevant physical conditions include density, temperature, and opacity. The redshifted peak from the eastern nuclei has peak flux a little higher than the blueshifted peak. The difference in their maximum fluxes is larger than the uncertainty from the measurements

and therefore the intensity of the blueshifted peak is of significance. The blueshifted peak at $\simeq$ -120 km s$^{-1}$ has a peak flux of 0.115 Jy, whereas the redshifted peak at $\simeq$ 190 km s$^{-1}$ has a peak flux of 0.125 Jy.

The profile of the HCN(1-0) transition in our observations is very similar to previous observations, both from single dish and interferometric measurements. The main difference is in the difference in the intensities of the two peaks in the profile. While we see a small but significant difference in the intensities of the dual peaked profile, the single dish measurements from Greve et al. (2009) do not show any significant differences.

The integrated line flux for our HCN(1-0) emission is 42 $\pm$ 4 Jy km s$^{-1}$. Interferometric observations from Plateau de Bure interferometer (PdBI), measured the integrated flux at 35 $\pm$ 11 Jy km s$^{-1}$ (Radford et al., 1991) and single dish observations from the IRAM 30m telescope (Greve et al., 2009) measured an integrated flux of 59 $\pm$ 12 Jy km s$^{-1}$ . Thus, the measurements are within the uncertainties. We have confidence in our measurements and analysis because of the strong agreement with the CO(1-0) measurements with previous studies. The FWHM is measured at 565 km s$^{-1}$ in our observations compared to 550 km s$^{-1}$ from the IRAM 30m Greve et al. (2009).

### 3.1.4 CS(2-1)

CS(2-1) is weaker (Fig. 5.1(b)) than the HCN and CO emission in our Arp 220 observations. A double peaked profile is again seen here, indicating emission from each of the two nuclei. However, the peaks are not as distinguishable and equally broad as seen in the HCN(1-0) spectra. The peaks are not of equal strength and the difference in the intensities of the peak is greater than the uncertainties in the measurements. The blueshifted peak from the western nucleus at $\simeq$ -50 km s$^{-1}$ has a peak flux of 0.09 Jy, whereas the redshifted peak at $\simeq$ 200 km s$^{-1}$ has a peak flux of 0.075 Jy.

Our profile for the CS(2-1) emission is very similar to previous single dish measurements (Greve et al., 2009). The integrated line flux for our CS(2-1) transition is 11 $\pm$ 0.1 Jy km s$^{-1}$. This is very similar to single dish observations from the IRAM 30m measured the integrated flux at 12 $\pm$ 3 Jy km s$^{-1}$ (Greve et al., 2009). The FWHM is measured at 345 km s$^{-1}$ in our observations for this transition in agreement with FWHM of 339 km s$^{-1}$ the IRAM 30m telescope (Greve et al., 2009) measurements.

### 3.1.5 HNC(1-0)

The HNC(1-0) emission is surprisingly strong in our observations (Fig. 5.1(c)). It is stronger than the HCN(1-0) emission line in Arp 220. Again, a clearly defined double horned profile is seen and as in the case of HCN(1-0) transition the peaks are not of equal strength. Even more surprising, the

relative strength of the peaks is not similar to that seen in HCN(1-0). Here the blueshifted peak from the western nuclei is has a peak flux higher than the redshifted peak. Therefore, the emission lines CO(1-0), CS(2-1), HNC(1-0), and $HCO^+$(1-0) have similar profiles with the HCN(1-0) emission line profile being the outlier. The blueshifted peak from the western nucleus at $\simeq$ -80 km $s^{-1}$ has a peak flux of 0.14 Jy, whereas the redshifted peak at $\simeq$ 175 km $s^{-1}$ has a peak flux of 0.11 Jy.

The profile of the HNC(1-0) transition in our observations are very similar to previous single dish observations (Greve et al., 2009; Aalto et al., 2002). The integrated line flux for our HNC(1-0) transition is 53 $\pm$ 5 Jy km $s^{-1}$. This is very similar to single dish flux of 55 $\pm$ 11 Jy km $s^{-1}$ from the IRAM 30m telescope (Huettemeister et al., 1995). However, our measurements do not agree with more recent observations done using SEST (Aalto et al., 2002) and IRAM 30m (Greve et al., 2009). The FWHM is measured at 400 km $s^{-1}$ in our observations for this transition. The HNC(1-0) transition is less broad line than HCN(1-0) transition.

### 3.1.6 $HCO^+$(1-0)

The $HCO^+$(1-0) emission is also surprisingly strong (Fig. 5.1(d)) and the profile is double peaked with less emission at the middle velocities than was seen in the previous lines. Like CO(1-0), CS(2-1), HNC(1-0), the blueshifted peak has a peak flux higher than the redshifted peak. The blueshifted peak from the western nuclei at $\simeq$ -150 km $s^{-1}$ has a peak flux of 0.057 Jy, whereas the redshifted peak at $\simeq$ 150 km $s^{-1}$ has a peak flux of 0.045 Jy.

The integrated line flux for the $HCO^+$(1-0) emission is 37 $\pm$ 4 Jy km $s^{-1}$. This value disagrees with previous interferometric observations from Plateau de Bure interferometer (PdBI) which yielded 20 $\pm$ 6 Jy km $s^{-1}$ (Radford et al., 1991). Single dish observations from the IRAM 30m telescope (Solomon et al., 1992a) measured an integrated flux of 19 $\pm$ 6 Jy km $s^{-1}$. The FWHM is 570 km $s^{-1}$ in our observations for this transition. Previous $HCO^+$(1-0) observations do not have a measured FWHM listed. The $HCO^+$(1-0) emission line width indicates strong turbulence in the molecular gas.

The disagreement in our measurements of $HCO^+$(1-0) integrated line flux with previous single dish and interferometric observations is surprising. Because of this discrepancy many diagnostics such as line ratios used to understand the properties and environments of the molecular gas will show different results. However, we are confident in our observations and calibrations, since all of the emission lines except (CO(1-0) and $^{13}$CO(1-0)) were observed using the same correlator configuration and with similar synthesized beams. The agreement with measurements of the other line intensities to previous measurements indicates that our measurements are well calibrated.

### 3.1.7 Isotopomer Emission Lines

Along with the afore mentioned emission lines, we were also able to configure the correlator at CARMA to observe the isotopomer lines $H^{13}CN$(1-0) and $^{13}CS$(2-1). While we were able to detect $H^{13}CN$(1-0) (Fig. 5.1(f)) at more than $4\sigma$ level, $^{13}CS$(2-1) was not detected. The integrated line flux of $H^{13}CN$(1-0) is $15 \pm 2$ Jy km s$^{-1}$ and the FWHM is 400 km s$^{-1}$.

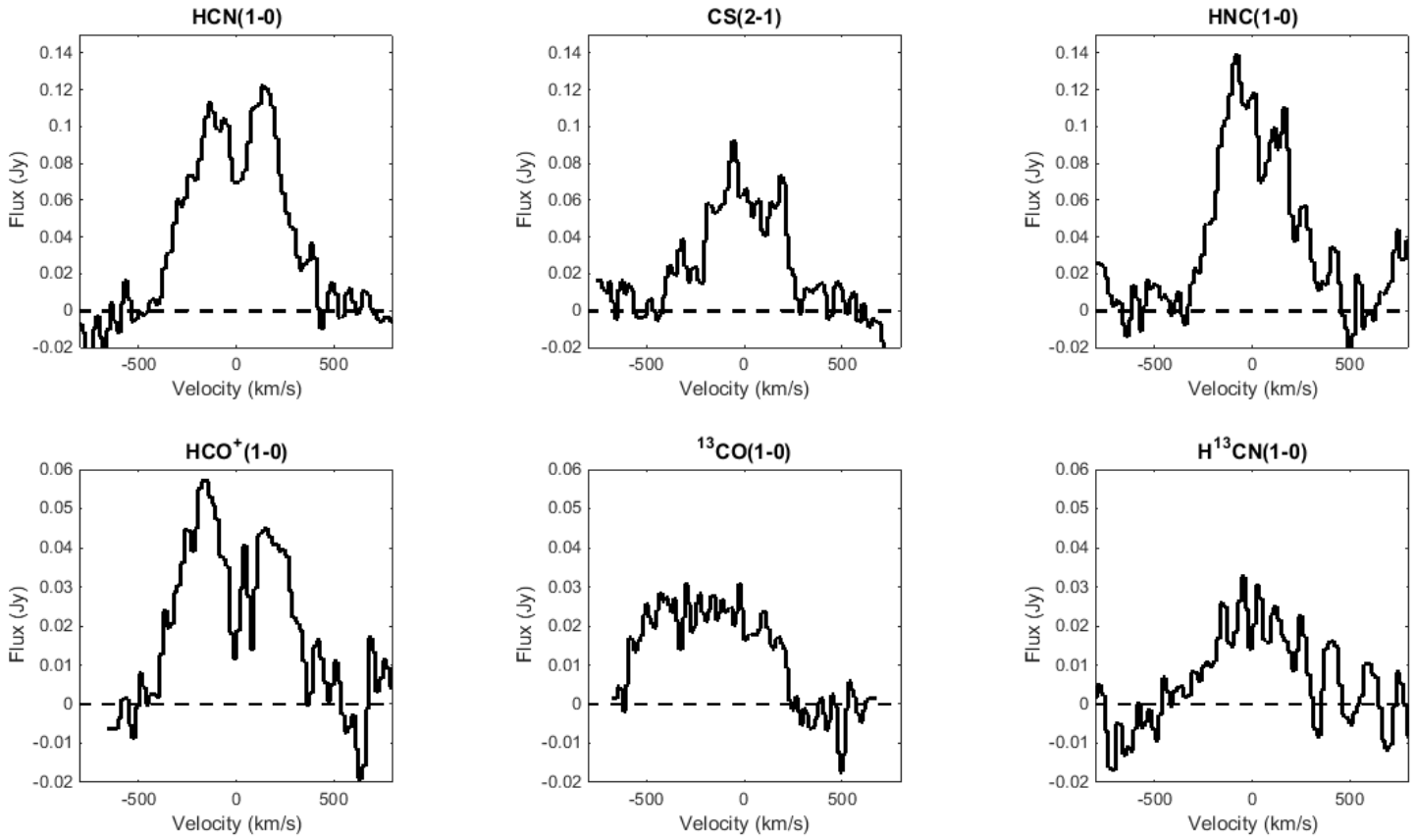


Figure 3.1: Molecular line spectra observed in Arp 220. The velocity scale for all transitions is same and centered at the galaxy redshift. HCN(1-0), CS(2-1) and HNC(1-0) transition spectra (panels (a)-(c)) are on the same flux scale. The $HCO^+$(1-0), $^{13}CO$(1-0), and $H^{13}CN$(1-0) spectra (panels (d)-(f)) scales are stretched to show the weaker spectra features.

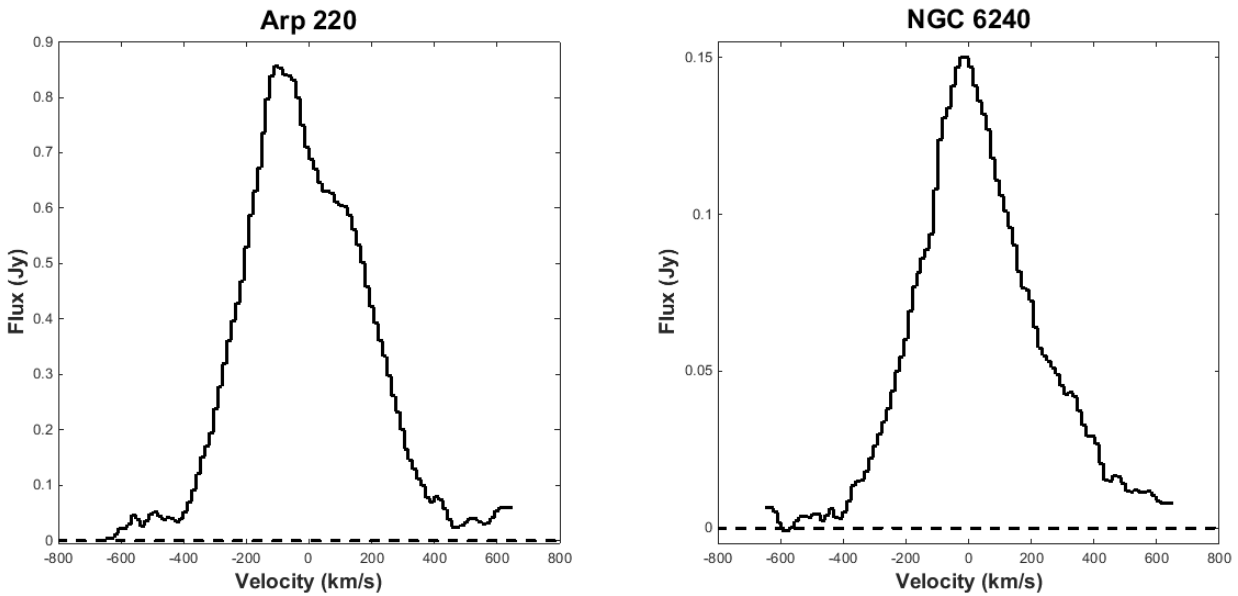


Figure 3.2: Molecular CO(1-0) spectra observed in Arp 220 and NGC 6240. The velocity scale for transitions is the same as the transitions in Fig. 5.1 for Arp 220 and Fig. 5.3 for NGC 6240, centered on the galaxy redshifts. The velocity limits are the same for both the galaxies. The flux scale is six times expanded for NGC 6240.

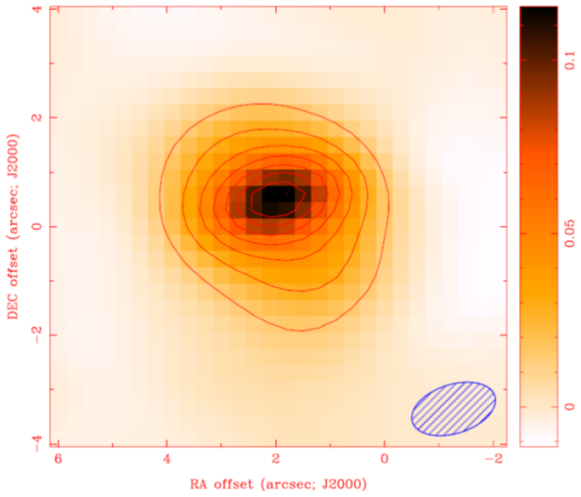


Figure 3.3: Arp 220 Integrated Line Intensity images for CO(1-0) emission. Contours are at $2\sigma$ spacings starting at $4\sigma$. The beam size is shown in the lower right corner

## 3.2 NGC 6240

All the lines detected in NGC 6240 show a Gaussian-like velocity profile. This is in contrast to Arp 220, which has a double peaked line profile. This suggests that turbulence or disordered random motions rather than rotation is dominating the line profiles in NGC 6240. This is consistent with the fact that the molecular and dust continuum emission shows a single concentration of ISM between the two stellar nuclei (Scoville et al., 2015), rather than the two concentrations centered on each of the stellar nuclei as in Arp 220. This seems to be the case on a wide range of spatial scales. In Arp 220 this does not seem to be the case, as the double peak features also evolve with the different transition lines which are charting dissimilar densities and temperatures (Greve et al., 2009).

### 3.2.1 CO(1-0)

Unlike Arp 220, CO(1-0) profile in NGC 6240, shown in Fig. 5.2, is a single peak. This concurs with the model of single molecular gas disk like concentration between the two nuclei. The single-peaked profile peaking on the blue side (relative to $V_{LSR}$ of 7359 km $s^{-1}$) is similar to previous interferometric observations from OVRO (Bryant & Scoville, 1999) and single dish observations at the IRAM 30m (Solomon et al., 1997). The profile is also very similar to that observed for higher transitions CO(2-1) and CO(3-2) (Tacconi et al., 1999; Greve et al., 2009), the only difference being that these emission lines have a more blueshifted peak than the CO(1-0) transition. The peak in our observations is at -25 km $s^{-1}$, whereas in the case of CO(2-1) the peak is skewed to almost -200 km $s^{-1}$. This is very likely due to the higher optical depth expected in the CO(2-1) line compared with CO(1-0).

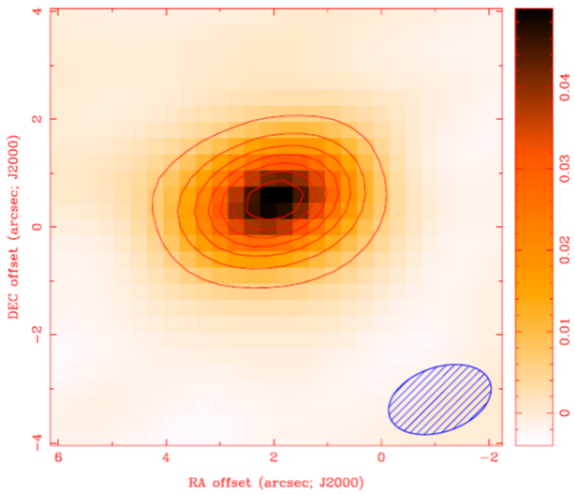


Figure 3.4: Arp 220 Integrated Line Intensity images for HCN(1-0) emission. Contours are at $2\sigma$ spacings starting at $4\sigma$. The beam size is shown in the lower right corner

The integrated line flux for our observations is 304 ± 30 Jy km $s^{-1}$. OVRO interferometric observations (Bryant & Scoville, 1999) measured it as 324 Jy km $s^{-1}$ and single dish observations at IRAM 30m measured an integrated flux of 314 Jy km $s^{-1}$ (Solomon et al., 1997). Thus, our results closely agree with previous interferometric measurements and single dish measurements. For more comparisons, see Table 3.2. The close agreement of our interferometric data with other interferometric data and single dish measurements indicates that our analysis is recovering almost all of the emission line flux in Arp 220. The FWHM for our integrated emission line profile is 400 km $s^{-1}$, which again is in good agreement with IRAM measurements (Solomon et al., 1997). See Table 3.2 for more details.

### 3.2.2 HCN(1-0)

HCN(1-0) spectra (Fig. 5.3(a)) has a single peaked profile, consistent with the CO(1-0) profile. However, the profile not as sharply peaked as CO(1-0). Its width is similar to CO(1-0) in NGC 6240. The profile seen in our observations is also similar to the ones seen in previous observations, both single dish observations (Greve et al., 2009) and interferometric observations (Tacconi et al., 1999; Nakanishi et al., 2005). The line peaks at 0 km $s^{-1}$ relative to the $V_{LSR}$ of NGC 6240 of 7359 km $s^{-1}$. This is not seen in other observations (Nakanishi et al., 2005; Greve et al., 2009), where the line peaks at -50 km $s^{-1}$ and -200 km $s^{-1}$, respectively. The velocities at peak fluxes of HCN(1-0) and CO(1-0) in our observations are internally consistent; the difference between measured velocity at peak flux relative to the galaxy and that in previous observations is simply the different systemic $V_{LSR}$ assumed.

The integrated line flux for our HCN(1-0) line is 26 ± 2.6 Jy km $s^{-1}$. Interferometric observa-

tions from Nobeyama Millimeter Array (NMA), measured an integrated flux of 14 ± 4 Jy km $s^{-1}$ (Nakanishi et al., 2005) and single dish observations from IRAM 30m ((Greve et al., 2009)) measured 13 ± 3 Jy km $s^{-1}$ . Our observations best agree with IRAM 30m observations done earlier (Solomon et al., 1992a) which obtained 26 ± 8 Jy km $s^{-1}$. We have confidence in our measurements and analysis because of the agreement of the CO(1-0) measurements with previous CO studies which have been more numerous. The FWHM is measured at 350 km $s^{-1}$ in our observations for this transition. This agrees well with the IRAM 30m telescope (Greve et al., 2009) measurements.

### 3.2.3 CS(2-1)

The CS(2-1) emission (Fig.5.3(b)) is much weaker in NGC 6240 than in Arp 200. While a single peak is apparent, not much can be said about the shape of the profile given the low signal-to-noise ratio. The detection, while weak, is still a 5 $\sigma$ detection. From what can be seen, the profile is single peaked as expected. The line has not been detected by other observations. Our interferometric capabilities along with long observation times have made this detection possible. The integrated flux measured for the CS(2-1) transition is 3 ± 0.6 Jy km $s^{-1}$. The FWHM is not a definitive measurement in this case. The quantity listed in Table 3.2 is an approximate estimate.

### 3.2.4 HNC(1-0)

HNC(1-0) (Fig.5.3(c)) is another weak line in NGC 6240. The only observations in literature that we could find were done at the 15m Swedish-ESO Submillimetre Telescope (SEST) (Aalto et al., 2002). While it is not a strong emission line, we were able to detect it at 4$\sigma$ level. We see more of a profile and stronger emission than the previous single dish measurement. The integrated flux density is 19 ± 4 Jy km $s^{-1}$. This is similar to the previous single dish observation. The integrated flux was measured at 14 ± 7 Jy km $s^{-1}$ by SEST. The FWHM is not a high accuracy measurement for this line.

### 3.2.5 $HCO^+$(1-0)

As in Arp 220, $HCO^+$(1-0) (Fig.5.3(d)) is a very strong emission line in NGC 6240. This was surprising considering that many of the other well studied emission lines were much weaker than this emission line. Its profile is very similar to the other strong emission lines (CO(1-0) and HCN(1-0)) in NGC 6240. However, the $HCO^+$ peak is not at 0 km $s^{-1}$, as is the case with the other two lines but at -50 km $s^{-1}$. While its peak is sharp, comparable to CO(1-0), the overall profile is more similar to the HCN(1-0) emission line. The blueshifted rise of the line is steeper than the redshifted rise. The redshifted line wing has a slower decline from the peak. As a result, a Gaussian profile would not fit either of the HCN(1-0) or $HCO^+$(1-0) lines. The peak of this emission line is at 0.021

Jy.

The integrated line flux for our $HCO^+$(1-0) transition is 40 ± 4 Jy km $s^{-1}$, which is similar to the flux measured for Arp 220. This is the only emission line where integrated flux density of the line is comparable for Arp 220 and NGC 6240.

This measurement disagrees with previous observations by a significant margin. In comparison Interferometric observations from NMA (Nakanishi et al., 2005), measured the integrated flux of 21 ± 3 Jy km $s^{-1}$ and single dish observations from IRAM 30m (Graciá-Carpio et al., 2006) measured an integrated flux of 25 ± 8 Jy km $s^{-1}$. The FWHM is measured at 470 km $s^{-1}$ in our observations for this transition. $HCO^+$(1-0) is also surprisingly a broad line, indicating a lot of turbulence in the molecular gas. Its FWHM is comparable to that of the CO(1-0) line, indicating perhaps similar gas dynamics.

The disagreement in our measurements of $HCO^+$(1-0) integrated line flux with previous single dish and interferometric observations is surprising. Because of this discrepancy many diagnostics such as line ratios used to understand the properties and environments of the molecular gas will show different results. However, we are confident in our observations and subsequent calibrations and analysis. A very strong factor which gives confidence to our observations is the fact that all of the emission lines except CO(1-0) and $^{13}$CO(1-0) were observed using the same correlator configuration and interferometer. The agreement in measurements of the other line intensities with previous measurements indicates that overall our calibrations and measurements are accurate.

### 3.2.6 Isotopomer Emission Line

The correlator was configured to also simultaneously observe the isotopomer lines for many of the emission lines we are observing here, such as $^{13}$CO(1-0), H$^{13}$CN(1-0), and $^{13}$CS(2-1). None of these lines were detected with high signal-to-noise ratio. $^{13}$CO(1-0) is a very marginal detection ($2\sigma$) seen in Fig.5.3(e) and we can only make an upper limit measurement for this line. This measurement will not be used for further analysis.

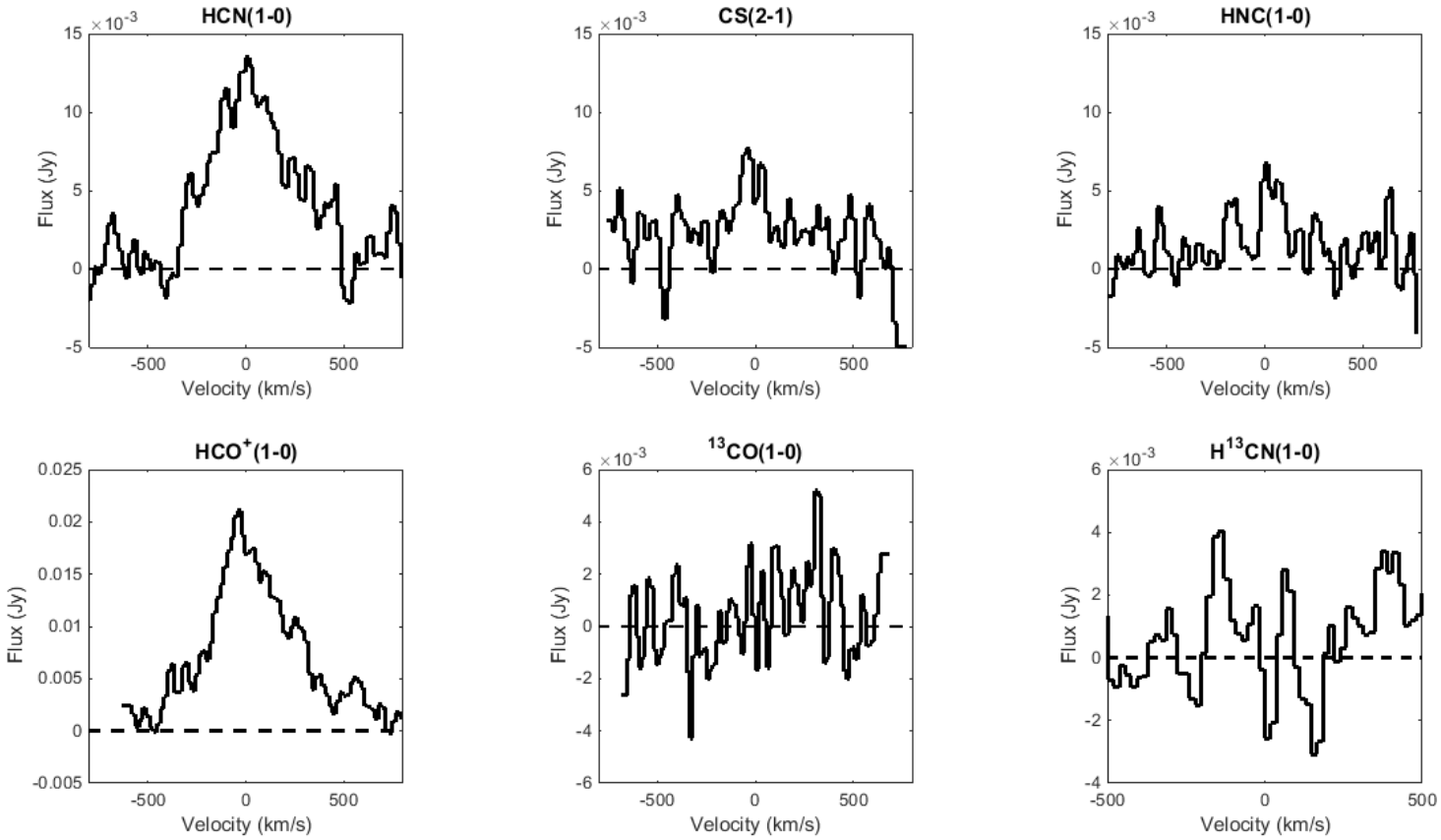


Figure 3.5: Molecular line spectra observed in NGC 6240. The velocity scale for all transitions is same and centered at the galaxy redshift. HCN(1-0), CS(2-1) and HNC(1-0) transition spectra (panels (a)-(c)) are on the same flux scale. The $HCO^+$(1-0) spectra has the highest peak of the transitions and its flux scale is higher. Note that the vertical scales in all panels except the panel (d) have a scale factor of $10^{-3}$. The $^{13}$CO(1-0) and H$^{13}$CN(1-0) spectra (panels (e)-(f)) scales have been stretched to show spectra features clearly.

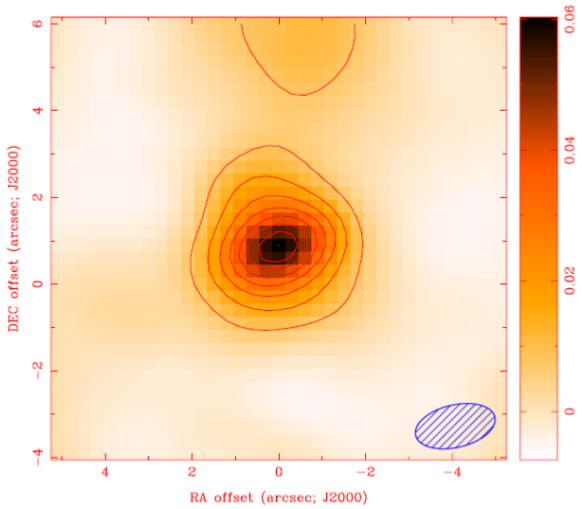


Figure 3.6: NGC 6240 Integrated Line Intensity images for CO(1-0) emission. Contours are at $2\sigma$ spacings starting at $4\sigma$. The beam size is shown in the lower right corner

Table 3.1: Observational Parameters for 2″ Observations

| Parameter | CO(1-0) | HCN(1-0) | CS(2-1) | HNC(1-0) | $HCO^+$(1-0) | $^{13}$CO(1-0) | $H^{13}CN$(1-0) | $^{13}$CS(2-1) |
|---|---|---|---|---|---|---|---|---|
| Arp 220 | | | | | | | | |
| $\nu_{obs}$ (GHz) | 113.219 | 87.05 | 96.23 | 89.05 | 87.60 | 108.239 | 84.80 | 90.84 |
| $t_{int}$(hrs) | 16.5 | 48.5 | 48.5 | 48.5 | 48.5 | 16.5 | 48.5 | 48.5 |
| HPBW(″) | 1.59 x 0.9 | 1.97 x 1.2 | 1.71 x 1.1 | 1.89 x 1.21 | 1.95 x 1.19 | 1.65 x 0.94 | 2.0 x 1.26 | 1.83 x 1.17 |
| NGC 6240 | | | | | | | | |
| $\nu_{obs}$ (GHz) | 112.517 | 86.51 | 95.64 | 88.49 | 87.06 | 107.568 | 84.27 | 90.28 |
| $t_{int}$(hrs) | 16.4 | 36.7 | 36.7 | 36.7 | 36.7 | 16.4 | 36.7 | 36.7 |
| HPBW(″) | 1.87 x 0.98 | 2.229 x 1.334 | 1.89 x 1.21 | 2.15 x 1.35 | 2.21 x 1.33 | 1.87 x 1.02 | 2.23 x 1.39 | 2.04 x 1.29 |

### 3.2.7 Comparing with Past Studies

We aim to compare with literature and previous studies to give comprehensive idea of the properties of the molecular gas in Arp 220 and NGC 6240. In this work, we have compiled measurements from previous observations of these systems, particularly for the lines that we have observed. Since a comprehensive interferometric study of these systems has not been done before, comparison with previous studies is essential. Table 3.2 is a compilation of many previous works, including both interferometric and single dish observations. While not completely comparable, both interferometric and single dish observations are useful for analysis.

Our observation of CO(1-0), for both Arp 220 and NGC 6240, agree with many previous measurements, for example Scoville et al. (1997); Downes & Solomon (1998); Bryant & Scoville (1999).

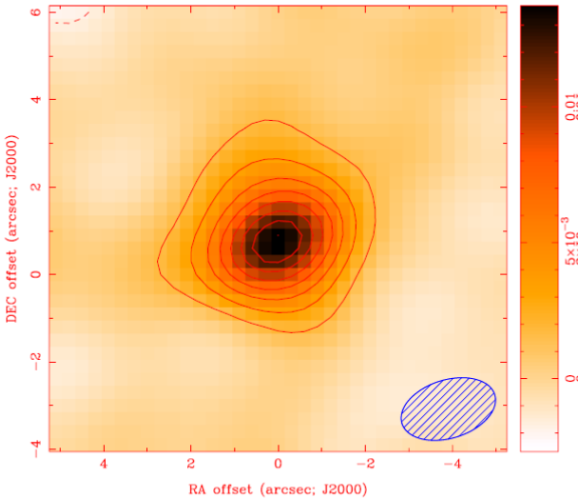


Figure 3.7: NGC 6240 Integrated Line Intensity images for HCN(1-0) emission. Contours are at $2\sigma$ spacings starting at $4\sigma$. The beam size is shown in the lower right corner

This gives us confidence in our data, methodology, and calibrations.

We see discrepancy in our measurements of flux densities of HCN(1-0), CS(2-1), HNC(1-0), and $HCO^+$(1-0) from previous studies, especially in comparison with single dish measurements. The strongest discrepancy is in the measurement of $HCO^+$(1-0) flux density, where our measurements are as much as twice that of other measurements (see Table 3.2). As we discuss later, this discrepancy may reflect significant differences between abundances in galactic sources and distant mergers.

Table 3.2: Molecular Transition Lines Detected: Arp 220 and NGC 6240

| Line | Arp 220 | | | | | NGC 6240 | | | | |
|---|---|---|---|---|---|---|---|---|---|---|
| | FWHM | $S_\nu \Delta v$ | $L'^c$ | Telescope | References | FWHM | $S_\nu \Delta v$ | $L'^c$ | Telescope | References |
| | km s$^{-1}$ | Jy km s$^{-1}$ | x10$^9$ K km s$^{-1}$ pc$^2$ | | | km s$^{-1}$ | Jy km s$^{-1}$ | x10$^9$ K km s$^{-1}$ pc$^2$ | | |
| CO(1-0) | 504 | 410 ± 41 | 5.9 ± 0.6 | OVRO | Scoville et al. (1997) | 370 | 314 ± 64 | 8.3 ± 1.7 | IRAM 30m | Solomon et al. (1997) |
| | ... | 384 ± 115 | 5.5 ± 1.7 | OVRO | Scoville et al. (1991) | 469 | 324 ± 33 | 8.6 ± 0.9 | OVRO | Bryant & Scoville (1999) |
| | 480 | 496 ± 99 | 7.2 ± 1.4 | IRAM 30 m | Solomon et al. (1997) | | 322 ± 29 | 8.5 ± 0.8 | | |
| | 500 | 385 ± 40 | 6.1 ± 0.64 | CARMA | This Work | 400 | 304 ± 30 | 8.9 ± 0.88 | CARMA | This Work |
| HCN(1-0) | ... | 35 ± 11 | 0.85 ± 0.27 | IRAM PdBI | Radford et al. (1991) | ... | 26 ± 8 | 1.17 ± 0.36 | IRAM 30 m | Solomon et al. (1992a) |
| | 550 | 59 ± 12 | 1.44 ± 0.29 | IRAM 30 m | Greve et al. (2009) | 340 | 13 ± 3 | 0.58 ± 0.13 | IRAM 30 m | Greve et al. (2009) |
| | 530 | 48 ± 14 | 1.17 ± 0.34 | IRAM 30 m | Krips et al. (2008) | ... | 14 ± 4 | 0.63 ± 0.18 | NMA | Nakanishi et al. (2005) |
| | 565 | 42 ± 4 | 1.1 ± 0.11 | CARMA | This Work | 350 | 26 ± 2.6 | 1.3 ± 0.13 | CARMA | This Work |
| CS(2-1) | 339 | 12 ± 3 | 0.24 ± 0.06 | IRAM 30 m | Greve et al. (2009) | ... | 7.5 ± 1.5 | 0.3 ± 0.06 | Herschel | Papadopoulos et al. (2014) |
| | 345 | 11 ± 0.1 | 0.24 ± 0.02 | CARMA | This Work | 175 | 3 ± 0.6 | 0.12 ± 0.02 | CARMA | This Work |
| HNC(1-0) | 516 ± 38 | 55 ± 11 | 1.28 ± 0.26 | IRAM 30 m | Huettemeister et al. (1995) | ... | 14 ± 7 | 0.60 ± 0.30 | SEST | Aalto et al. (2002) |
| | ... | 34 ± 7 | 0.79 ± 0.16 | SEST | Aalto et al. (2002) | | | | | |
| | 407 | 43 ± 8 | 0.96 ± 0.19 | IRAM 30 m | Greve et al. (2009) | | | | | |
| | 400 | 53 ± 5 | 1.4 ± 0.13 | CARMA | This Work | 275 | 19 ± 4 | 0.89 ± 0.2 | CARMA | This Work |
| $HCO^+$(1-0) | ... | 20 ± 6 | 0.48 ± 0.14 | IRAM PdBI | Radford et al. (1991) | 420 | 21 ± 3 | 0.93 ± 0.13 | NMA | Nakanishi et al. (2005) |
| | ... | 19 ± 6 | 0.46 ± 0.14 | IRAM 30 m | Solomon et al. (1992a) | ... | 25 ± 8 | 1.11 ± 0.35 | IRAM 30 m | Graciá-Carpio et al. (2006) |
| | ... | 22 ± 7 | 0.53 ± 0.17 | IRAM 30 m | Graciá-Carpio et al. (2006) | | | | | |
| | 570 | 37 ± 4 | 1.0 ± 0.11 | CARMA | This Work | 470 | 40 ± 4 | 2.0 ± 0.19 | CARMA | This Work |
| $^{13}$CO(1-0) | 369 | 9 ± 2 | 0.14 ± 0.03 | IRAM 30 m | Greve et al. (2009) | | | | | |
| | 380 | 14 ± 2 | 0.24 ± 0.04 | CARMA | This Work | ... | ... | ... | ... | ... |
| H$^{13}$CN(1-0) | 400 | 15 ± 2 | 0.43 ± 0.06 | CARMA | This Work | ... | ... | ... | ... | ... |
| $^{13}$CS(2-1) | ... | ... | ... | ... | ... | ... | ... | ... | ... | ... |

## 3.3 Analysis & Discussion

### 3.3.1 High Density Molecular Gas traced in HCN, CS, HNC, and $HCO^+$

#### 3.3.1.1 Two Level Excitation with Photon Trapping

Scoville et al. (2015) adopted a two-level molecular system to determine the molecular hydrogen density, $n_{H2}$. We apply the same method here to determine the molecular hydrogen density, $n_{H2}$ using the properties each of the molecular species observed. We will be using the transitions HCN(1-0), CS(2-1), HNC(1-0) and $HCO^+$(1-0). Each of these molecules have a unique set of properties and therefore will give us insight into the density, temperature, and molecular abundance of the gas in these galaxies.

For the excitation analysis, we treat each transition, such as HCN(1-0), as a two-level molecular system with populations dictated by the collisional equilibrium with molecular hydrogen, $H_2$, the rate of spontaneous decay and photon absorption by the emission lines. $\tau$ is also assumed to be greater than one. Therefore, the population ratio of the upper and lower energy levels would be given by

$$\frac{n_u}{n_l} = \frac{n_{H2} < \sigma v >_{ul} g_{ul} e^{-h\nu/kT_k}}{n_{H2} < \sigma v >_{ul} + A_{ul}/\tau} \tag{3.2}$$

where $g_{ul}$ is the ratio of statistical weights, $\langle \sigma v \rangle_{ul}$ is the downward collision rate coefficient, $T_k$ is the kinetic temperature of the gas and $A_{ul}$ is the spontaneous decay rate. For more details see Scoville et al. (2015). The optical depth is given by

$$\tau = A_{ul} \frac{g_{ul} c^3}{8\pi\nu^3 dv/dr} n_l (1 - e^{-T_0/T_{ul}}) \tag{3.3}$$

We assume that the populations in the rotational levels would be typified by a single excitation temperature, $T_x$, which is then used to correlate the total molecular density, $n_m$ to the population in the lower energy level, $n_l$ through the Boltzmann distribution.

The molecules used in our analysis are all linear molecules; any transition J $\rightarrow$J - 1 has energy $E_l$ given by $E_l$ = h B ($J^2$ - J) and $T_0$ = h $\nu$/k = 2 h J B/k where B is the rotational constant for the molecules. The formulae, thus, used for our analysis are

$$\frac{T_x}{T_k} = \frac{1}{1 + \frac{T_k}{T_0} ln(1 + \psi f(T_x))} \tag{3.4}$$

where

$$\psi = \frac{64\pi (JB/c)^3}{(n_m/(dv/dr)) n_{H2} g_u < \sigma v >_{ul}} \tag{3.5}$$

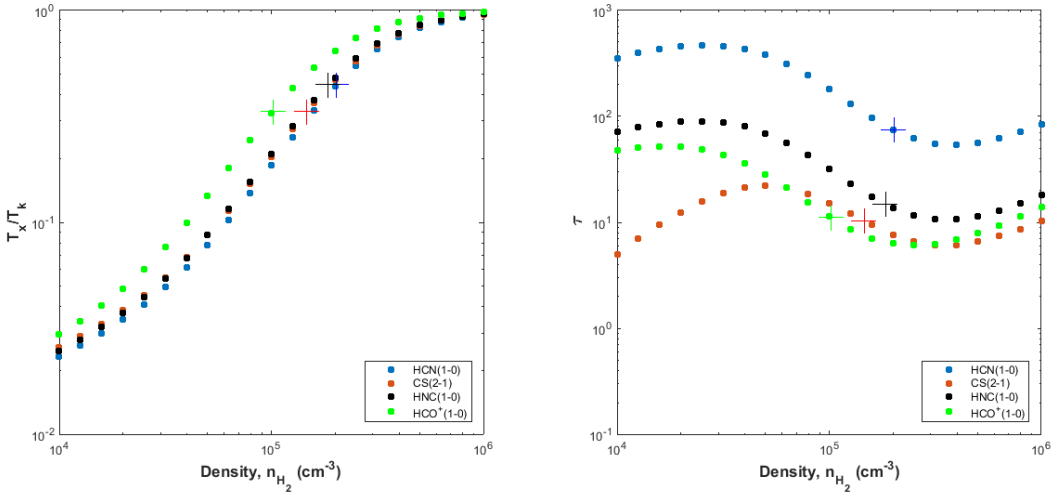


Figure 3.8: Arp 220: On the left, the ratio of the level excitation temperature to the gas kinetic temperature ($T_x/T_k$) on the abscissa and the density of HCN(1-0), CS(2-1), HNC(1-0), and HCO$^+$(1-0) lines which have been calculated from equations in Section 3.3.1.1. On the right, the optical depths of each of the lines are shown.

and

$$f(T_x) = \frac{kT_x/hB}{e^{-hB(J^2-J)/kT_x} - e^{-hB(J^2+J)/kT_x}} \tag{3.6}$$

Here dv/dr is the line of sight velocity gradient. The values used for these equations used in the following sections are collated in Table 3.3 for Arp 220 and NGC 6240.

Table 3.3: Constants used for Two Level Excitation with Photon Trapping for Arp 220 and NGC 6240

| | | | | | Arp 220 | | NGC 6240 | |
|---|---|---|---|---|---|---|---|---|
| Line | B | $A_{ul}$ | Abundance, X | $\langle\sigma v\rangle_{ul}$ | $T_b$ | dv/dr | $T_b$ | dv/dr |
| | GHz | $s^{-1}$ | Relative to $H_2$ | $s^{-1}$ | K | $s^{-1}$ | K | $s^{-1}$ |
| HCN(1-0) | 44.32 | 2.4 x $10^{-5}$ | 2 x $10^{-8}$ | 1.2 x $10^{-11}$ $(\frac{T_k}{50})^{-0.468}$ | 22.1 | 1.3 x $10^{-13}$ | 15.2 | 3 x $10^{-14}$ |
| CS(2-1) | 24.50 | 1.7 x $10^{-5}$ | 5 x $10^{-9}$ | 4.9 x $10^{-11}$ $(\frac{T_k}{50})^{-0.130}$ | 13.2 | 1 x $10^{-13}$ | 8 | 1.5 x $10^{-14}$ |
| HNC(1-0) | 45.33 | 2.7 x $10^{-5}$ | 4 x $10^{-9}$ | 7.6 x $10^{-11}$ $(\frac{T_k}{50})^{-0.196}$ | 22.8 | 1 x $10^{-13}$ | 10.4 | 2.3 x $10^{-14}$ |
| HCO$^+$(1-0) | 44.59 | 4.3 x $10^{-5}$ | 4 x $10^{-8}$ | 2x $10^{-9}$ $(\frac{T_k}{50})^{-0.152}$ | 14.4 | 1.3 x $10^{-13}$ | 19.1 | 4 x $10^{-14}$ |

#### 3.3.1.2 HCN(1-0) Excitation in Arp 220 and NGC 6240

The above described methodology can be used to estimate the gas density for each of the observed transitions in Arp 220 and NGC 6240. In the case of Arp 220, we estimated the nuclei to be ∼130

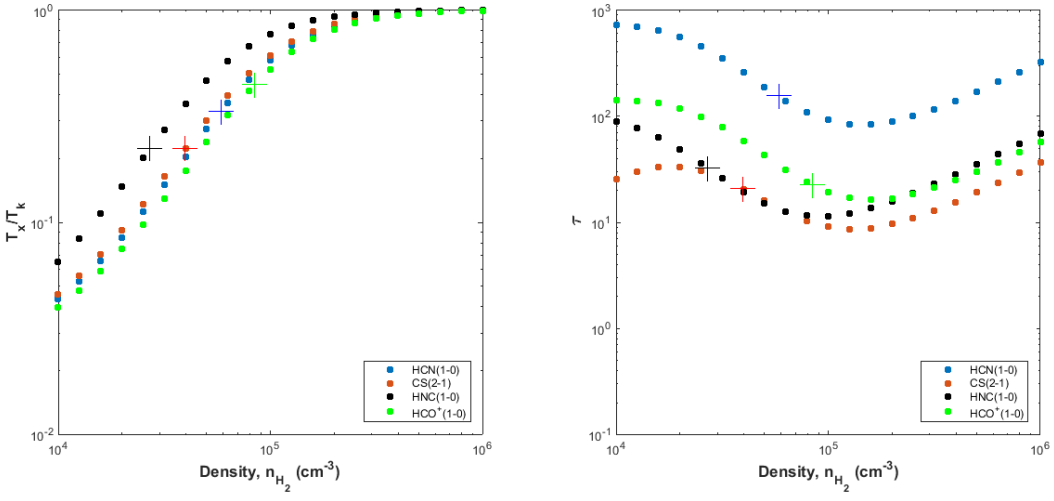


Figure 3.9: NGC 6240: On the left, the ratio of the level excitation temperature to the gas kinetic temperature ($T_x/T_k$) on the abscissa and the density of HCN(1-0), CS(2-1), HNC(1-0), and $HCO^+$(1-0) lines which have been calculated from equations in Section 3.3.1.1. On the right, the optical depths of each of the lines are shown.

pc in diameter and in the case of NGC 6240, we estimated it to be ∼380 pc. The FWHM of each transition in the respective galaxies was then used to calculate dv/dr. The number is listed in Table 3.3 for all transitions. We adopted a kinetic temperature of ∼45 K. This is from the dust temperature measured in IR from Sanders et al. (1991) for Arp 220 and NGC 6240. We are making this assumption because the dust and gas are in thermal equilibrium as shown in Goldreich & Kwan (1974). For HCN(1-0), the peak brightness temperature ∼20 K in Arp 220 and ∼15 K in NGC 6240. The line is expected to be optically thick and therefore this brightness temperature indicates an excitation temperature, $T_x$ ∼ 20-40 K for Arp 220 and ∼ 15-25 K for NGC 6240. Thus, the gas density would be derived for $T_x/T_k \backsimeq 0.44$ in Arp 220 and 0.33 in NGC 6240.

The values used for variables in the equations in section 3.3.1.1 such as B, $T_0$, $A_{1-0}$ etc. and hence to create the Fig. 3.8 and Fig. 3.9 are also provided in Table 3.3. The collision rate coefficients were calculated using the tables provided by Dumouchel et al. (2010) in the temperature range 20-100 K. The summed rate coefficient used for each of the transitons is also provided in Table 3.3. We assumed the abundance of HCN relative to molecular hydrogen, $H_2$ to be similar to that seen in Galactic clouds. Therefore, $X_{HCN} \sim 2 \times 10^{-8}$ (Bergin et al., 1996; Lahuis & van Dishoeck, 2000) and $n_m = X_{HCN} n_{H2}$.

The the ratio of the level excitation temperature to the gas kinetic temperature ($T_x/T_k$) as a

function of density $n_{H2}$ is shown in Fig. 3.8 and Fig. 3.9 with blue dots.

#### 3.3.1.3 CS(2-1) Excitation in Arp 220 and NGC 6240

For CS(2-1), the peak brightness temperature $\sim$ 13 K for Arp 220 and 8 K for NGC 6240. Thus, $T_x/T_k \backsimeq 0.3$ in Arp 220 and 0.2 in NGC 6240. Again, the various values of B, $T_0$, $A_{1-0}$ etc. are detailed in Table 3.3. The dv/dr has been calculated using the FWHM values measured from our observation (Table 3.2). In the case of CS, the galactic abundance has been observed to be $X_{CS}$ $\sim$ 5 x $10^{-9}$ (Paglione et al., 1995; Shirley et al., 2003; Bergin et al., 1997). The the ratio of the level excitation temperature to the gas kinetic temperature ($T_x/T_k$) as a function of density $n_{H2}$ is shown in Fig. 3.8 and Fig. 3.9 with red dots.

#### 3.3.1.4 HNC(1-0) Excitation in Arp 220 and NGC 6240

In the case of HNC(1-0), Graninger et al. (2014) postulate $X_{HNC} \sim X_{HCN}$. Therefore, we first assumed $X_{HNC} \sim 2$ x $10^{-8}$ for our calculations. However, assuming an abundance similar to HCN resullted in $n_{H2}$ that were too low to agree with measurements made using other molecular species. Therefore, we adjusted abundance of HNC to 5 times lower than previously assumed and redid our calculations to set $X_{HNC} \sim 4$ x $10^{-9}$. The lower abundance of HNC in contrast to HCN could be due to the destruction of HNC molecules at higher temperatures. The peak brightness temperature $\sim$ 22 K for Arp 220 and 10 K for NGC 6240. Thus, $T_x/T_k \backsimeq 0.4$ in Arp 220 and 0.2 in NGC 6240. The the ratio of the level excitation temperature to the gas kinetic temperature ($T_x/T_k$) as a function of density $n_{H2}$ is shown in Fig. 3.8 and Fig. 3.9 with black dots.

#### 3.3.1.5 $HCO^+$(1-0) Excitation in Arp 220 and NGC 6240

For $HCO^+$(1-0), the peak brightness temperature $\sim$ 14 K for Arp 220 and 19 K for NGC 6240. Thus, $T_x/T_k \backsimeq 0.3$ in Arp 220 and 0.4 in NGC 6240. We adopted the abundance of $HCO^+$ relative to molecular Hydrogen, $H_2$ to be twice that of HCN (Acharyya & Herbst, 2015). Hence, $X_{HCO^+} \sim$ 4 x $10^{-8}$. With this assumption we calculated $n_{H2}$ that were an order of magnitude lower than that measured by other molecular species. For the measurements to agree, we adjusted the abundance to $X_{HCO^+} \sim 4$ x $10^{-9}$. Abundance of $HCO^+$ would declines with increasing density as recombination is easier in denser regions. Therefore, the lower abundance could be the result of recombination in these galaxies. The the ratio of the level excitation temperature to the gas kinetic temperature ($T_x/T_k$) as a function of density $n_{H2}$ is shown in Fig. 3.8 and Fig. 3.9 with green dots.

#### 3.3.1.6 Densities Required for the Observed Emission

The left subplots in Fig. 3.8 and Fig. 3.9 show the ratio $T_x/T_k$ calculated for all the transitions in Arp 220 and NGC 6240. The observed values of $T_x/T_k$ measured for each transition, the values for

which have been mentioned in the previous sections, are shown as '+' on the plots. For the assumed abundances in Arp 220, the required densities, $n_{H2}$, are 2 x $10^5$ $cm^{-3}$ for HCN, 1 x $10^5$ $cm^{-3}$ for CS, 2 x $10^5$ $cm^{-3}$ for HNC, and 1 x $10^5$ $cm^{-3}$ for $HCO^+$. For the assumed abundances in NGC 6240, the required densities, $n_{H2}$, are 5 x $10^4$ $cm^{-3}$ for HCN, 4 x $10^4$ $cm^{-3}$ for CS, 3 x $10^4$ $cm^{-3}$ for HNC, and 8 x $10^4$ $cm^{-3}$ for $HCO^+$.

The right-side subplots in Fig.3.8 and Fig.3.9 show the line optical depth for each of the transitions as a function of density. The optical depths for the above mentioned densities are marked with '+' in the subplots. In the case of Arp 220, the optical depth, $\tau$ are 70 for HCN, 10 for CS, 15 for HNC, and 10 for $HCO^+$. For NGC 6240, the optical depth $\tau$ is 160 for HCN, 20 for CS, 30 for HNC, and 20 for $HCO^+$. Thus, these lines are optically thick, as assumed earlier for both galaxies. Its measured at over 100 for HCN in NGC 6240. $^{13}CO$ was not included in the model because $^{13}CO$ intensity measurements did not fit the model which has been used to model the other lines here as it yielded optical depths about one and $n_{H2} \sim 10^2$. This may imply either that the $^{13}CO/CO$ abundance is much lower than the galactic abundances or that the $^{13}CO$ emission is originating from a clumpy interstellar medium.

In Arp 220, measurements and calculations for all species produce similar molecular gas densities for the assumed abundances. The assumed abundances of HNC and $HCO^+$ were adjusted as molecular hydrogen densities would not agree otherwise. The $n_{H2}$ should not be dissimilar within each galaxy. Since $n_{H2}$ should constant regardless of which molecular species was used to make the estimate, it suggests that the abundances that have been measured for galactic sources are not always correct for ULIRGs.

In the case of NGC 6240, we assumed the same adjusted abundances as done for Arp 220. All the transitions indicate molecular gas densities within a factor of 2 for these assumed abundances. As in the case of Arp 220, HNC and $HCO^+$ calculated $n_{H2}$ with adjusted abundances agree more with HCN densities.

In chapter 5, we will discuss a fully correct multi-level equiibrium analysis to calculate the molecular hydrogen densities in these galaxies using the Large Velocity Gradient or Sobolev formalism to treat the radiative transfer for molecular excitation.

### 3.3.2 HCN and HNC line ratios: XDR vs PDR regions

#### 3.3.2.1 HCN and HNC: Line Chemistry

Observations of HCN and HNC in various molecular clouds within the galaxy (Goldsmith et al., 1981; Hirota et al., 1998) as well as in other galaxies (Pérez-Beaupuits et al., 2007), along with theoretical modeling of chemistry of steady-state molecular gas (Schilke et al., 1992; Meijerink & Spaans, 2005) have been used to understand the physical conditions and chemistry dense molecular

gas in galaxies in the local universe and at high redshift. The ratios of their flux densities and/or luminosities can be used to infer temperatures, densities, and environments of the molecular gas. These ratios can be especially enlightening while studying ULIRGs in the view of the fact that star formation is going on in these galaxies at high rates. The inferred temperatures, densities, and physical properties of the star forming molecular gas can inform our models of star formation and further our understanding of the conditions required for starbursts. Arp 220 and NGC 6240 are excellent laboratories for these studies, given their ULIRG status and differences in their merging stage. Observing emission lines from tautomers HCN and HNC can provide us valuable information about the chemistry of the ISM in these galaxies. Dense gas at low temperature conditions can enhance the HCN/HNC ratio.

Both Hydrogen Cyanide (HCN) and Hydrogen Isocyanide (HNC) have similar dipole moments, $\mu_{HCN}$=3.05 Debye and $\mu_{HNC}$=2.98 Debye. Since both have large dipole moments, their emission lines are easily observed in the ISM provided the gas has excitation conditions (high gas density and/or high optical depth. As a result, lines from both molecules are regularly used as diagnostics to study high excitation molecular gas both inside our galaxy and in other galaxies. As HNC has a higher binding energy than HCN ( 4000 $cm^{-1}$), it would be expected that at low temperatures (T<100 K) HCN would be much more abundant than HNC ([HNC]/[HCN]<$10^{-25}$). But this is not what is observed in our galaxy and in extragalactic observations. The abundance ratio at low temperatures and high densities reaches unity. This is due to the large amount of energy required for the tautomerization reaction to happen. The activation barrier is of the order of 10000 $cm^{-1}$. This would occur at temperatures high enough for the HNC molecule to be easily destroyed by other reactions. As a result, the HNC abundance which matches the HCN abundances at high densities and low temperatures can be easily observed in these conditions.

If the HCN and HNC emission arises from gas of densities n($H_2$)>$10^5$ $cm^{-3}$ then the HNC chemistry would be dominated by reactions like HNC+O$\longrightarrow$CO+NH which would destroy HNC at higher temperatures. Thus, at high gas densities, a bright HNC line would imply a considerable amount of cold ($T_k$ < 24 K) dense gas. These are the conditions that are expected in the dense molecular gas clouds where a lot of the star formation is happening.

#### 3.3.2.2 PDR and XDR: An Introduction

The HCN and HNC ratios provide constraints on the temperature and density of the molecular gas but and the environment of the gas in these galaxies. An important aspect is whether is the region in the galaxy is Photon dominated or X-ray dominated, that is if the region is a Photon Dominated Region (PDR) or a X-ray Dominated Region (XDR). Differentiating between these is insightful as the former would imply that the molecular gas is mainly radiated by extreme star formation while the latter would imply that the molecular gas is irradiated by an AGN nucleus. Since it is not always

clear if there is an obscured AGN nuclei in the core of a galaxy, this can be a valuable insight into the nature of the lumonsity source.

Photon Dominated Regions or Photon Dissociation Regions (PDRs) are characterized by the irradiation of molecular gas clouds in star forming regions by Far-Ultraviolet (FUV) radiation emitted by young, nearby, OB type stars. O and B stars dominate the radiation from starbursts, which is mostly in the far-ultraviolet (6.0<E<13.6 eV), turning cloud surfaces into Photon Dominated Regions (PDRs) (Tielens & Hollenbach, 1985). Since a starburst galaxy will be populated by a large number of OB stars, it would be expected that the molecular gas in such regions would be dominated by PDR chemistry. FUV photons dominate the ionization and spectral properties and physical conditions such as temperature and densities especially on the surface of the molecular clouds.

The first theoretical models for PDRs were presented in the paper Tielens & Hollenbach (1985). Subsequently, many others have expanded on the theoretical predictions of spectral properties of these regions. Most of these models assume a semi-infinite plane-parallel slab where one side is illuminated by UV radiation and the interior of the slab emits the cooling lines. Using these assumptions, the temperature profile and chemical composition of the PDR are evaluated, and this includes the cooling line intensities.

Depending on assumptions such as hydrogen particle density, $n_H$, and the UV field, large differences can be seen in the chemical and physical structure of the PDR and can be used to model a typical set of observable line intensities. Many of these PDR models have successfully explained the observed line integrated intensities of the low- and mid-J rotational lines of the molecules and the [CII] line both in galactic sources (star formations regions) and external galaxies (Wolfire et al., 1989; Stacey et al., 1991).

An excellent summary of the physical processes that affect the properties of PDRs is provided in Meijerink & Spaans (2005). These include heating through photo-electric emission by dust grains and PAHs (for example Bakes & Tielens (1994)), heating caused by FUV pumping of $H_2$, fine-structure line cooling of [CI] 609, [CII] 158, [OI] 146 and 63 $\mu$m (Tielens & Hollenbach, 1985) etc. For more details, see Meijerink & Spaans (2005) and Meijerink et al. (2007).

X-ray Dominated Regions or X-ray Dissociation Regions (XDRs) are characterized by the irradiation of molecular gas clouds by intense X-ray fluxes. Molecular gas can be irradiated by X-rays in a number of different astrophysical scenarios such as near Active Galactic Nuclei (AGNs), Supernovae remnants and X-ray binaries. The most dominant source of X-rays in ULIRGs such as Arp 220 and NGC 6240, which have supermassive accreting black holes, would be the AGNs. AGNs are capable of producing hard X-ray photons (energies $>$ 1 keV), which can penetrate through large column densities (of the order of $10^{22}$ cm$^{-2}$) before being absorbed by the molecular gas because of the large energy per photon present in the radiation (Maloney et al., 1996). This can strongly alter

the chemical and thermal properties of the clouds that are opaque to other kinds of radiation. The effects of X-ray irradiation can also result in infrared and submillimeter emission from the irradiated molecular clouds. By observing these effects, the presence of a XDR (indicating perhaps the existence of an obscured AGN) can be deduced. Many investigations into the properties of XDRs have been done over the years (Krolik & Kallman, 1983; Lepp & McCray, 1983; Bakes & Tielens, 1994; Maloney et al., 1996). More recent studies (Meijerink & Spaans, 2005; Meijerink et al., 2007), have updated models including vast range of densities and temperatures; these models are able to make predictions for the emission lines of molecular species such as $HCO^+$, HCN, HNC, CS, and fine structure lines like [CII], [OI]. Thus, using the models along with observations of emission lines of molecular species mentioned earlier, one can probe the environment of the molecular gas in these systems and the nature of the energy sources.

#### 3.3.2.3 PDR and XDR: Models

A starting point for many of these models is the assumption that many of the astrophysical sources producing the X-rays, can be represented by a mostly flat spectral energy distribution (for example, the power law continuum expected from AGNs (Maloney et al., 1996)). As a result, the energy from these X-ray photons will not be absorbed till the UV photons in the regions have been absorbed and only then will they affect the physical conditions of the gas. PDRs are limited to column densities of the order of $10^{21}$ $cm^{-2}$ because the presence of dust will inhibit absorption at higher column densities. Therefore, if both UV and X-ray sources irradiate the molecular gas with mostly flat spectral distributions, XDR conditions would dominate for higher column densities. The XDR and PDR models we are using to understand the spectral environment of the molecular gas have been developed by R. Meijerink and M. Spaans (Meijerink & Spaans, 2005; Meijerink et al., 2007). In these models, they explain that while in XDRs the molecular gas is mostly heated directly by the ionization of the gas by the photons; that is not the case in PDRs. As a result, free electrons are produced in XDRs, which lose energy by collisions with the surrounding electrons, atoms, and molecules. In XDRs, a different set of processes play major roles (Meijerink & Spaans, 2005). There is also cooling through molecular lines from warm ISM containing chemical species such as CO, $H_2$, etc.

In Meijerink et al. (2007), the authors used what was called 'Standard clouds' with different physical properties to explore the detailed column density dependencies of the line ratios such as HCN/CO, HNC/HCN, HCO+/HCN, CS/HCN, etc. as function of the densities of the molecular gas for both PDRs and XDRs. Table 3.4 shows the properties that have been used for these cloud simulations, adopted from the paper Meijerink et al. (2007). In this table, UV radiation field (6-13.6 eV) is expressed in multiples of the Habing flux, where $G_0 = 1$ corresponds to $1.6 \times 10^3$ $s^{-1}$ $cm^{-2}$ (the local Galactic interstellar radiation field). $F_X$ is the X-ray flux in erg $s^{-1}$ $cm^{-2}$. As explained

in this paper, an active Super-Massive Black Hole (SMBH) producing an X-ray luminosity of $10^{44}$ erg $s^{-1}$, produces a flux of 100 erg $cm^{-2}$ at a distance of 100 pc, assuming no extinction. Therefore, Standard cloud type A is similar to a compact, high-density environment found in molecular cloud cores, and clouds very close to active nuclei, whereas cloud type B is a more traditional molecular cloud environment, and cloud type C is similar to the more diffuse extended (molecular) medium in which clouds of type B would be embedded. For our studies, Cloud type A and B would more closely resemble the molecular gas we are observing. Molecular species such as HCN, $HCO^+$, CS, etc. are expected to be in high abundances in regions of high densities in these molecular clouds. Hence, using metrics that depend on emission from these molecules, it is expected that we are observing dense molecular gas clouds that correspond to the cloud types A and B, which will henceforth be referred to as high density regions or mid density regions, respectively. A similar format is followed in the the above mentioned paper.

Table 3.4: Standard Cloud Properties from Meijerink et al. (2007)

| Type | r(pc) | n($cm^{-3}$) | N($cm^{-3}$) | $G_0$ | $F_X$ [erg $s^{-1}$ $cm^{-2}$] |
|---|---|---|---|---|---|
| A | 1 | $10^4$-$10^{6.5}$ | $3 \times 10^{22}$-$1 \times 10^{25}$ | $10^2$-$10^5$ | 1.6 - 160 |
| B | 10 | $10^3$-$10^4$ | $3 \times 10^{22}$-$1 \times 10^{23}$ | $10^1$-$10^4$ | $1.6 \times 10^{-1}$ - 16 |
| C | 10 | $10^2$-$10^3$ | $3 \times 10^{21}$-$1 \times 10^{22}$ | $10^{0.5}$-$10^3$ | $1.6 \times 10^{-2}$ - 1.6 |

Some of the results from the paper Meijerink et al. (2007) are included here for ease of access (Fig. 3.10- 3.13).

#### 3.3.2.4 ARP 220 and NGC 6240: PDR or XDR?

From X-ray observations of both Arp 220 and NGC 6240, studies have been able to detect the presence of Active Galactic Nuclei. Since both are merging systems, it is deduced that they both have Supermassive Black Holes (SMBHs). While these systems are at different merging states, they have not gone through the coalescing stage which would include the merger of the black holes at their cores. In Arp 220, we clearly observe two counter-rotating disks of gas, both of which probably have black holes at their centers. The presence of at least one black hole has been indicated from observations (Clements et al., 2002; McDowell et al., 2003), the presence of another one in the other counter rotating disk has yet to be detected. In the case of NGC 6240, the presence of two black holes has been detected (Komossa et al. (2003), Fig. 1.4) using Chandra X-Ray Observatory. Using the molecular emission line measurements, we might be able to detect the presence of SMBHs in the midst of the molecular gas if the molecular clouds are being irradiated by the XDR conditions emitted by the AGN. Given the very high column densities of dust, the absence of the optical emission line ratios characteristic of AGN does not preclude the presence of a SMBH, the line ratio

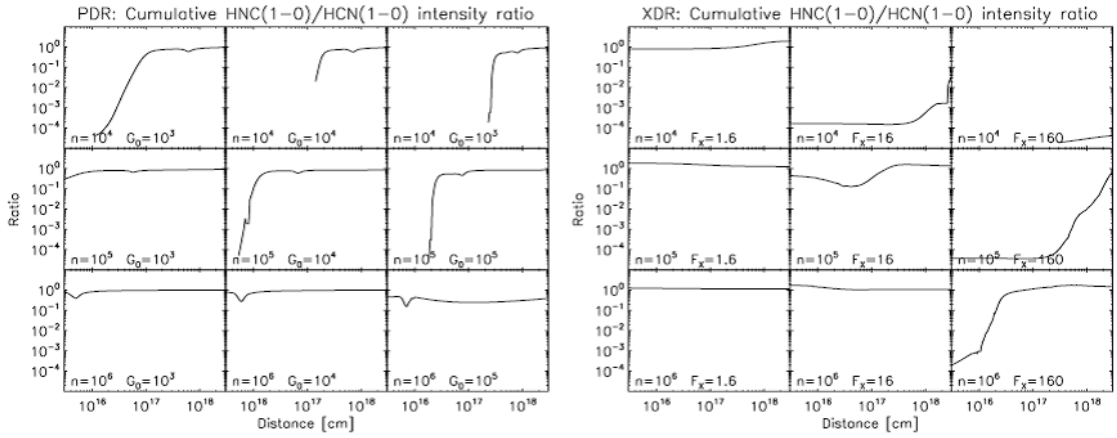


Figure 3.10: Cumulative HNC(1-0)/HCN(1-0) line intensity ratios for PDR (left) and XDR (right) (Meijerink et al., 2007). In PDRs HCN is more abundant in the radical region. However, in the denser cores of the clouds the abundance approaches unity. In XDRs, HCN has higher abundance in the highly ionized parts of the cloud. Therefore, in PDRs, HCN(1-0)/HNC(1-0) line intensity ratio is around one if column densities are larger than $10^{22}$ cm$^{-2}$ and greater than one for lower densities. In XDRs, the ratios decrease for lower radiation fields and as density increase (n$\rightarrow 10^{6.5}$cm$^{-3}$), the line ratios are always less than one.

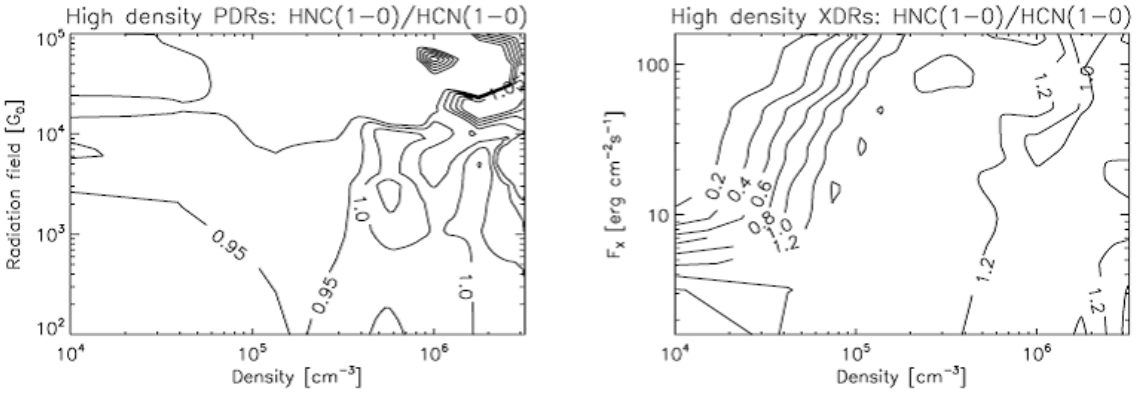


Figure 3.11: HNC(1-0)/HCN(1-0) ratio for PDR (left) and XDR (right) models (Meijerink et al., 2007). From comparison of these plots one can conclude that the low HNC/HCN intensity ratio occur only in the XDR regions and at low density.

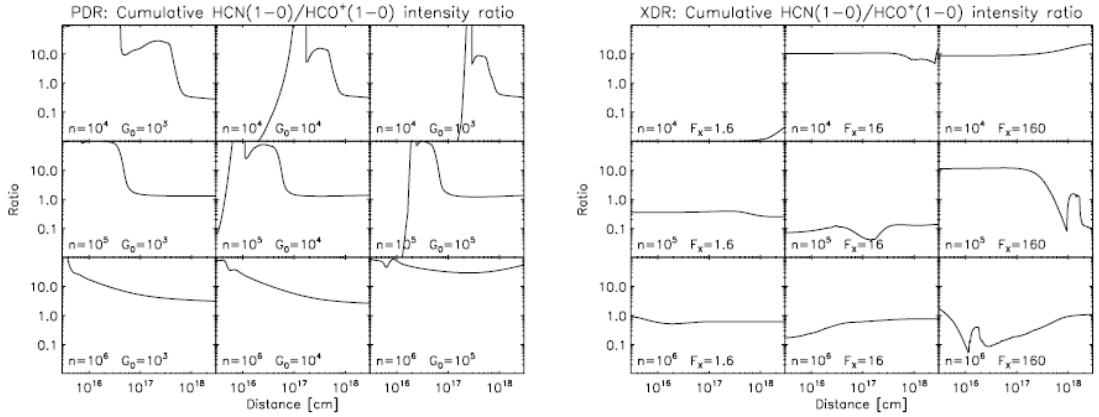


Figure 3.12: Cumulative HCN(1-0)/$HCO^+$(1-0) line intensity ratios for PDR (left) and XDR (right) (Meijerink et al., 2007). The radiation field affects the HCN and $HCO^+$ abundance. They are more abundant at PDR edge of the cloud. At higher densities, inside the cloud, HCN and $HCO^+$ abundance first increase and then become constant. At high enough densities and columns, the HCN(1-0)/$HCO^+$(1-0) line intensity ratio are larger than one. In XDRs, $HCO^+$ is less abundant than HCN. At higher column densities, $HCO^+$ becomes more abundant and eventually, has larger abundances than HCN.

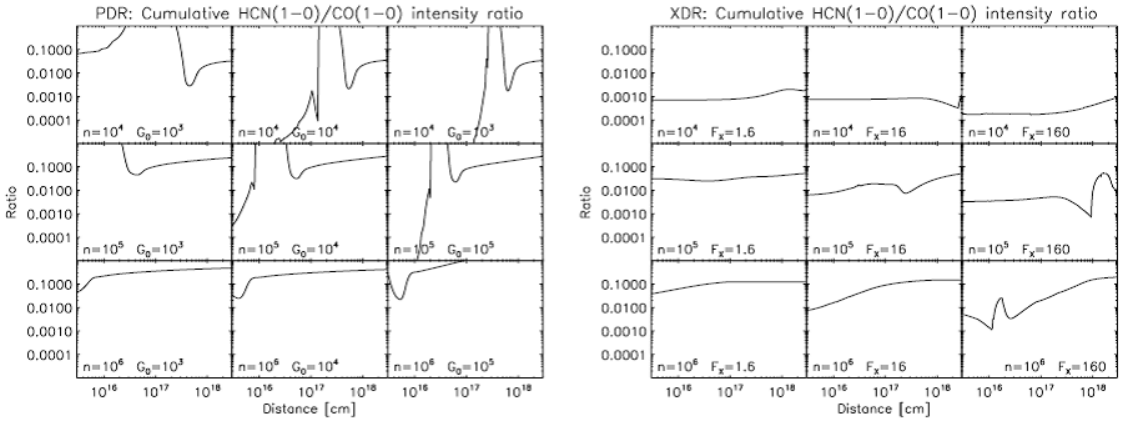


Figure 3.13: Cumulative HCN(1-0)/CO(1-0) line intensity ratios for PDR (left) and XDR (right) (Meijerink et al., 2007). Here the ratios are calculated for cloud type A. There is more variation in these ratios because of the high critical densities of the HCN transition. The HCN(1-0)/CO(1-0) line intensity ratios are large in PDRs at high densities (n $>10^6 cm^{-3}$) and can be greater than one. However, in XDRs, the ratios are around 0.1-0.2.

measurements for the molecular species consistent with the XDR models would be a very strong indicator to its presence.

The densities of molecular gas that we are probing using high density gas tracers like HCN, HNC, and CS are expected to be of the order of $10^4$ cm$^{-3}$ to $10^6$ cm$^{-3}$. As mentioned earlier, HCN and HNC molecules have very similar critical densities because of their similar dipole moments. Therefore, the line ratios would be very indicative of the difference of their abundance and the environment of the molecular gas. The models of XDRs indicate that the HCN/HNC column density ratio is diminished (and lower than unity) compared to PDRs and quiescent cloud regions for gas densities around $10^5$ cm$^{-3}$. Steady-state excitation models show that the abundance of HCN and its isotopomer HNC decreases with increasing density and temperature (Schilke et al., 1992). Values for the HCN/HNC abundance ratio above unity are consistent with steady-state models for higher-density gas at higher temperatures (Fig. 3.10 and 3.11). An HNC/HCN abundance ratio lower than unity suggests a rather quiescent, low temperature gas.

At higher temperatures HNC tends to be selectively destroyed in favor of HCN as long as the medium is not highly ionized. Therefore, HCN/HNC is roughly unity in PDR sources, but lower than unity in XDR sources. The HNC/HCN abundance ratio ratio is expected to be around 0.9, if the standard neutral production paths are followed (Goldsmith et al., 1981). In a highly ionized medium, high HCN/HNC ratios would be prevented since $HCNH^+$ can form HCN and HNC with equal probability (Aalto et al., 2002; Wang et al., 2004). Shocks can selectively destroy HNC and could significantly increase the steady-state HCN/HNC abundance ratio (Schilke et al., 1992). Both HCN and HNC may be pumped by an intense mid-IR radiation field boosting the emission also from low density regions where the lines would not be collisionally excited. For HNC the interaction with the IR radiation is even stronger than for HCN, thus increasing the likelihood for IR pumping in extreme IR galaxies

Table 5.3 displays the HCN/HNC line intensity ratios for the 1–0 transition for Arp 220 and NGC 6240 compiled with ratios from other sources such as Seyferts, liners and Galactic Molecular Clouds (GMCs) for comparison. The uncertainty in the line ratios for our measurements are based on the uncertainty in our flux observations that have been propagated through the ratio.

The dichotomy in the measurements for Arp 220 and NGC 6240 can be clearly seen. While the HCN/HNC ratio is less than unity for Arp 220, that is not the case for NGC 6240. The ratio for Arp 220 is clearly less than unity. As discussed before in this section, a ratio less than unity indicates the presence of a strongly irradiated XDR, possibly by an AGN, at the cores of the Arp 220. In section 3.3.2.3, the profiles and relatives strengths of the peaks for the molecular lines were discussed. Since HNC is a strong line in both the nuclei as compared to HCN, there is a clear indication that both nuclei might house an AGN irradiating the molecular gas.

In comparison, NGC 6240, which is known to have two AGN detected by other observations,

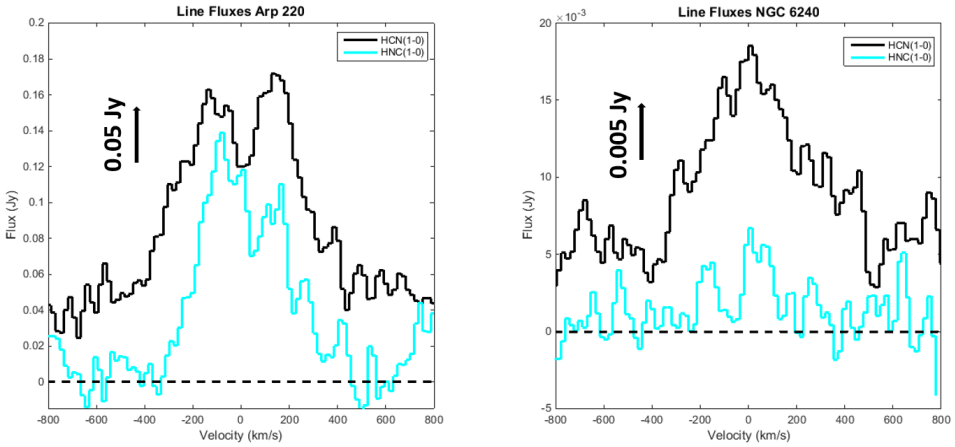


Figure 3.14: Overlaid HCN(1-0) and HNC(1-0) emission lines for Arp 220 and NGC 6240, respectively. For Arp 220 has the two emission lines separated by 0.05 Jy for easier viewing. For NGC 6240 has the two emission lines separated by 0.005 Jy for easier viewing.

displays a line ratio higher than unity. Such a ratio is expected from molecular gas with PDR conditions. That is not to say that a XDR does not exist within the galaxy. It only indicates that the molecular gas clouds we are observing have been mostly been irradiated by radiation originating from star forming regions. The ratio observed in NGC 6240 is very similar to other known star forming galaxies as shown in Table 5.3. This is consistent with the fact that the molecular gas peak lies between the two nuclei and not on top of them.

In summary, the diminished HCN/HNC ratio in Arp 220 may indicate the presence of an XDR being associated with an AGN.

Table 3.5: HCN and HNC Line Ratios for Arp 220 and NGC 6240

| Galaxy | $\frac{\text{HCN(1–0)}}{\text{HNC(1–0)}}$ | Reference |
|---|---|---|
| NGC 3079 | 2.15 ± 0.67 | Pérez-Beaupuits et al. (2007) |
| NGC 1068 | 2.01 ± 0.65 | Pérez-Beaupuits et al. (2007) |
| NGC 2623 | 1.4 | Aalto et al. (2002) |
| NGC 1365 | 1.35 ± 0.37 | Pérez-Beaupuits et al. (2007) |
| NGC 7469 | 1.50 ± 0.57 | Pérez-Beaupuits et al. (2007) |
| L1489 | 0.83 ± 0.17 | Hirota et al. (1998) |
| L1521B | 0.5 ± 0.12 | Hirota et al. (1998) |
| ARP 220 | 0.79 ± 0.1 | This Work |
| NGC 6240 | 1.39 ± 0.2 | This Work |

### 3.3.3 HCN and $HCO^+$ Ratios

A goal of this thesis has been to study the dense molecular gas present in the ULIRGs Arp 220 and NGC 6240. These galaxies have been widely studied using the multitransitional CO observations which trace both high and lower density regimes of the molecular gas. HCN observations have often been used to selectively probe the highest density gas. Graciá-Carpio et al. (2006) suggest that HCN might not be the best tracer for the very dense gas and others have argued that the HCN abundance may be enhanced by obscured AGN (Kohno et al., 2001; Usero et al., 2004) or excited by IR pumping in vibrational transitions (Aalto et al., 1995). $HCO^+$ has been proposed as an alternative tracer of dense gas.

Both the $HCO^+$ and HCN J=1-0 transition lines have very similar critical densities. These lines are expected to arise from the dense molecular gas with densities, $n_H \geq 10^4$ cm$^{-3}$. These molecular species are better tracers of dense gas, as their dipole moments ($\mu > 3$ D, Imanishi et al. (2007)) are an order of magnitude larger than the widely used CO molecular ($\mu \sim 0.1$ D).

#### 3.3.3.1 Empirical Models and Diagnostics

Kohno et al. (2001) proposed another diagnostic method to probe the presence of an obscured AGN in the molecular disks of LIRGs and ULIRGs. Direct X-ray observations are not always possible to detect these AGNs. Therefore, the chemical effects of the X-ray radiation on the surrounding medium would be the most effective method to probe the presence of an AGN. In effect, this is another method to probe whether the observed molecular lines are originating from a PDR and therefore a starburst/star formation driven region, or from an XDR, associated with an AGN.

Models such as those by Maloney et al. (1996) suggest that in XDRs there is a diminished $HCO^+$ abundance. Thus, an increased HCN/$HCO^+$ line ratio would be expected in a XDR. Observations by Kohno et al. (2001) measured the HCN/$HCO^+$ ratio in the J=1-0 transitions and compared these ratios for a sample of Seyfert and Starburst galaxies. They observed that the ratio is low, i.e. significantly elevated $HCO^+$ fluxes compared to HCN, in the case of starbursts. These results are reproduced in Fig. 3.15.

With our observations of these galaxies, which have been performed simultaneously using the same array configurations of CARMA, these molecular transition lines have the same beam patterns and therefore probe similar regions in the galaxies. As all the line fluxes have been measured using the same correlator configuration and same receivers, taking ratios to perform diagnostics cancels out the uncertainty from any calibration uncertainties.

Fig. 3.16 shows the HCN(1-0)/$HCO^+$(1-0) brigthness temperature ratio on the y-axis and the HCN(1-0)/CO(1-0) brightness temperature ratio on the x-axis. Brightness temperature ratios have been used here to make comparison with previous studies simpler. The figure also has ratios mea-

sured by other studies of Seyferts and Starbursts (Kohno et al., 2001; Kohno, 2005; Imanishi et al., 2004, 2006, 2007). All of the observations for HCN(1-0) and $HCO^+$(1-0) in these studies were done using the Nobeyama Millimeter Array (NMA) and the Rainbow interferometer. Some of the CO(1-0) observations were taken from other studies. For HII regions within our galaxy, the measurements were done by Turner & Thaddeus (1977) and Pirogov (1999).

#### 3.3.3.2 Interpretation and Analysis of the Brightness Temperature Ratios

Kohno et al. (2001) and Kohno (2005) found empirically that galaxies dominated by AGNs, displayed higher HCN/$HCO^+$ and HCN/CO ratios than galaxies that were were dominated by starbursts. Thus, AGN dominated galaxies were expected to be in the upper right section of the Fig. 3.15 and 3.16, whereas the starburts would reside in the lower left.

The HCN/CO ratio increases due to the increased HCN abundance as compared to CO in XDRs (Lepp & Dalgarno, 1996). Also, the HCN abundance would be enhanced in dense molecular clouds because of the disparity in the dipole moments of HCN and CO. Many studies have shown that there is an enhancement in the HCN/CO brightness temperature ratios when galaxies contained a larger fraction of high density molecular gas (e.g. Solomon et al. (1992b); Curran (2000). Sanders & Mirabel (1996) also showed that ULIRGs displayed a higher fraction of dense gas than the less IR luminous galaxies. Therefore, high HCN/CO ratios would be expected from ULIRGs, despite the presence of XDRs. Thus, the HCN/CO ratios alone would not form a strong enough diagnostic for the presence of AGNs.

Thus, the use of HCN/$HCO^+$ along with HCN/CO ratios will prove more robust. Since both HCN and $HCO^+$ have high dipole moments, they both probe high density molecular gas, and therefore their ratio would not be as affected by differences in the fractions of dense molecular gas.

High ratios of HCN/$HCO^+$ are expected if the HCN abundance is enhanced by different processes, such as X-ray radiation by an AGN source (Lintott & Viti, 2006). In the case when both the HCN(1-0) and $HCO^+$ emission are optically thin, it would be expected that the HCN(1-0)/$HCO^+$(1-0) ratio would increase as the HCN abundance relative to $HCO^+$ increases. Imanishi et al. (2006, 2007) showed that even if emission from these molecular species was reasonably optically thick, the enhancement of HCN abundance would increase the HCN/$HCO^+$(1-0).

If the ratios of HCN/$HCO^+$ and HCN/CO are such that a galaxy resides in the upper right corner of the plot, it would give a strong indication that an AGN is present. However, if the ratios put the galaxy in the lower left corner, it does not automatically imply that an active AGN is not present in the galaxy since this could be a case of a composite AGN and starburst galaxy.

In an earlier section, we discussed our observations of both HCN and $HCO^+$ in the ULIRGs Arp 220 and NGC 6240. $HCO^+$(1-0) is a strong emission line in both these galaxies in comparison to HCN(1-0). This can be seen clearly in Fig. 3.16, where HCN(1-0) and $HCO^+$(1-0) lines are overlaid

for both Arp 220 and NGC 6240. As a result of the strong $HCO^+$ emission line, the HCN/$HCO^+$ ratio in both Arp 220 and NGC 6240 is low. Therefore, these galaxies fall in the lower left portion of Fig. 3.16. They are denoted by a red inverted triangle and green star on the plot while measurements done by Imanishi et al. (2007) are shown by blue dots. Other observations shown as filled black dots in the case of starbursts and black circles for Seyfert galaxies.

In this figure, there are also separate points for Arp 220W and Arp 220E. The observations for HCN and $HCO^+$ were performed by Imanishi et al. (2007), while the CO measurements were done by previous studies of Arp 220. The authors fit Gaussians to the HCN and $HCO^+$ line profiles to measure fluxes separately for the two nuclei. We did not do this, since it would mean we are interpreting the two peaks as emission each coming solely from one of the two nuclei. The CO line profile is more difficult to resolve into two peaks. Therefore, to divide flux from the two nuclei to make such an interpretation might not be the correct route. As a result, our measurements differ from those in Imanishi et al. (2007).

Both Arp 220 and NGC 6240 fall in the lower left portion of the plot, indicating high rates of star formation. The fact that neither occupy the upper right section, does not automatically imply the absence of AGNs. This would especially hold in the case of NGC 6240, where two AGNs have been identified using X-ray (Komossa et al., 2003). Thus, the fact that NGC 6240 ratios do not occupy the 'pure AGN' section of the plot does not imply that AGNs are not present since the starbursts may dominate the AGN and in the case of NGC 6240, the molecular gas peak is offset from both nuclei and their X-ray sources. This could easily be the case for Arp 220 as well.

Imanishi et al. (2007) made a plot with HCN(1-0)/$HCO^+$(1-0) brightness temperature ratios from different sources along with HCN and $HCO^+$ line widths. The plot has been reproduced in Fig. 3.17 here with our measurements of Arp 220 and NGC 6240 plotted also. There is no significant correlation of the line ratios with line widths.

#### 3.3.3.3 $HCO^+$(1-0) as an indicator of Star Formation

An interesting outcome of these observations is the strong $HCO^+$ emission lines observed both in Arp 220 and NGC 6240. There have not been a lot of studies that explain the presence of strong $HCO^+$ emission lines in ULIRGs, beyond its use as a high density gas tracer. While $HCO^+$ has been used in line ratios as explained in the previous section, its chemistry is not unique enough to specify any other physical conditions or chemistry of the molecular gas.

In the case of Arp 220 and NGC 6240, the fact that we see strong $HCO^+$(1-0) emission lines indicates that free electron abundances is not high enough to cause the ion to dissociate, and neither is cosmic ray induced dissociation. Papadopoulos (2007) suggests that turbulence reduces the abundance of $HCO^+$. Abundance ratios of HCN/ $HCO^+ > 1$ would not correlate directly to the line ratios for similar transition levels for these molecules as their chemistry is not entirely similar.

As mentioned by Papadopoulos (2007), their $E_u/k_b$ values are similar but the critical density of HCN is 5-7 times that of $HCO^+$ for J=1-0 transition. Therefore, $HCO^+$ will be a brighter line even if HCN is more abundant. This might very well explain the presence of a bright $HCO^+$ line in our observations of NGC 6240 and Arp 220.

Higher transitions of $HCO^+$ have been used to identify regions of star formation in some studies. For example, in Sakamoto et al. (2009), authors observed $HCO^+$(3-2) and $HCO^+$(4-3) transitions using the Submillimeter Array(SMA) along with observations of CO(3-2) of Arp 220. They observed P Cygni line profiles for CO(3-2) with absorption at the blueshifted velocities of $HCO^+$ emission lines. They suggest that P Cygni profiles are a result of 100 km $s^{-1}$ outflows of molecular gas from the nuclei. They also suggest that these outflows are winds driven by starbursts. These emission lines are strongly centered around the nuclei (Fig 1. in Sakamoto et al. (2009)). This is very similar to the $HCO^+$ emission topography seen in our observations. While it is not expected that higher $HCO^+$ transitions will map exactly the same region as $HCO^+$(1-0) transition, the correlation of higher transition $HCO^+$ emission and absorption in starburst driven winds implies a correlation of the presence of a $HCO^+$ with rapid star formation.

The low HCN/ $HCO^+$ ratios suggests that an extreme starburst dominated by young hot stars do not easily produce a high HCN/$HCO^+$ ratios. It might also indicate that the HCN and $HCO^+$ emission lines are not originating in similar/the same regions and we are sampling regions of dense gas with a range of physical conditions across the ULIRGs. Therefore, more extensive and higher resolution imaging of these galaxies in these emission lines needs to be done. We will discuss higher resolution imaging from CARMA in the next chapter.

### 3.3.4 Isotopomer Line Ratios

Table 3.6 shows the isotopomer line ratios for both Arp 220 and NGC 6240. These include line intensity ratios CO(1-0)/$^{13}$CO(1-0)($\Re_{1--0}$) and HCN(1-0)/H$^{13}$CN(1-0). The isotopomer lines $^{13}$CO(1-0) and H$^{13}$CN(1-0) for NGC 6240 were not significantly detected and only limits can be ascertained from the data. This section will focus only on Arp 220 where we have definite detections.

Isotopomer lines such as $^{13}$CO(1-0) have been more readily observed in ULIRGs. Casoli et al. (1992) proposed that the missing $^{13}$CO(1-0) in other lower luminosity systems was due to top-heavy initial stellar mass functions that could be found in these extreme systems. Another explanation could be optical depth effects being caused by molecular gas that is turbulent and warmer than the expected temperatures in star forming regions (Aalto et al., 1995). Aalto et al. (1995) proposed that $\Re_{1--0} > 20$ (as seen in Arp 220) would be found in molecular gas which is at very high pressures in the interior cores of the merging luminous galaxies. The authors point out that the optical depth of CO(1-0) transition will be reduced at high gas temperatures since the molecules are more widely distributed over the rotational levels. The optical depth will also be reduced for low density gas,

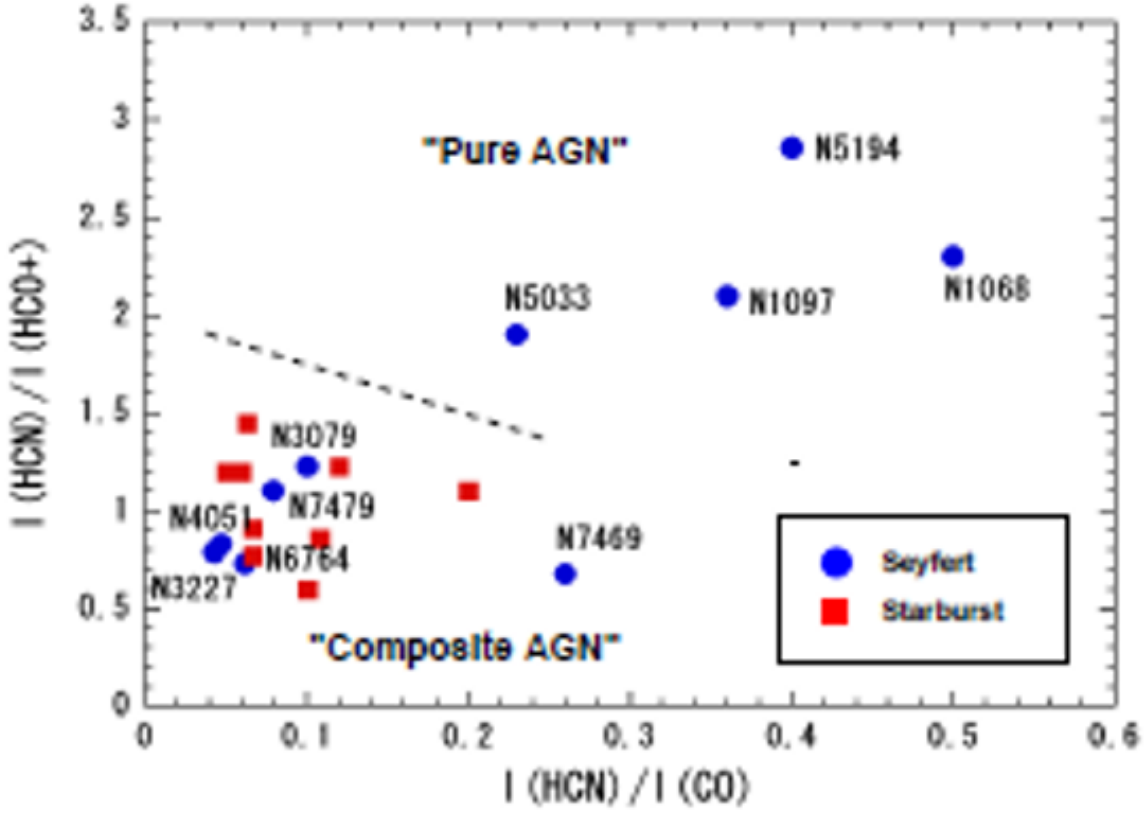


Figure 3.15: HCN/CO and HCN/$HCO^+$ integrated intensity ratios of the Seyfert and starburst galaxies (Kohno, 2005). These line ratios have been proposed as a diagnostic tool of the nuclear power source in active galaxies, be it starbursts (lower left) or AGN (upper right).

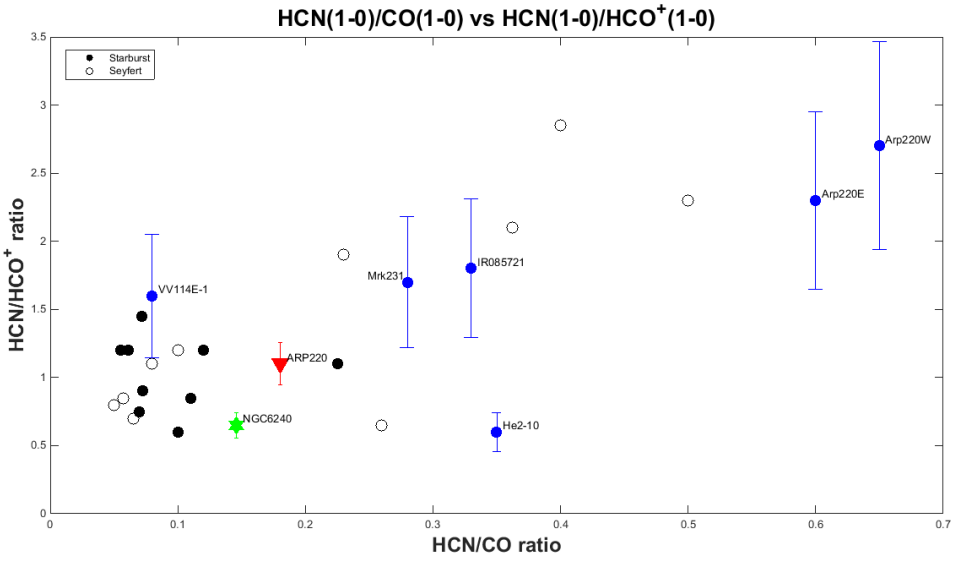


Figure 3.16: HCN/CO vs HCN/HCO: The error bars on data points collected from other sources are based on stated uncertainties in the papers (Imanishi & Nakanishi, 2006). The data points for our observations of Arp 220 and NGC 6240 are in red and green, respectively.

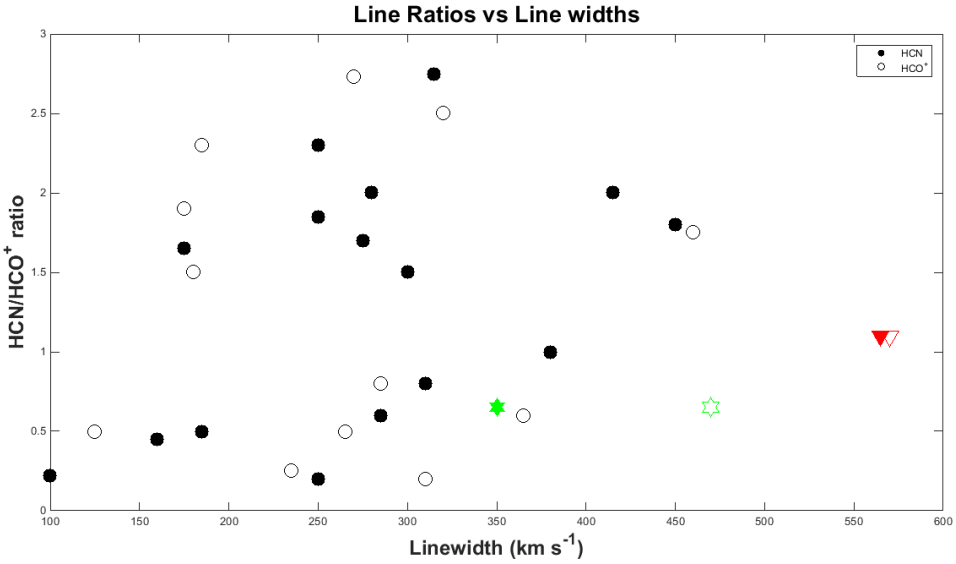


Figure 3.17: Line widths of HCN(1-0) and $HCO^+$(1-0) transitions plotted against HCN/$HCO^+$ brightness temperature ratios. This plot is a reproduction of a similar plot in Imanishi et al. (2007) with data points for our observations of Arp 220 and NGC 6240 overplotted for comparison. Arp 220 data points are in red and NGC 6240 in green. HCN line width data points are filled for all galaxies and $HCO^+$ ones are not filled. No obvious correlation exists between the line widths and the brightness temperature ratios.

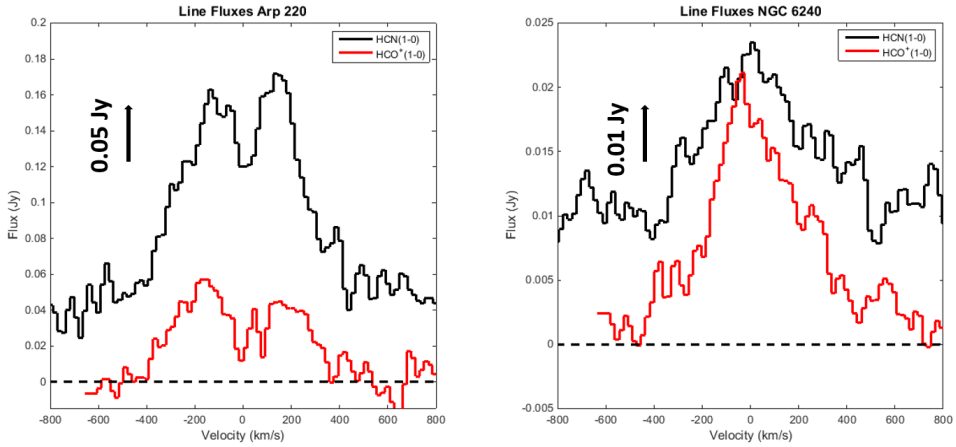


Figure 3.18: Overlaid HCN(1-0) and $HCO^+$(1-0) emission lines for both Arp 220 and NGC 6240. For Arp 220 has the two emission lines separated by 0.05 Jy for easier viewing. For NGC 6240 has the two emission lines separated by 0.01 Jy.

which envelopes the dense molecular gas where the gas surface densities are high since the turbulence broadens line widths.

Aalto et al. (1995) derived under LTE assumptions:

$$\tau_{10} \approx 3.911 \times 10^{-15} \frac{N(^{12}CO)}{T_{ex}\Delta V}(1 - e^{\frac{-5.5322}{T_{ex}}})$$

Here N($^{12}$CO) is the total column density of CO in cm$^{-2}$, $\Delta$V is the FWHM of the 1-0 transition line in km s$^{-1}$, $\tau_{10}$ is the line-center optical depth for 1-0 transition, and $T_{ex}$ is the temperature of CO.

Extreme starburts like Arp 220 will have more turbulence in enveloping gas. The gas will therefore have higher temperatures as the dissipation of the turbulence would heat up the gas (Güsten, 1989). As explained in Aalto et al. (1995), these two effects would decrease the CO(1-0) optical depths in the gas envelope. As a result, the strong UV emanating from the intense star formation regions in the galaxies would easily penetrate the gas envelopes and cause the destruction of "isotopic variants" of CO(1-0) (Aalto et al., 1995). Therefore, high values of $\Re_{1--0}$ would be expected in luminous mergers like Arp 220. Thus, as Aalto et al. (1995) suggested, large surface densities of gas expected in the cores of mergers do not always result in high CO(1-0) optical depths.

In summary, a high value of $\Re_{1--0}$ for Arp 220 does not necessarily imply a high abundance of CO and lower $^{13}$CO abundance. The low $^{13}$CO intensity could simply be the result of effects such as higher temperatures, turbulence, and the mixing of low metallicity gas. A high $\Re_{1--0}$ does not

imply a mean C/$^{13}$C abundance that is very different from molecular clouds found closer to us in the Milky Way galaxy ($\Re_{1--0} \backsimeq 4$ for a GMC, where $^{12}$C/$^{13}$C $\sim$60, Langer & Penzias (1993)).

Table 3.6: Intensity Ratios in C & $^{13}$C Molecules for Arp 220 and NGC 6240

| Galaxy | $\frac{\text{CO(1-0)}}{^{13}\text{CO(1-0)}}$ $\Re_{1--0}$ | $\frac{\text{HCN(1-0)}}{\text{H}^{13}\text{CN(1-0)}}$ |
|---|---|---|
| Arp 220 | 25.4 ± 0.3 | 2.6 ± 0.03 |
| NGC 6240 | ... | ... |

# Chapter 4

# CARMA B Configuration Imaging: 0.5 - 0.8″ Observations and Analysis

In this section, we present additional observations at a higher resolution (CARMA B configuration) than that which was achieved in the previous chapter (CARMA C Configuration). This is the first comprehensive high resolution interferometric measurements of the lower transition lines for these systems. We have measured velocity integrated fluxes and luminosities at 0.5 - 0.8 ″resolution. These observational parameters along with those for the earlier C Configuration are tabulated in Table 4.1.

## 4.1 Arp 220

### 4.1.1 CO(1-0)

The double peaked profile expected from the counter-rotating molecular gas disks observed in earlier studies (Scoville et al., 1997; Downes & Solomon, 1998) are again seen in B configuration 0.8 ″ observations (Fig. 4.3(b)). We see a stronger peak in CO(1-0) emission line at $\simeq$ -100 km s$^{-1}$ which is relative to the $V_{LSR}$ of ARP 220 of 5434 km s$^{-1}$. The second peak is at $\simeq$ of 180 km s$^{-1}$. As expected, these peaks correspond to the blueshifted nucleus and redshifted nucleus to the west and east respectively. In contrast to the 2 ″ resolution observations in the previous chapter (Fig. 4.3(a)), the peaks are similar in strengths and the dip between the peaks is deeper. The peak velocities are also slightly shifted.

The integrated line flux for our observations is 350 $\pm$ 35 Jy km s$^{-1}$, which agrees very well with the earlier lower resolution measurements. For other details, see Table 4.2 and 4.1.

### 4.1.2 HCN(1-0)

HCN(1-0) (Fig. 4.4(a)) shows a double peaked profile similar to CO(1-0). The peaks are of similar strengths. HCN(1-0) is a broad line, its width comparable to CO(1-0). The similarity in the strength of both the peaks suggests that physical conditions (densities, temperature, and opacities) in the two nuclei of Arp 220 are similar. The velocity widths of the two peaks are also somewhat broader than those seen in the lower resolution observations. The difference in their maximum fluxes is smaller than the uncertainty from the measurements. The blueshifted peak at $\simeq$ -180 km s$^{-1}$ has a peak flux of 0.105 Jy, whereas the redshifted peak at $\simeq$ 190 km s$^{-1}$ has a peak flux of 0.10 Jy. The integrated line flux for our HCN(1-0) transition is 49 $\pm$ 5 Jy km s$^{-1}$. These measurements are within the uncertainty limits of our previous lower resolution observations.

### 4.1.3 CS(2-1)

CS(2-1) is a weaker emission line (Fig. 4.4(b)) than C Configuration Arp 220 observations. A double peaked profile is again seen, indicating emission from each of the two nuclei. They are also broader than in our C Configuration observations. The blueshifted peak from the western nuclei at $\simeq$ -80 km s$^{-1}$ has a peak flux of 0.07 Jy, whereas the redshifted peak at $\simeq$ 50 km s$^{-1}$ has a peak flux of 0.072 Jy.

The integrated line flux for our CS(2-1) transition is 17 $\pm$ 0.2 Jy km s$^{-1}$. This is significantly higher than the C Configuration observations. The FWHM is measured at 375 km s$^{-1}$ in our observations for this transition.

### 4.1.4 HNC(1-0)

In the B configuration data, the HNC(1-0) line (Fig. 4.4(c)) is stronger line than HCN(1-0) line in Arp 220. This is similar to what was seen in the C configuration data. Again, a clearly defined double horned profile is seen, and unlike the HCN(1-0) the peaks are not of equal strength. Similar to the lower resolution observations, the blueshifted peak from the western nuclei has a peak flux higher than the redshifted peak. The blueshifted peak from the western nuclei at $\simeq$ -30 km s$^{-1}$ has a peak flux of 0.13 Jy, whereas the redshifted peak at $\simeq$ 175 km s$^{-1}$ has a peak flux of 0.1 Jy.

The profile of the HNC(1-0) transition in these observations is similar to the lower resolution data and the single dish spectra (Greve et al., 2009; Aalto et al., 2002). The integrated line flux for our HNC(1-0) transition is 58 $\pm$ 6 Jy km s$^{-1}$. The FWHM is measured at 425 km s$^{-1}$ in the B configuration data for this transition, i.e. is narrower than HCN(1-0) line.

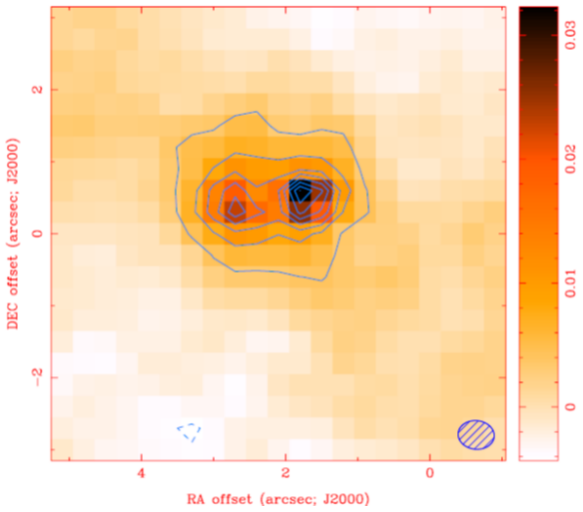


Figure 4.1: Arp 220 Integrated Line Intensity images for CO(1-0) emission. Contours are at $2\sigma$ spacings starting at $4\sigma$. The beam size is shown in the lower right corner

### 4.1.5 $HCO^+$(1-0)

The blueshifted peak of $HCO^+$(1-0) (Fig. 4.4(d)) has a peak flux higher than the redshifted peak from the eastern nuclei. The spectral peaks are more distinct for the other emission lines. The blueshifted peak from the western nuclei at $\simeq$ -125 km $s^{-1}$ has a peak flux of 0.065 Jy, whereas the redshifted peak at $\simeq$ 175 km $s^{-1}$ has a peak flux of 0.05 Jy.

The integrated line flux for $HCO^+$(1-0) emission is 36 $\pm$ 4 Jy km $s^{-1}$. This measurement agrees with our lower resolution observations. The FWHM is measured at 450 km $s^{-1}$ in our observations for this transition. The higher resolution observations are less broad than our 2 $''$ observations. $HCO^+$(1-0) is also very broad, indicating a lot of turbulence in the molecular gas.

The disagreement in our measurements of $HCO^+$(1-0) integrated line flux with previous single dish and interferometric observations has been indicated in the precious chapter. With these higher resolution measurements, we have recovered similar flux measurements which confirm our previous observations.

### 4.1.6 Isotopomer Emission Line

Along with the afore mentioned emission lines, we were also able to configure the correlator at CARMA to observe the isotopomer lines $H^{13}CN$(1-0) and $^{13}CS$(2-1). While we were able to detect $H^{13}CN$(1-0) at more than $10\sigma$ level, $^{13}CS$(2-1) was not detected. The integrated line flux of $H^{13}CN$(1-0) was measured at 17 $\pm$ 2 Jy km $s^{-1}$ and the FWHM was 380 km $s^{-1}$.

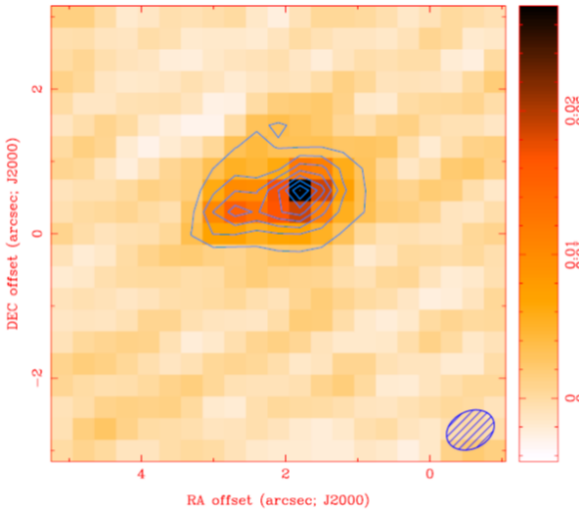


Figure 4.2: Arp 220 Integrated Line Intensity images for HCN(1-0) emission. Contours are at $2\sigma$ spacings starting at $4\sigma$. The beam size is shown in the lower right corner

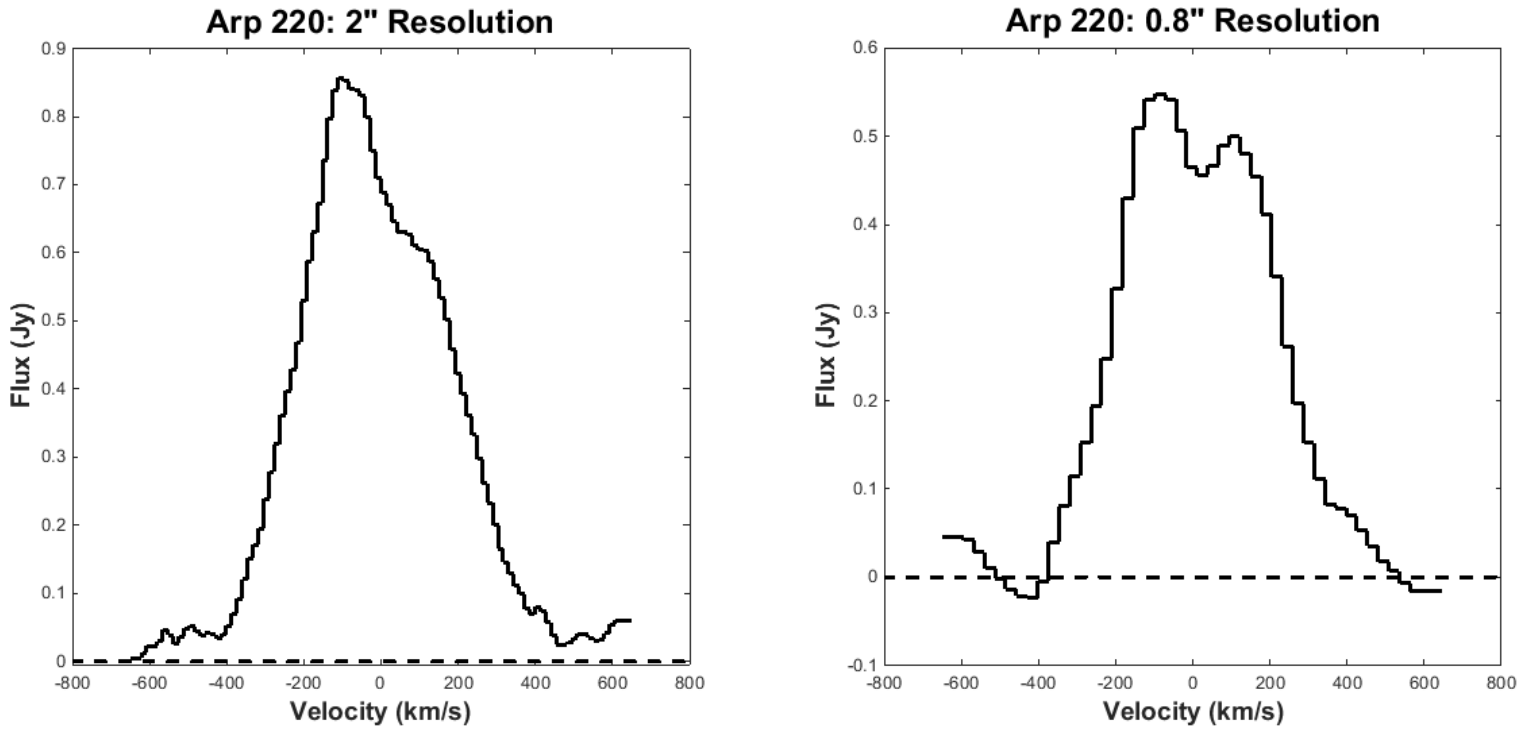


Figure 4.3: Molecular CO(1-0) spectra observed in Arp 220 at both resolutions. The velocity scale for transitions is same as the transitions in Fig. 4.4 and centered at the galaxy redshift. The velocity scales cover the same range for both resolutions. The flux scale is scaled to fill the available space.

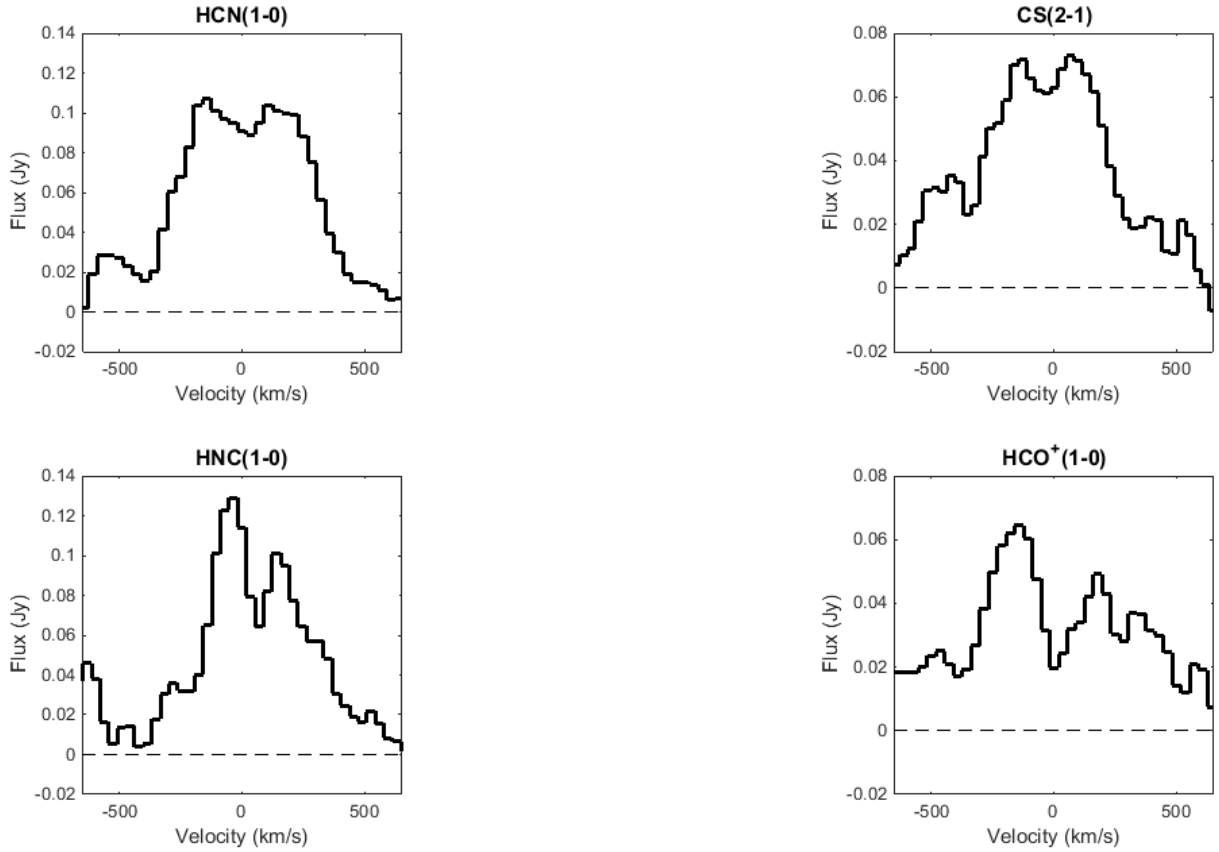


Figure 4.4: Molecular line spectra observed in Arp 220. The velocity scale for all transitions is the same and centered at the galaxy redshift. HCN(1-0) and HNC(1-0) transition spectra (panels (a) and (c)) are on the same flux scale. The CS(2-1) and $HCO^+$(1-0) spectra (panels (b) and (d)) internal scales have been stretched to show spectra features clearly.

Table 4.1: Molecular Transition Lines Detected: Arp 220 and NGC 6240

| Line | Arp 220 | | | | NGC 6240 | | | |
|---|---|---|---|---|---|---|---|---|
| | FWHM | $S_\nu \Delta v$ | $L'^c$ | Resolution | FWHM | $S_\nu \Delta v$ | $L'^c$ | Resolution |
| | km s$^{-1}$ | Jy km s$^{-1}$ | x10$^9$ K km s$^{-1}$ pc$^2$ | | km s$^{-1}$ | Jy km s$^{-1}$ | x10$^9$ K km s$^{-1}$ pc$^2$ | |
| CO(1-0) | 500 | 385 ± 40 | 6.1 ± 0.64 | 2″ | 400 | 304 ± 30 | 8.9 ± 0.88 | 2″ |
| | 450 | 350 ± 35 | 5.2 ± 0.52 | 0.8″ | ... | ... | ... | ... |
| HCN(1-0) | 565 | 42 ± 4 | 1.1 ± 0.11 | 2″ | 350 | 26 ± 2.6 | 1.3 ± 0.13 | 2″ |
| | 550 | 49 ± 5 | 1.3 ± 0.13 | 0.8″ | 325 | 24 ± 2.4 | 1.2 ± 0.12 | 0.8″ |
| CS(2-1) | 345 | 11 ± 0.1 | 0.24 ± 0.02 | 2″ | 175 | 3 ± 0.6 | 0.12 ± 0.02 | 2″ |
| | 375 | 17 ± 2 | 0.38 ± 0.04 | 0.8″ | 200 | 12 ± 1 | 0.05 ± 0.01 | 0.8″ |
| HNC(1-0) | 400 | 53 ± 5 | 1.4 ± 0.13 | 2″ | 275 | 19 ± 4 | 0.89 ± 0.2 | 2″ |
| | 425 | 58 ± 6 | 1.5 ± 0.15 | 0.8″ | 275 | 18 ± 6 | 0.85 ± 0.3 | 0.8″ |
| $HCO^+$(1-0) | 570 | 37 ± 4 | 1.0 ± 0.11 | 2″ | 470 | 40 ± 4 | 2.0 ± 0.19 | 2″ |
| | 450 | 36 ± 4 | 0.96 ± 0.1 | 0.8″ | 470 | 48 ± 5 | 2.3 ± 0.2 | 0.8″ |
| $^{13}$CO(1-0) | 380 | 14 ± 2 | 0.24 ± 0.04 | 2″ | ... | ... | ... | ... |
| | 300 | 11 ± 1 | 0.19 ± 0.02 | 0.8″ | ... | ... | ... | ... |
| H$^{13}$CN(1-0) | 400 | 15 ± 2 | 0.43 ± 0.06 | 2″ | ... | ... | ... | ... |
| | 380 | 17 ± 2 | 0.48 ± 0.05 | 0.8″ | ... | 7 ± 2 | 0.37 ± 0.1 | 0.8″ |
| $^{13}$CS(2-1) | ... | ... | ... | ... | ... | ... | ... | ... |

## 4.2 NGC 6240

### 4.2.1 HCN(1-0)

HCN(1-0) spectra (Fig. 4.5(a)) has a single peaked profile, consistent with previous observations. However, the profile is not as sharply peaked as CO(1-0). It is a broad line, its width comparable to CO(1-0) in NGC 6240. The FWHM is measured at 325 km $s^{-1}$ in our observations for this transition. The line peaks at 0 km $s^{-1}$ relative to the $V_{LSR}$ of NGC 6240 of 7359 km $s^{-1}$.

The integrated line flux for our HCN(1-0) transition is 24 ± 2.4 Jy km $s^{-1}$. These measurements agree with our previous observations.

### 4.2.2 CS(2-1)

The CS(2-1) emission (Fig. 4.5(b)) is much weaker line in NGC 6240 compared to Arp 220. The 0.8″ observations of CS(2-1) is a more significant detection ($10\sigma$) than the previous lower resolution observations. The profile is Gaussian like HCN(1-0). The line has not been detected by other observations. The interferometric stability along with the long observation times, in contrast to the earlier single dish observations at lower sensitivity, made this detection possible. The integrated flux measured the CS(2-1) is 12 ± 0.12 Jy km $s^{-1}$. The FWHM is 220 km $s^{-1}$.

### 4.2.3 HNC(1-0)

HNC(1-0) (Fig. 4.5(c)) is another weak line in NGC 6240. The detection is weak at about at $3\sigma$ level. We see more of a profile and stronger emission than the previous single dish measurement (Greve et al., 2009). The integrated flux density is 18 ± 6 Jy km $s^{-1}$.

### 4.2.4 $HCO^+$(1-0)

As in the case of Arp 220, $HCO^+$(1-0) (Fig. 4.5(d)) is a very strong emission line in NGC 6240. This was surprising considering that many of the other well studied emission lines were so much weaker than this emission line. Its profile is very similar to the other strong emission lines in NGC 6240 like HCN(1-0) and the lower resolution CO(1-0). However, its peak is not centered at 0 km $s^{-1}$, as is the case with the other two, but at -50 km $s^{-1}$. The peak of this emission line 0.037 Jy.

The integrated line flux for the $HCO^+$(1-0) transition is 48 ± 4 Jy km $s^{-1}$, which agrees with 2″ resolution measurements within the uncertainties. This is the only emission line where integrated flux density of the line is comparable for Arp 220 and NGC 6240. The FWHM is measured at 470 km $s^{-1}$ in our observations. $HCO^+$(1-0) is also a broad line; its FWHM is similar to that of the CO(1-0) line, indicating perhaps similar spatial extents and gas dynamics.

### 4.2.5 Isotopomer Emission Line

The correlator was configured to also simultaneously observe the isotopomer lines for many of emission lines we are observing here such as $H^{13}CN$(1-0) and $^{13}CS$(2-1). $^{13}CS$(2-1) was not detected. $H^{13}CN$(1-0) is a weak detection ($4\sigma$). The integrated line flux is $7 \pm 2$ Jy km $s^{-1}$.

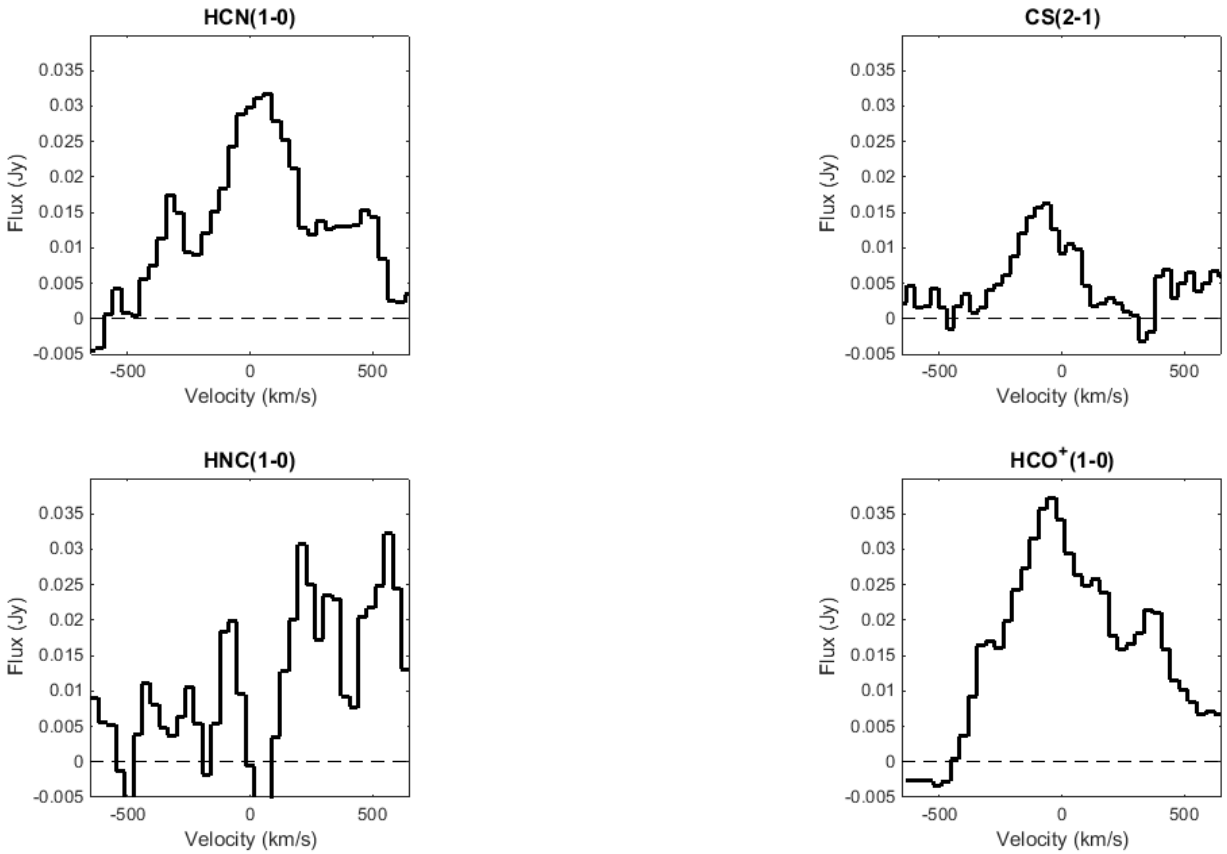


Figure 4.5: Molecular line spectra observed in NGC 6240. The velocity scale for the four transitions is same and centered at the galaxy redshift. HCN(1-0), CS(2-1), HNC(1-0), and $HCO^+$(1-0) transition spectra (panels (a)-(d)) are on the same flux scale.

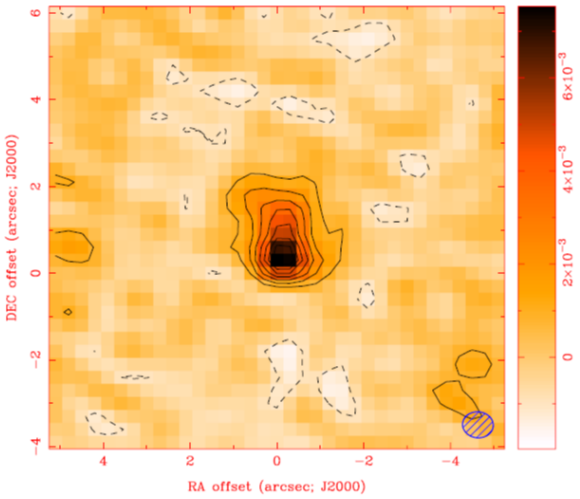


Figure 4.6: NGC 6240 Integrated Line Intensity images for HCN(1-0) emission. Contours are at $2\sigma$ spacings starting at $4\sigma$. The beam size is shown in the lower right corner

Table 4.2: Observational Parameters

| Parameter | CO(1-0) | HCN(1-0) | CS(2-1) | HNC(1-0) | $HCO^+$(1-0) | $^{13}$CO(1-0) | $H^{13}CN$(1-0) | $^{13}$CS(2-1) |
|---|---|---|---|---|---|---|---|---|
| Arp 220 | | | | | | | | |
| $\nu_{obs}$ (GHz) | 113.219 | 87.05 | 96.23 | 89.05 | 87.60 | 108.239 | 84.80 | 90.84 |
| $t_{int}$(hrs) | 30.4 | 23.8 | 23.8 | 23.8 | 23.8 | 30.4 | 23.8 | 23.8 |
| HPBW($''$) | 0.5 x 0.4 | 0.66 x 0.53 | 0.61 x 0.47 | 0.66 x 0.54 | 0.65 x 0.51 | 0.53 x 0.41 | 0.68 x 0.53 | 0.64 x 0.49 |
| NGC 6240 | | | | | | | | |
| $\nu_{obs}$ (GHz) | 112.517 | 86.51 | 95.64 | 88.49 | 87.06 | 107.568 | 84.27 | 90.28 |
| $t_{int}$(hrs) | 0 | 25 | 25 | 25 | 25 | 0 | 25 | 25 |
| HPBW($''$) | ... | 0.7 x 0.6 | 0.64 x 0.52 | 0.79 x 0.54 | 0.69 x 0.59 | ... | 0.73 x 0.59 | 0.68 x 0.55 |

## 4.3 Analysis & Discussion

### 4.3.1 High Density Molecular Gas traced in HCN, CS, HNC, and $HCO^+$

#### 4.3.1.1 Two Level Excitation with Photon Trapping

The methodology followed in Section 3.3.1.1 to derive an estimate of molecular hydrogen density, $n_{H2}$, and the optical depth, $\tau$, is recreated here for the 0.5 - 0.8$''$ observations of the two ULIRGs. We used the transitions HCN(1-0), CS(2-1), HNC(1-0) and $HCO^+$(1-0). As each of these molecules have a unique set of properties they wil therefore give us insight into the density and temperature of the molecular gas in these galaxies.

The values used for the equations derived in section 3.3.1.1 and used in the following sections

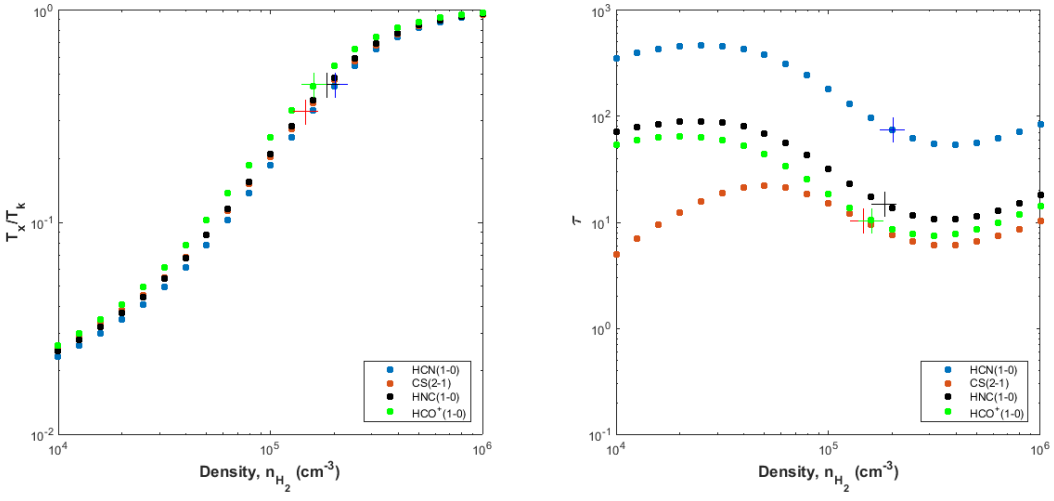


Figure 4.7: Arp 220: On the left, the ratio of the level excitation temperature to the gas kinetic temperature ($T_x/T_k$) on the abscissa and the density of HCN(1-0), CS(2-1), HNC(1-0), and HCO$^+$(1-0) lines, which have been calculated from equations in Section 3.3.1.1. On the right, the optical depths of each of the lines are shown.

are collated in Table 4.3 for Arp 220 and NGC 6240. All the variable names used are same as those described in section 3.3.1.1. The assumed abundances are the same as in Chapter 3.

Table 4.3: Constants used for Two Level Excitation with Photon Trapping for Arp 220 and NGC 6240

| | | | | | Arp 220 | | NGC 6240 | |
|---|---|---|---|---|---|---|---|---|
| Line | B | $A_{ul}$ | Abundance, X | $\langle\sigma v\rangle_{ul}$ | $T_b$ | dv/dr | $T_b$ | dv/dr |
| | GHz | $s^{-1}$ | Relative to $H_2$ | $s^{-1}$ | K | $s^{-1}$ | K | $s^{-1}$ |
| HCN(1-0) | 44.32 | 2.4 x $10^{-5}$ | 2 x $10^{-8}$ | 1.2 x $10^{-11}$ $(\frac{T_k}{50})^{-0.468}$ | 22 | 1.3 x $10^{-13}$ | 3.3 | 3 x $10^{-14}$ |
| CS(2-1) | 24.50 | 1.7 x $10^{-5}$ | 5 x $10^{-9}$ | 4.9 x $10^{-11}$ $(\frac{T_k}{50})^{-0.130}$ | 14 | 1 x $10^{-13}$ | 2.3 | 1.7 x $10^{-14}$ |
| HNC(1-0) | 45.33 | 2.7 x $10^{-5}$ | 4 x $10^{-9}$ | 7.6 x $10^{-11}$ $(\frac{T_k}{50})^{-0.196}$ | 22.5 | 1 x $10^{-13}$ | 7.5 | 2.3 x $10^{-14}$ |
| HCO$^+$(1-0) | 44.59 | 4.3 x $10^{-5}$ | 4 x $10^{-8}$ | 2x $10^{-9}$ $(\frac{T_k}{50})^{-0.152}$ | 17 | 1.1 x $10^{-13}$ | 3.3 | 4 x $10^{-14}$ |

#### 4.3.1.2 HCN(1-0) Excitation in Arp 220 and NGC 6240

The above described methodology was used to estimate the gas density for each of the observed transitions in Arp 220 and NGC 6240. As earlier, in the case of Arp 220, we estimated the nuclei to be ∼130 pc in diameter and in the case of NGC 6240, we estimated it to be ∼380 pc. The FWHM of each transition in the respective galaxies was then used to calculate dv/dr. The number is listed

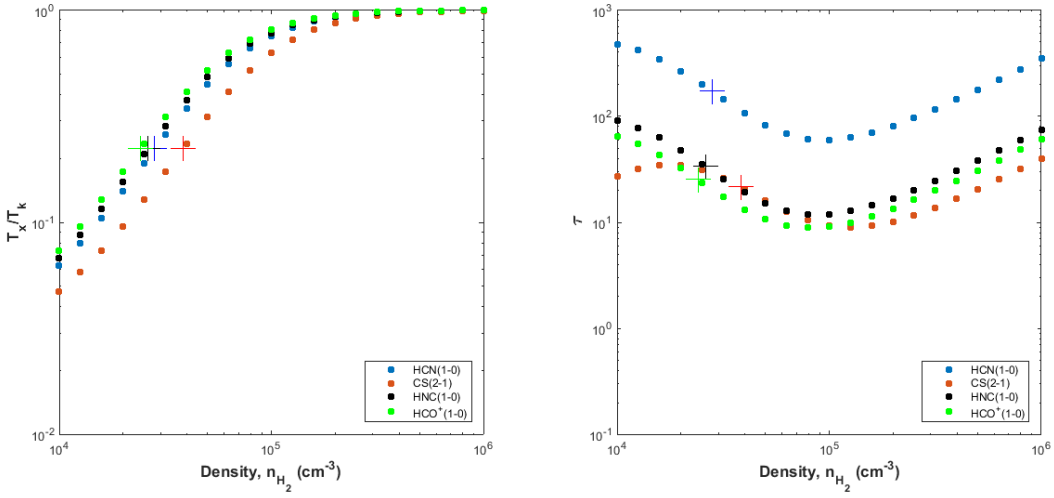


Figure 4.8: NGC 6240: On the left, the ratio of the level excitation temperature to the gas kinetic temperature ($T_x/T_k$) on the abscissa and the density of HCN(1-0), CS(2-1), HNC(1-0) and $HCO^+$(1-0) lines which have been calculated from equations in Section 3.3.1.1. On the right, the optical depths of each of the lines are shown.

in Table 4.3 for all transitions. We adopted a kinetic temperature of ∼45 K. This is again from the dust temperature measured in IR from Sanders et al. (1991) for Arp 220 and NGC 6240. For HCN(1-0), the peak brightness temperature is ∼20 K in Arp 220 and ∼ 3 K in NGC 6240. The line is expected to be optically thick, and therefore this brightness temperature indicates an excitation temperature, $T_x$, of the order of 20-40 K for Arp 220 and of the order of 10 K for NGC 6240. Thus, the gas density would be measured at $T_x/T_k \backsimeq 0.44$ in Arp 220 and 0.22 in NGC 6240.

The values used for variables in the equations in section 3.3.1.1 such as B, $T_0$, $A_{1-0}$, etc., and hence to create the Fig. 4.7 and Fig. 4.8 are also provided in Table 4.3. The collision rate coefficients are those that were used in the previous chapter. The summed rate coefficient used for each of the transitions is also provided in Table 4.3. We assumed the same abundance of HCN relative to molecular hydrogen, $H_2$, as in the previous chapter.

The ratio of the level excitation temperature to the gas kinetic temperature ($T_x/T_k$) as a function of density $n_{H2}$ is shown in Fig. 4.7 and Fig. 4.8 with blue dots.

#### 4.3.1.3 CS(2-1) Excitation in Arp 220 and NGC 6240

For CS(2-1), the peak brightness temperature ∼ 14 K for Arp 220 and 2.3 K for NGC 6240. Thus, $T_x/T_k \backsimeq 0.3$ in Arp 220 and 0.2 in NGC 6240. Again, the various values of B, $T_0$, $A_{1-0}$, etc,. are

detailed in Table 4.3. The dv/dr has been calculated using the FWHM values measured from our observation (Table 4.1). The ratio of the level excitation temperature to the gas kinetic temperature ($T_x/T_k$) as a function of density $n_{H2}$ is shown in Fig. 4.7 and Fig. 4.8 with red dots.

#### 4.3.1.4 HNC(1-0) Excitation in Arp 220 and NGC 6240

As in the previous chapter, for HNC(1-0), Graninger et al. (2014) postulate $X_{HNC} \sim X_{HCN}$. Therefore, we assume $X_{HNC} \sim 4 \times 10^{-9}$ for our calculations. As in the previous chapter, we have adjusted the abundance of HNC. The peak brightness temperature $\sim$ 22 K for Arp 220 and 7.5 K for NGC 6240. Thus, $T_x/T_k \backsimeq 0.4$ in Arp 220 and 0.2 in NGC 6240. The ratio of the level excitation temperature to the gas kinetic temperature ($T_x/T_k$) as a function of density, $n_{H2}$, is shown in Fig. 4.7 and Fig. 4.8 with black dots.

#### 4.3.1.5 $HCO^+$(1-0) Excitation in Arp 220 and NGC 6240

For $HCO^+$(1-0), the peak brightness temperature $\sim$ 17 K for Arp 220 and 3.3 K for NGC 6240. Thus, $T_x/T_k \backsimeq 0.4$ in Arp 220 and 0.2 in NGC 6240. We assumed the abundance of $HCO^+$ relative to molecular hydrogen, $H_2$ to be $X_{HCO^+} \sim 4 \times 10^{-9}$. As in the previous chapter, we have adjusted the abundance of $HCO^+$. The ratio of the level excitation temperature to the gas kinetic temperature ($T_x/T_k$) as a function of density $n_{H2}$ is shown in Fig. 4.7 and Fig. 4.8 with green dots.

#### 4.3.1.6 Densities Required for the Observed Emission

The left subplots in Fig. 4.7 and Fig. 4.8 show the ratio $T_x/T_k$ calculated for all the transitions in Arp 220 and NGC 6240.'+' on the plots shows the density corresponding to the observed values of $T_x/T_k$ measured for each transition, which have been mentioned in the previous sections. For the assumed abundances in Arp 220, the required densities, $n_{H2}$ are 2 x $10^5$ $cm^{-3}$ for HCN, 2 x $10^5$ $cm^{-3}$ for CS, 2 x $10^5$ $cm^{-3}$ for HNC, and 1.6x $10^5$ $cm^{-3}$ for $HCO^+$. For the assumed abundances in NGC 6240, the required densities, $n_{H2}$, are 3 x $10^4$ $cm^{-3}$ for HCN, 4 x $10^4$ $cm^{-3}$ for CS, 3 x $10^4$ $cm^{-3}$ for HNC, and 2 x $10^4$ $cm^{-3}$ for $HCO^+$.

The rightside subplots in Fig. 4.7 and Fig. 4.8 show the line optical depth for each of the transitions as a function of density. The optical depths for the above mentioned densities are marked with '+' in the subplots. In the case of Arp 220, the optical depth, $\tau$, is 70 for HCN, 10 for CS, 15 for HNC, and 10 for $HCO^+$. For NGC 6240, the optical depths, $\tau$, are 170 for HCN, 20 for CS, 35 for HNC, and 35 for $HCO^+$. Thus, these lines are optically thick, as assumed earlier for both galaxies. The optical depth is over 100 again for HCN in NGC 6240. Therefore, our earlier assumption that the gas is optically thick is valid.

In Arp 220, HCN, CS, HNC, and $HCO^+$ measurements and calculations produce molecular gas densities of the same order of magnitude for the assumed abundances. The same adjustments have

been made for both HNC and $HCO^+$ as in the previous chapter. This was so that the $n_{H2}$ calculated from various molecules would agree. The adjusted abundances are not similar to those measured in galactic sources or in the LMC (Graninger et al., 2014; Acharyya & Herbst, 2015). The disparity in HNC abundances is perhaps a result of destruction of the molecule at high temperatures, for example in regions of star formation. $HCO^+$ abundance can be affected by recombination in very dense gas. Therefore, in regions of very high density, the regions we are mapping, $HCO^+$ abundance would be low. The measurements from our $2''$ resolution observations agree with the $0.8''$ resolution observations. $HCO^+$ has a higher peak brightness temperature in the $0.8''$ resolution observations. This might be caused by a dense pocket of $HCO^+$ gas in Arp 220 which might be more resolved at higher resolutions.

In the case of NGC 6240, HCN, CS, HNC, and $HCO^+$ measurements and calculations produce similar molecular gas densities for the adjusted abundances. We assumed the abundances for NGC 6240 calculations as in the Arp 220 calculations. Again, the disparity in the abundances of these ULIRGs and galactic sources is perhaps the chemical and physical processes at play in the systems. The $n_{H2}$ calculations done earlier for $2''$ resolution observations agree with the $0.8''$ resolution observations in this section.

In chapter 5, we will discuss a fully correct multi-level equiibrium analysis to calculate the molecular hydrogen densities in these galaxies using the Large Velocity Gradient or Sobolev formalism to treat the radiative transfer for molecular excitation.

### 4.3.2 HCN and HNC line ratios: XDR vs PDR regions

#### 4.3.2.1 ARP 220 and NGC 6240: PDR or XDR?

In the previous chapter (section 3.3.2) we discussed the use of HCN and HNC line ratios to gain insight into the environment of these ULIRGs. The existence of PDRs or XDRs can be inferred from HCN and HNC line ratios using the models that were discussed extensively in the previous chapter. As mentioned before, Arp 220 does not have a confirmed AGN nucleus or nuclei. However, observations done by Clements et al. (2002) and McDowell et al. (2003) using Chandra X-Ray Observatory do not definitively confirm the presence of an AGN. They observed a point source with a hard X-Ray spectrum that lies within the western radio nucleus of Arp 220. They also observed a fainter source in the eastern nucleus of the ULIRG. They detected an extended X-ray emission in the energy range 2-10 keV with a luminosity of $1.2 \times 10^{41}$ erg $s^{-1}$ and suggested that one possibility to explain this luminosity is the existence of an AGN shrouded by gas with column densities $> 5 \times 10^{24}$ $cm^{-2}$.

In the case of NGC 6240, Komossa et al. (2003) observed using the ACIS-S detector aboard the Chandra X-Ray Observatory and detected two hard X-ray nuclei coinciding with the optical-IR

nuclei. They also detected strong neutral FeK$\alpha$ lines in both the nuclei of NGC 6240 (Komossa et al., 2003). Extended X-Ray continuum emission was also detected for both nuclei.

HCN and HNC line ratios might give us insight into the engines irradiating the molecular gas and hence affecting the chemical and physical properties. As discussed in section 3.3.2, at higher temperatures HNC tends to be selectively destroyed in favor of HCN as long as the medium is not highly ionized. Therefore, HCN/HNC is roughly unity in PDR sources, but lower than unity in XDR sources. The HCN/HNC abundance ratio ratio is expected to be around 1.1, if the standard neutral production paths are followed (Goldsmith et al., 1981). In a highly ionized medium, high HCN/HNC ratios would be unlikely since $HCNH^+$ can form HCN and HNC with equal probability (Aalto et al., 2002; Wang et al., 2004). The passage of shocks may also selectively destroy HNC and could significantly increase the steady-state HCN/HNC abundance ratio (Schilke et al., 1992). Both HCN and HNC may be pumped by an intense mid-IR radiation field, boosting the emission from low density regions where the lines would not normally be collisionally excited. The interaction with the IR radiation field is stronger for HNC than for HCN, thus increasing the probability for IR pumping in extreme galaxies and hence decreasing HCN/HNC.

Table 4.4 displays the HCN/HNC line intensity ratios for the 1–0 transition for Arp 220 and NGC 6240 from our observations along with the ratios from other sources such as Seyferts, liners and GMCs. The HCN and HNC spectra are shown in Fig. 4.9 on the same plot for each of the ULIRGs for comparison of line strengths.

While the HCN/HNC ratio is less than unity for Arp 220, that is not the case for NGC 6240. Even with allowing for the uncertainty in the measurements, the ratio for Arp 220 is less than unity. As discussed before in this section, a ratio less than unity in the case of Arp 220 indicates the presence of a strongly irradiated XDR and very likely an AGN in the nuclei of the Arp 220. In an earlier section, the profiles and relative strengths of the peaks for all molecular lines were discussed. Since HNC is a stronger line in both the nuclei as compared to HCN, there is a strong indication that both nuclei likely host an AGN irradiating the molecular gas. This, in addition to the Clements et al. (2002) Chandra observations, can be used to make an argument for the presence of AGN in the nuclei of Arp 220.

In comparison, NGC 6240, which is known to have two AGN detected by X-Ray observations (Komossa et al., 2003), displays a line ratio higher than unity. Such a ratio is expected from molecular gas with PDR conditions. That is not to say that a XDR does not exist within the galaxy. It only indicates that the molecular gas clouds we are observing have been mostly been irradiated by radiation originating from star forming regions. In NGC 6240, the molecular gas is observed between the two nuclei. As a result, the molecular gas will be less irradiated by the hard X-Rays from the AGN. The ratio observed in NGC 6240 is very similar to other known star forming galaxies as shown in Table 4.4. NGC 6240 ratios are similar to other Seyfert, LINER, and LIRG

galaxies which indicates chemistry similar to these galaxies – probably a mix of starburst and AGN conditions but with the starburst dominant.

In summary, the diminished HCN/HNC ratio in Arp 220 likely indicates the presence of XDR conditions due to an AGN.

Table 4.4: HCN and HNC Line Ratios for Arp 220 and NGC 6240

| Galaxy | $\frac{\text{HCN(1–0)}}{\text{HNC(1–0)}}$ | Reference |
|---|---|---|
| NGC 3079 | 2.15 ± 0.67 | Pérez-Beaupuits et al. (2007) |
| NGC 1068 | 2.01 ± 0.65 | Pérez-Beaupuits et al. (2007) |
| NGC 2623 | 1.4 | Aalto et al. (2002) |
| NGC 1365 | 1.35 ± 0.37 | Pérez-Beaupuits et al. (2007) |
| NGC 7469 | 1.50 ± 0.57 | Pérez-Beaupuits et al. (2007) |
| L1489 | 0.83 ± 0.17 | Hirota et al. (1998) |
| L1521B | 0.5 ± 0.12 | Hirota et al. (1998) |
| ARP 220 | 0.79 ± 0.1 | 2″ CARMA |
| ARP 220 | 0.84 ± 0.1 | 0.8″ CARMA |
| NGC 6240 | 1.39 ± 0.2 | 2″ CARMA |
| NGC 6240 | 1.33 ± 0.2 | 0.8″ CARMA |

### 4.3.3 HCN and $HCO^+$ Ratios

A goal of this thesis has been to study the dense molecular gas present in the ULIRGs Arp 220 and NGC 6240. ULIRGs are havens for both starbursts and AGNs. The presence of both AGNs and starbursts can't always be untangled. In the last section, we used HCN and HNC line ratios as a means to probe the physical and chemical properties of the molecular gas. To further our understanding of the conditions prevalent in the galaxies, we have the capacity with this study to use other dense molecular gas tracers to probe the density and temperature of the dense core regions of the galaxies.

In this section, we use $HCO^+$ as a diagnostic to probe the physical conditions and chemistry of our targets. HCN and HNC ratios already indicate the presence of XDRs, perhaps generated by AGN cores in Arp 220. Similar studies have been proposed to use $HCO^+$ together with HCN and CO lines to separate "Pure AGN" from "Composite AGN", i.e. galaxies with starbursts and AGN components (Kohno, 2005).

#### 4.3.3.1 Interpertation and Analysis of the Brightness Temperature Ratios

As explained in section 3.3.3, Kohno et al. (2001); Kohno (2005) found empirically that galaxies that were dominated by strong AGNs displayed a higher HCN/$HCO^+$ and HCN/CO ratio than galaxies that were were dominated by starbursts. Thus, AGN dominated galaxies were expected to be in the

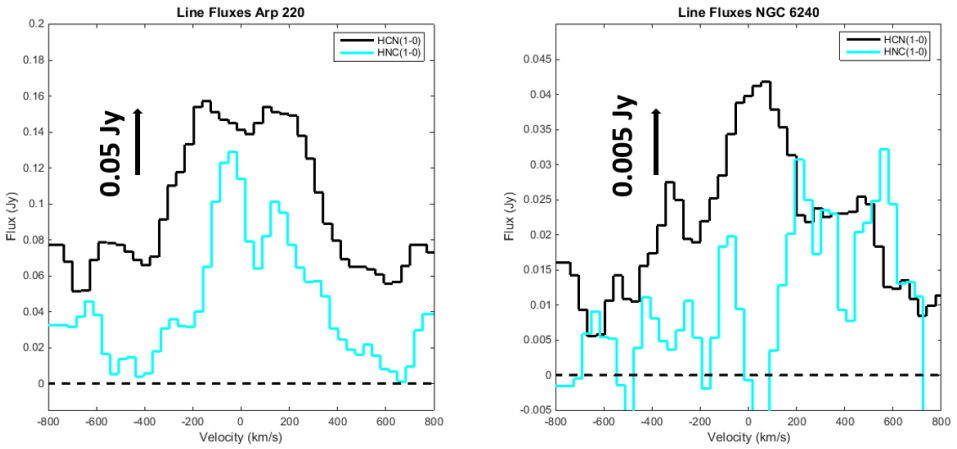


Figure 4.9: Overlaid HCN(1-0) and HNC(1-0) emission lines for Arp 220 and NGC 6240, respectively. Arp 220 has the two emission lines separated by 0.05 Jy for easier viewing. NGC 6240 has the two emission lines separated by 0.005 Jy for easier viewing.

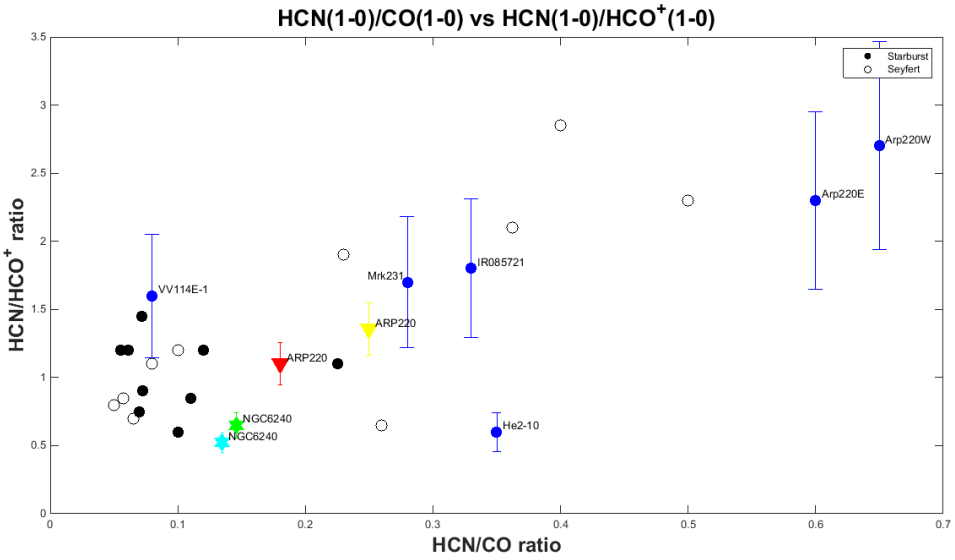


Figure 4.10: HCN/CO vs HCN/HCO: Collated data from various sources. The error bars on data points collected from other sources are based on mentioned uncertainties in the papers (Imanishi & Nakanishi, 2006). The data points for our 2″ observations of Arp 220 and NGC 6240 are in red and green respectively. The 0.8″ observations of Arp 220 and NGC 6240 are in yellow and cyan, respectively. The points are labelled on the plot.

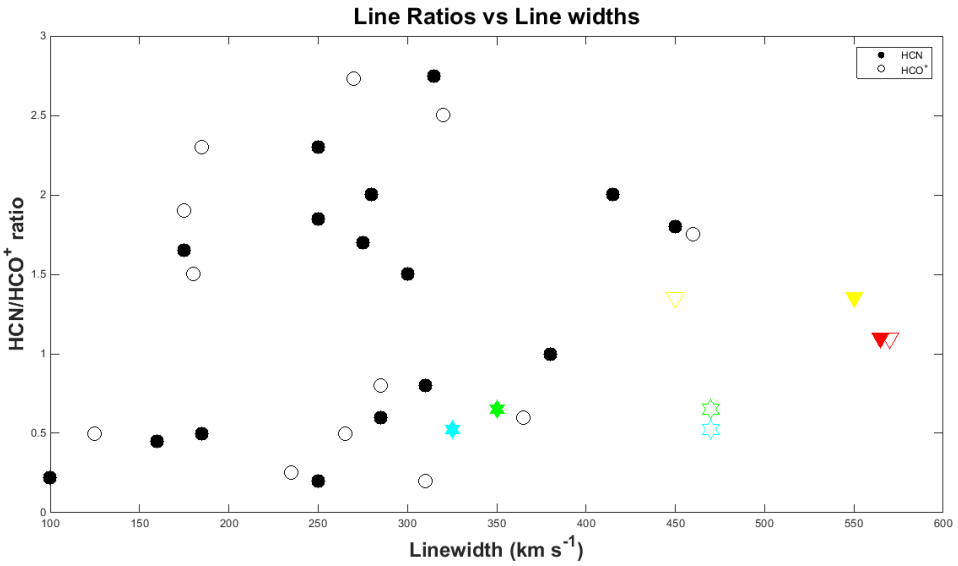


Figure 4.11: Line widths of HCN(1-0) and $HCO^+$(1-0) transitions plotted against HCN/$HCO^+$ brightness temperature ratios. This plot is a reproduction of a similar plot in Imanishi et al. (2007) with data points for our observations of Arp 220 and NGC 6240 overplotted for comparison. For the 2″ observations, Arp 220 data points are in red and NGC 6240 in green. For the 0.8″ observations, Arp 220 data points are in yellow and NGC 6240 in cyan. HCN line width data points are filled for all galaxies and $HCO^+$ ones are not filled.

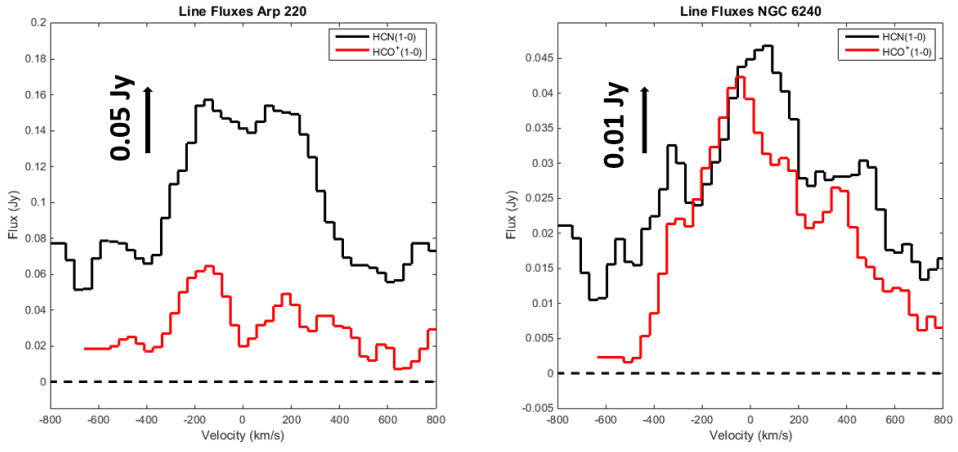


Figure 4.12: Overlaid HCN(1-0) and $HCO^+$(1-0) emission lines for both Arp 220 and NGC 6240. Arp 220 has the two emission lines separated by 0.05 Jy for easier viewing. NGC 6240 has the two emission lines separated by 0.01 Jy. This plot helps better visualize the flux ratios of the lines.

upper right section of the Fig. 3.15 and Fig. 4.10, whereas the starbursts would reside in the lower left.

The HCN abundance will be enhanced in dense molecular clouds because of the disparity in the dipole moments of HCN and CO. Many studies have shown that there is an enhancement in the HCN/CO brightness temperature ratios when galaxies contained a larger fraction of high density molecular gas (e.g. Solomon et al. (1992b); Curran (2000)). Sanders & Mirabel (1996) also show that ULIRGs displayed a higher fraction of dense molecular gas than less IR luminous galaxies. Therefore, high HCN/CO ratios would be expected from ULIRGs, despite the presence of XDRs irradiated by central black hole engines. Thus, the HCN/CO ratios alone would not form a strong enough diagnostic for the presence of AGNs.

To remove the effects of the XDR, the use of double ratios ($HCN/HCO^+$ along with HCN/CO) might prove more useful. Since both HCN and $HCO^+$ have high dipole moments, they both probe high density molecular gas, and therefore their ratio would not be as affected by differences in the fractions of dense molecular gas within the more diffuse gas in these galaxies.

If the ratios of $HCN/HCO^+$ and HCN/CO are such that a galaxy resides in the upper right corner of the plot Fig. 4.10, it would give a strong indication that an AGN is present. However, if the ratios put the galaxy in the lower left, it does not automatically imply that an AGN is not present in the galaxy, simply that the starburst is dominant. This could be a case of a composite AGN and starburst.

In an earlier section, we discussed our observations of both HCN and $HCO^+$ in the ULIRGs Arp 220 and NGC 6240. $HCO^+$(1-0) is a strong emission line in both these galaxies in comparison to HCN(1-0). The $HCO^+$ line was observed to be unexpectedly strong as compared to previous observations. This can be seen clearly in Fig. 4.12 where HCN(1-0) and $HCO^+$(1-0) lines are overlaid for both Arp 220 and NGC 6240. As a result of the strong $HCO^+$ emission line, the $HCN/HCO^+$ ratio in both Arp 220 and NGC 6240 are not very high. Therefore, these galaxies fall in the lower left portion of the plot in Fig. 4.10. They are denoted by a yellow inverted triangle and cyan star on the plot while measurements done by Imanishi et al. (2007) are shown by blue dots. Our earlier $2''$ resolution observations are also shown on the plot with red inverted triangle and green star. Other observations shown as filled black dots in case of starbursts and black circles for Seyfert galaxies were done by various other studies.

Both Arp 220 and NGC 6240 fall in the lower left fraction of the plot, indicating high rates of star formation. Our $2''$ resolution observations do not coincide with the higher resolution observations. However, they still lie in the "Composite AGN" section of the plot. They might not be pure AGNs but have molecular gas affected and irradiated by both AGNs and star formation. This would especially hold in the case of NGC 6240, where two AGNs have been identified using X-ray observations (Komossa et al., 2003). As noted earlier, the absence of AGN-like ratios in NGC 6240

is very likely due to the fact that the bulk of the molecular gas lies between the AGN and does not reside around the AGN.

# Chapter 5

# What lurks in ULIRGs ? – Probing the chemistry and excitation of molecular gas in the nuclei of Arp 220 and NGC 6240

## 5.1 Introduction

Galactic merging is a key step in the evolution and buildup of galaxies in the universe. It is also strongly correlated with the most luminous AGN activity and high star formation rates. Ultra Luminous Infra-Red Galaxies (ULIRGs) emit as much as 90% of their luminosity in the infrared ($L_{IR} > 10^{12} L_{\odot}$). Evidence of ongoing or recent mergers in a substantial fraction of these objects suggests that the merger process is an essential trigger for these energetic and active galaxies (Sanders et al., 1988; Veilleux et al., 2002).

NGC 6240 ($L_{IR} \sim 10^{11.9} L_{\odot}$) & Arp 220 ($L_{IR} \sim 2 \times 10^{12} L_{\odot}$) are often viewed as the prototypical ULIRGs, albeit at slightly different stages of merging. They show high Star Formation Rates (SFRs), $\sim$ 100 and 240 $M_{\odot}$/yr respectively, estimated from IR luminosity (Anantharamaiah et al., 2000; Beswick et al., 2001; Sanders et al., 2003). NGC 6240 exhibits two clearly separated nuclei $\sim 2''$ ($\sim$ 1 kpc, Tacconi et al. 1999) apart, both showing hard X-ray source AGN (Komossa et al., 2003). However, The major gas concentration lies between the two nuclei in the overlap region (Tacconi et al., 1999; Scoville et al., 2000; Engel et al., 2010).

Near infrared imaging of Arp 220 reveals two nuclei separated by $1''$ (projected distance of 370 pc) and one of these has recently been detected in X-rays (Iwasawa et al., 2005). Previous CO imaging at $0.5''$ resolution detected counter-rotating disks in both nuclei with radii $\sim$100 pc, and dynamical masses of 2 x $10^9 M_{\odot}$ in each (Scoville et al., 1997; Sakamoto et al., 1999; Downes & Eckart, 2007). Observations by Clements et al. (2002) and McDowell et al. (2003) using Chandra can neither confirm nor rule out the presence of AGNs. The inferred visible extinctions perpendicular to

the counter-rotating disks, $A_V \sim$ 500-2000 mag, has made direct observation and measurement of physical conditions of the cores of the Arp 220 disks difficult. In particular, the physical conditions of the molecular gas in the nuclei of Arp 220 and in the gas disk of NGC 6240 are poorly determined.

In this paper, we present CARMA molecular line observations of Arp 220 and NGC 6240 at $\sim$ 2″ and 0.6″ resolutions. We observed the HCN(1-0), CS(2-1), HNC(1-0) and $HCO^+$(1-0) transitions and also the isotopomer lines $H^{13}CN$(1-0) and $^{13}CS$(2-1) simultaneously, at similar resolutions and with consistent calibrations. CO(1-0) and $^{13}CO$(1-0) transitions were also observed for each of the galaxies at 2″ resolution. These two lines were also observed at 0.6″ resolution for Arp 220. Multi-band imaging has allowed excitation analysis of HCN, $HCO^+$, HNC and CS along with CO transitions to constrain the properties of the gas. Our unique dataset of high sensitivity observations of different lines at similar resolutions enables the derivation of line ratios of faint high excitation lines.

In section 2, we discuss the details of the observations of Arp 220 and NGC 6240 using CARMA at both 2″ and 0.5 - 0.8″ resolution. Section 3 describes the measurements and results from these observations for both systems and compares these with previous measurements. In section 4, we analyze the physical conditions of the molecular gas based on our observations and measurements. Section 5 summarizes our analysis and results.

## 5.2 Observations

The Combined Array for Research in Millimeter-wave Astronomy (CARMA) was used to observe CO(1-0), HCN(1-0), CS(2-1), HNC(1-0), and $HCO^+$(1-0) transitions along with isotopomer lines $^{13}CO$(1-0), $H^{13}CN$(1-0), and $^{13}CS$(2-1) in Arp 220 and NGC 6240. Observations in the C configuration used antenna separations between 26 - 370 m and led to a resolution of $\sim$1.7 - 2″. In the B configuration, the antennas were spaced more widely at 100 - 1000 m and achieved a higher resolution of $\sim$0.5 - 0.8″. The C configuration observations were carried out in good ($\tau_{112GHz} < 0.3$) to fair ($0.5 < \tau_{112GHz} < 0.3$) weather conditions during several runs between December 2012 and November 2013. The B configuration observations were done between January 2013 and January 2014 and were of similar high quality.

The spectrometer bands were positioned independently within the IF bandwidth to simultaneously observe the HCN(1-0), CS(2-1), HNC(1-0), and $HCO^+$(1-0) lines along with isotopomer lines $H^{13}CN$(1-0) and $^{13}CS$(2-1) in both Arp 220 and NGC 6240. The correlator was configured to have eight 500 MHz bands in the lower and upper sidebands with 95-channel spectral resolution per band. Each band corresponds to $\sim$1500 km $s^{-1}$ in velocity space. Each channel corresponds to 5.208 MHz width, $\sim$15 km $s^{-1}$. CO(1-0) and $^{13}CO$(1-0) were observed in a separate correlator configuration. The data were reduced using the MIRIAD (Multichannel Image Reconstruction, Image

Analysis and Display) package. Subsequent analysis, involving for example line profiles and intensity measurements, used MATLAB.

Total observation time for Arp 220, in C configuration, for observations of HCN(1-0), CS(2-1), HNC(1-0), $HCO^+$(1-0), $H^{13}CN$(1-0), and $^{13}CS$(2-1) lines was 48.5 hours. In the case of NGC 6240, the observation time was 36.7 hours. Observing times for CO(1-0) and $^{13}CO$(1-0) were 16.5 hours and 16.4 hours respectively for Arp 220 and NGC 6240. In the B configuration, the total observation time for Arp 220 for observations of HCN(1-0), CS(2-1), HNC(1-0), $HCO^+$(1-0), $H^{13}CN$(1-0) and $^{13}CS$(2-1) lines was 49 hours and for NGC 6240, 43.9 hours. For Arp 220, CO(1-0) and $^{13}CO$(1-0) were observed for 34.4 hours. Bad weather prevented these lines from being observed for NGC 6240 in the B configuration.

## 5.3 Results

Our observations are the first comprehensive high resolution interferometric measurements of lower transition lines of high dipole moment molecules like HCN for these galaxies. To compare the lines in both galaxies with each other and with earlier studies, we calculated velocity integrated fluxes and luminosities for observations at both $2''$ and $0.6''$ resolutions using Solomon et al. (1992b). The results along with measurements from earlier studies, are presented in Table 5.1.

Fig. 5.1 and Fig. 5.3 show the spectra of the high density gas tracers for Arp 220 and NGC 6240 respectively at $2''$ resolution. The high resolution interferometric observations of CO(1-0) for both the galaxies are in Fig. 5.2. Fig. 5.4 shows the integrated line intensity images for HCN(1-0) emission at $0.6''$ resolution for Arp 220 and NGC 6240. The beam size is in blue in the lower right corner. The two nuclei of Arp 220 are clearly seen in this image. The western nuclei is more clearly seen because of stronger emission from it.

In the case of Arp 220, the double peaked profile expected from the counter-rotating molecular gas disks observed in earlier studies (Scoville et al., 1997; Downes & Solomon, 1998; Greve et al., 2009) is seen in our CO(1-0) observations. HCN(1-0), CS(2-1), HNC(1-0), and $HCO^+$(1-0) display a similar double peaked profile. The peaks are stronger and more clearly distinguishable in these lines than in CO. $^{13}CO$(1-0) is not clearly a double peaked profile, but seems more square. This suggests that the $^{13}CO$(1-0) flux may originate largely from the blueshifted western nucleus of Arp 220. The difference in the CO(1-0) and $^{13}CO$(1-0) profiles indicates differences in either the dynamics of the molecular gas or its optical depth in the two nuclei. In this case, it seems most likely that the profile shape difference is probably due to the $^{13}CO$(1-0) optical depth being higher in the western nuclei. We were able to detect $H^{13}CN$(1-0) (Fig. 5.1(f)) at more than the $4\sigma$ level; $^{13}CS$(2-1) was not detected.

All the lines detected in NGC 6240 show a Gaussian-like velocity profile, in contrast to Arp 220.

This suggests that turbulence or disordered random motions rather than rotation is dominating the line profiles in NGC 6240 and is consistent with the molecular and dust continuum emission being concentrated between the two stellar nuclei (Scoville et al., 2015), rather than centered on each of the stellar nuclei as in Arp 220. This seems to be the case on a wide range of spatial scales. This is not the case in Arp 220 where the double peak features evolve with the different transition lines that reflect different densities and temperatures (Greve et al., 2009). Isotopomer lines were not detected at any significant level in NGC 6240.

Our observations of CO(1-0), for both Arp 220 and NGC 6240, agree with many previous measurements, for example (Scoville et al., 1997; Downes & Solomon, 1998; Bryant & Scoville, 1999), giving confidence in our data, methodology and calibrations. However, there are significant discrepancies in between our measurements of $HCO^+$(1-0) flux densities and those from previous studies, especially in comparison with single dish observations. Our fluxes are much as twice those reported by Solomon et al. (1992a), Graciá-Carpio et al. (2006), and Nakanishi et al. (2005) for both the galaxies (see Table 5.1). The discrepancy may be due to calibration in other observations. As we discuss below, this discrepancy may reflect significant differences between abundances in galactic sources and distant mergers.

Table 5.1: Molecular Transition Lines Detected: Arp 220 and NGC 6240

| Line | Arp 220 | | | | | NGC 6240 | | | | |
|---|---|---|---|---|---|---|---|---|---|---|
| | FWHM | $S_\nu\Delta v$ | $L'^c$ | Telescope | References | FWHM | $S_\nu\Delta v$ | $L'^c$ | Telescope | References |
| | km s$^{-1}$ | Jy km s$^{-1}$ | x10$^9$ K km s$^{-1}$ pc$^2$ | | | km s$^{-1}$ | Jy km s$^{-1}$ | x10$^9$ K km s$^{-1}$ pc$^2$ | | |
| CO(1-0) | 504 | 410 ± 41 | 5.9 ± 0.6 | OVRO | Scoville et al. 1997 | 370 | 314 ± 64 | 8.3 ± 1.7 | IRAM 30m | Solomon et al. 1997 |
| | ... | 384 ± 115 | 5.5 ± 1.7 | OVRO | Scoville et al. 1991 | 469 | 324 ± 33 | 8.6 ± 0.9 | OVRO | Bryant & Scoville 1999 |
| | 480 | 496 ± 99 | 7.2 ± 1.4 | IRAM 30 m | Solomon et al. 1997 | | 322 ± 29 | 8.5 ± 0.8 | | |
| | 500 | 385 ± 40 | 6.1 ± 0.64 | CARMA | 2″, This Work | 400 | 304 ± 30 | 8.9 ± 0.88 | CARMA | 2″, This Work |
| | 450 | 350 ± 35 | 5.2 ± 0.52 | CARMA | 0.8″, This Work | ... | ... | ... | ... | ... |
| HCN(1-0) | ... | 35 ± 11 | 0.85 ± 0.27 | IRAM PdBI | Radford et al. 1991 | ... | 26 ± 8 | 1.17 ± 0.36 | IRAM 30 m | Solomon et al. 1992a |
| | 550 | 59 ± 12 | 1.44 ± 0.29 | IRAM 30 m | Greve et al. 2009 | 340 | 13 ± 3 | 0.58 ± 0.13 | IRAM 30 m | Greve et al. 2009 |
| | 530 | 48 ± 14 | 1.17 ± 0.34 | IRAM 30 m | Krips et al. 2008 | ... | 14 ± 4 | 0.63 ± 0.18 | NMA | Nakanishi et al. 2005 |
| | 565 | 42 ± 4 | 1.1 ± 0.11 | CARMA | 2″, This Work | 350 | 26 ± 2.6 | 1.3 ± 0.13 | CARMA | 2″, This Work |
| | 550 | 49 ± 5 | 1.3 ± 0.13 | CARMA | 0.8″, This Work | 325 | 24 ± 2.4 | 1.2 ± 0.12 | CARMA | 0.8″, This Work |
| CS(2-1) | 339 | 12 ± 3 | 0.24 ± 0.06 | IRAM 30 m | Greve et al. 2009 | ... | 7.5 ± 1.5 | 0.3 ± 0.06 | Herschel | Papadopoulos et al. 2014 |
| | 345 | 11 ± 0.1 | 0.24 ± 0.02 | CARMA | 2″, This Work | 175 | 3 ± 0.6 | 0.12 ± 0.02 | CARMA | 2″, This Work |
| | 375 | 17 ± 2 | 0.38 ± 0.04 | CARMA | 0.8″, This Work | 200 | 12 ± 1 | 0.05 ± 0.01 | CARMA | 0.8″, This Work |
| HNC(1-0) | 516 ± 38 | 55 ± 11 | 1.28 ± 0.26 | IRAM 30 m | Huettemeister et al. 1995 | ... | 14 ± 7 | 0.60 ± 0.30 | SEST | Aalto et al. 2002 |
| | ... | 34 ± 7 | 0.79 ± 0.16 | SEST | Aalto et al. 2002 | | | | | |
| | 407 | 43 ± 8 | 0.96 ± 0.19 | IRAM 30 m | Greve et al. 2009 | | | | | |
| | 400 | 53 ± 5 | 1.4 ± 0.13 | CARMA | 2″, This Work | 275 | 19 ± 4 | 0.89 ± 0.2 | CARMA | 2″, This Work |
| | 425 | 58 ± 6 | 1.5 ± 0.15 | CARMA | 0.8″, This Work | 275 | 18 ± 6 | 0.85 ± 0.3 | CARMA | 0.8″, This Work |
| $HCO^+$(1-0) | ... | 20 ± 6 | 0.48 ± 0.14 | IRAM PdBI | Radford et al. 1991 | 420 | 21 ± 3 | 0.93 ± 0.13 | NMA | Nakanishi et al. 2005 |
| | ... | 19 ± 6 | 0.46 ± 0.14 | IRAM 30 m | Solomon et al. 1992a | ... | 25 ± 8 | 1.11 ± 0.35 | IRAM 30 m | Graciá-Carpio et al. 2006 |
| | ... | 22 ± 7 | 0.53 ± 0.17 | IRAM 30 m | Graciá-Carpio et al. 2006 | | | | | |
| | 570 | 37 ± 4 | 1.0 ± 0.11 | CARMA | 2″, This Work | 470 | 40 ± 4 | 2.0 ± 0.19 | CARMA | 2″, This Work |
| | 450 | 36 ± 4 | 0.96 ± 0.1 | CARMA | 0.8″, This Work | 470 | 48 ± 5 | 2.3 ± 0.2 | CARMA | 0.8″, This Work |
| $^{13}$CO(1-0) | 369 | 9 ± 2 | 0.14 ± 0.03 | IRAM 30 m | Greve et al. 2009 | | | | | |
| | 380 | 14 ± 2 | 0.24 ± 0.04 | CARMA | 2″, This Work | ... | ... | ... | ... | ... |
| | 300 | 11 ± 1 | 0.19 ± 0.02 | CARMA | 0.8″, This Work | ... | ... | ... | ... | ... |
| H$^{13}$CN(1-0) | 400 | 15 ± 2 | 0.43 ± 0.06 | CARMA | 2″,This Work | ... | ... | ... | ... | ... |
| | 380 | 17 ± 2 | 0.48 ± 0.05 | CARMA | 0.8″, This Work | ... | 7 ± 2 | 0.37 ± 0.1 | CARMA | 0.8″, This Work |
| $^{13}$CS(2-1) | ... | ... | ... | ... | ... | ... | ... | ... | ... | ... |

## 5.4 Analysis & Discussion

### 5.4.1 High Density Molecular Gas traced in HCN, CS, HNC, and $HCO^+$

A major goal of this study was to measure various molecular tracers at matched resolution and with consistent calibration. This enables analysis of the relative line strengths to provide reliable molecular abundances and gas physical conditions.

For the molecular excitation analysis, we used the Large Velocity Gradient or Sobolev formalism to treat the radiative transfer and then solve for the molecular level populations assuming statistical equilibrium (Scoville & Solomon, 1974; Goldreich & Kwan, 1974). For the line photon escape probabilities we assume a spherical cloud geometry yielding $\beta = (1 - e^{-\tau})/\tau$ where $\tau$ is the line optical depth.

The molecular level populations are determined by detailed balance of collisional excitation and de-excitation by $H_2$ molecules, spontaneous decay in the permitted dipole transitions and absorption and stimulated emission in optically thick molecular lines. The latter is termed 'line photon trapping' and it effectively results in the spontaneous decay rates being reduced by the photon escape probability, i.e. the Einstein A coefficient is replaced by $\beta$A. This means that the critical densities of the transitions can be considerably reduced when the transitions become optically thick. Scoville et al. (2015) made use of a 2-level analytic approximation for the excitation analysis for CS (7-6) and HCN (4-3) in Arp 220 and NGC 6240; here, we incorporate the full multi-level statistical equilibrium to yield more accurate results.

Simultaneous solutions for the multilevel non-LTE populations were obtained using the Newton-Raphson method with code made available by Jin Koda. The populations for each molecular species are a function of the gas volume density $n_{H2}$, the gas kinetic temperature $T_k$, the molecular abundance $X_m$ relative to $H_2$, and the line of sight velocity gradient $dv/dr$. The collisional cross sections are from RADEX (van der Tak et al., 2007). For the adopted kinetic temperature and $dv/dr$ appropriate for each source, the excitation temperature, $T_x$ and optical depth of each rotational transition can then be determined as a function of $n_{H2}$ for an adopted molecular abundance. As a starting point, we used abundances for the different molecule similar to those of Galactic GMCs (see below). We then let those relative abundances vary in order that a consistent volume density $n_{H2}$ is derived for each observed species – HCN, CS, HNC, and $HCO^+$. The parameters used for the LVG model are detailed in Table 5.2 for Arp 220 and NGC 6240.

Our observations constrain the peak *apparent* brightness temperature, $T_b$, for each of the transitions HCN(1-0), CS(2-1), HNC(1-0), and $HCO^+$(1-0) in both Arp 220 and NGC 6240. Assuming the lines are optically thick, these apparent brightness temperatures are 15-25 K for Arp 220 and 10-20 K for NGC 6240. The apparent brightness temperature is lower than the true brightness temperature due to beam dilution effects if the emission source does not entirely fill the synthe-

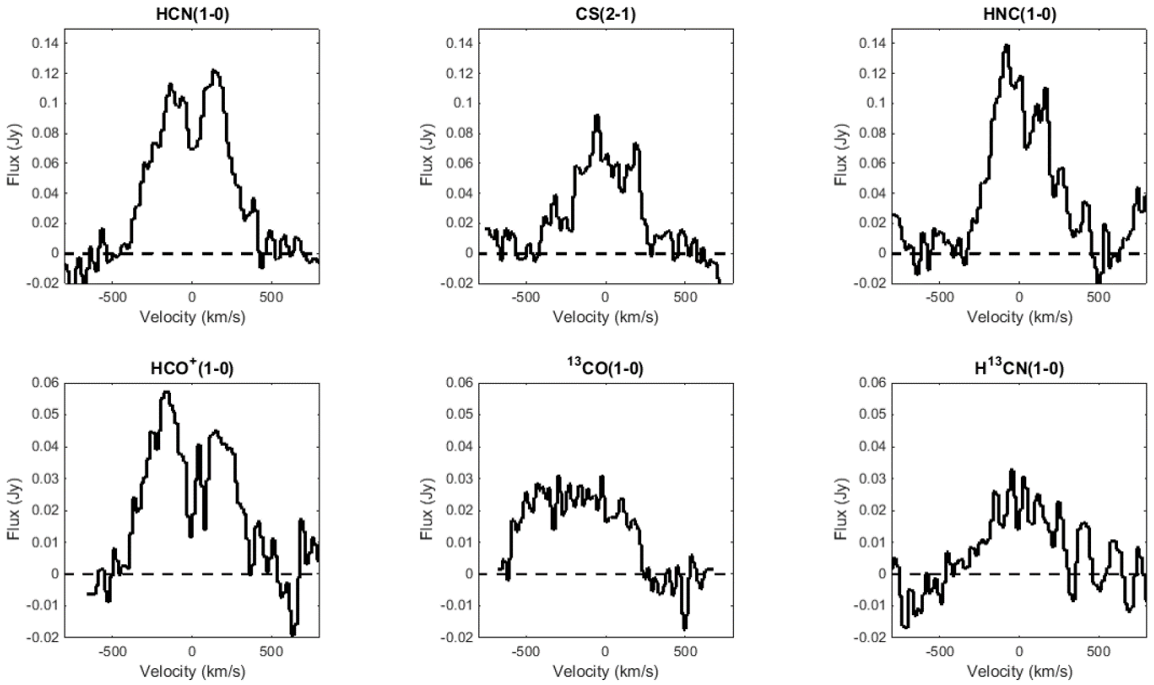


Figure 5.1: Molecular line spectra for Arp 220. The velocity scale for all transitions is the same and centered at the galaxy redshift. The flux scale for HCN(1-0), CS(2-1), and HNC(1-0) transition spectra (panels (a)-(c)) are the same. The $HCO^+$(1-0), $^{13}CO$(1-0), and $H^{13}CN$(1-0) spectra (panels (d)-(f)) scales are stretched to show the weaker spectra features.

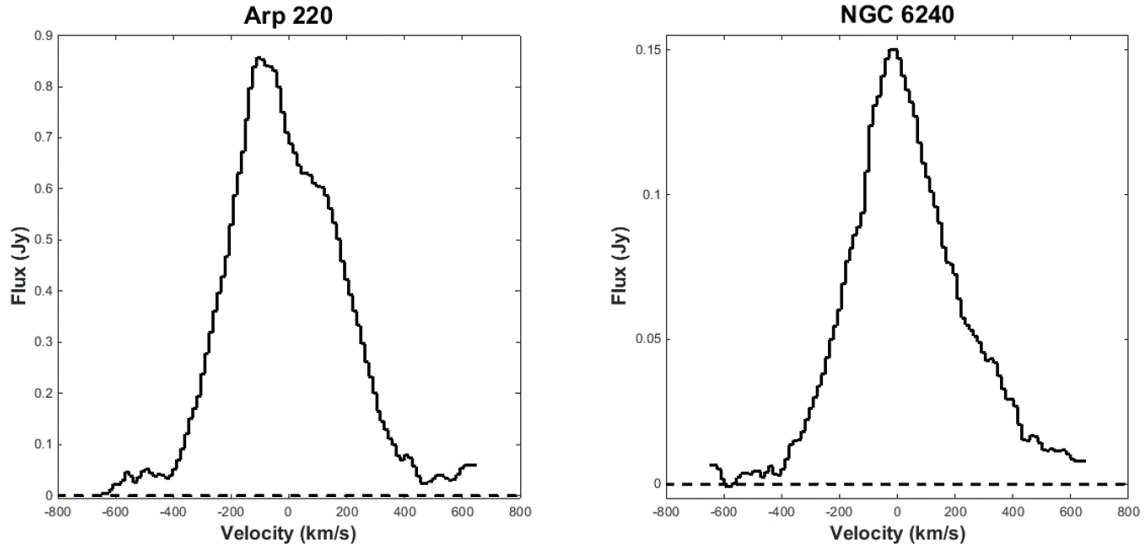


Figure 5.2: Molecular CO(1-0) spectra for Arp 220 and NGC 6240. The velocity scales are the same as those adopted in Fig. 5.1 for Arp 220 and Fig. 5.3 for NGC 6240. The velocity limits are the same for both the galaxies. In both galaxies the CO intensity is much greater than for the other lines. For NGC 6240, the scale adapted here is expanded by a factor of 6 compared to Fig. 5.3.

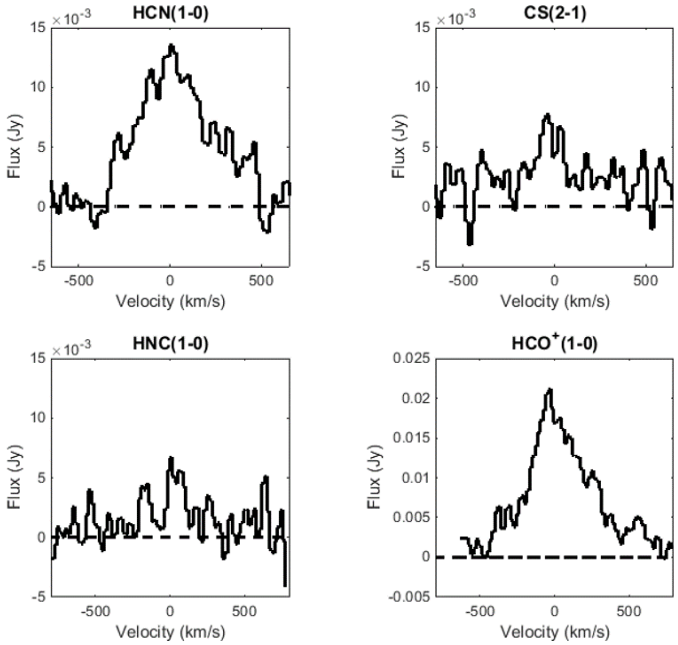


Figure 5.3: Molecular line spectra observed in NGC 6240. The velocity scale for all transitions is same and centered at the galaxy redshift. HCN(1-0), CS(2-1), and HNC(1-0) transition spectra (panels (a)-(c)) are on the same flux scale. The $HCO^+$(1-0) spectra has the highest peak of the transitions and its flux scale is higher. Note that the vertical scales in all panels except the panel (d) have a scale factor of $10^{-3}$.

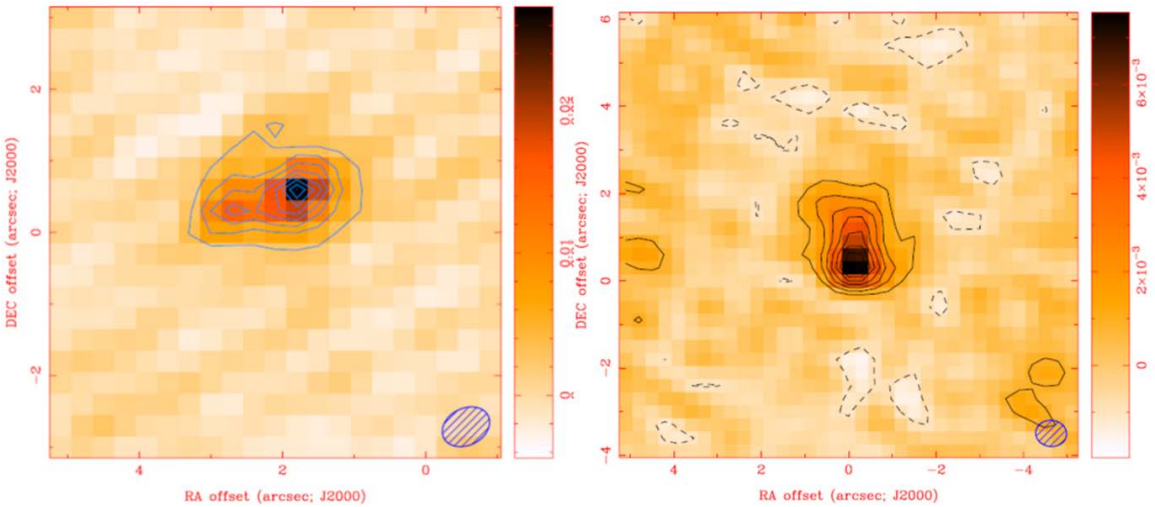


Figure 5.4: Arp 220 (left) and NGC 6240 (right) Integrated Line Intensity images for HCN(1-0) emission at 0.6″ resolution. Contours are at $2\sigma$ separations starting at $4\sigma$. The beam size is shown in the lower right corner for both images.

Table 5.2: Constants used for Large Velocity Gradient modeling for Arp 220 and NGC 6240

| | | | | Arp 220 | | NGC 6240 | |
|---|---|---|---|---|---|---|---|
| Line | B | $A_{ul}$ | Abundance, X | $T_b$ | dv/dr | $T_b$ | dv/dr |
| | GHz | $s^{-1}$ | Relative to $H_2$ | K | $s^{-1}$ | K | $s^{-1}$ |
| HCN(1-0) | 44.32 | 2.4 x $10^{-5}$ | 2 x $10^{-8}$ | 22.1 | 1.3 x $10^{-13}$ | 15.2 | 3 x $10^{-14}$ |
| CS(2-1) | 24.50 | 1.7 x $10^{-5}$ | 5 x $10^{-9}$ | 13.2 | 1 x $10^{-13}$ | 8 | 1.5 x $10^{-14}$ |
| HNC(1-0) | 45.33 | 2.7 x $10^{-5}$ | 4 x $10^{-9}$ | 22.8 | 1 x $10^{-13}$ | 10.4 | 2.3 x $10^{-14}$ |
| $HCO^+$(1-0) | 44.59 | 4.3 x $10^{-5}$ | 4 x $10^{-8}$ | 14.4 | 1.3 x $10^{-13}$ | 19.1 | 4 x $10^{-14}$ |

sized beam. To compensate for this partial filling, we make use of the observed CO (1-0) *apparent* brightness temperature and assume that this emission has a similar beam filling factor as the high dipole moment molecules. Since the CO levels are more easily thermalized ($T_x = T_k$), the ratio of the observed $T_b$ of each molecular line to that of CO provides an approximate estimate of the ratio of each molecular excitation temperature to the gas kinetic temperature $T_k$. We then try to match the molecular excitations with the observationally constrained $T_x/T_k$.

The preceding methodology was used to estimate the gas density for each of the observed transitions in Arp 220 and NGC 6240. In the case of Arp 220, the observed emission nucleus is ∼130 pc in diameter and in NGC 6240, the diameter of our imaged disk is ∼380 pc. Using the velocity FWHM of each transition in the respective galaxies, we obtained the values of dv/dr listed in Table 5.2. For both galactic nuclei, we adopt a mean kinetic temperature of ∼45 K based on the dust temperature measured in IR spectral energy distributions (Sanders et al., 1991). We assume that the dust and gas are likely to be approximately in thermal equilibrium, as should be the case at densities $n_{H2} > 10^4$ $cm^{-3}$ (Goldreich & Kwan, 1974).

We also assumed the abundance of HCN relative to molecular hydrogen, $H_2$ to be similar to that seen in Galactic clouds, with $X_{HCN} \sim 2$ x $10^{-8}$ (Bergin et al., 1996; Lahuis & van Dishoeck, 2000) where $n_m = X_{HCN} n_{H2}$. In the case of CS, the galactic abundance has been observed to be $X_{CS} \sim 5$ x $10^{-9}$ (Paglione et al., 1995; Shirley et al., 2003; Bergin et al., 1997).

For the HNC(1-0) transition, Graninger et al. (2014) postulate $X_{HNC} \sim X_{HCN}$. Therefore, we first adopted $X_{HNC} \sim 2$ x $10^{-8}$ for our calculations. However, this assumption resulted in values of $n_{H2}$ that were too low compared with measurements made using other molecular species. We then adjusted the abundance of HNC to $X_{HNC}$ to $\sim 4$ x $10^{-9}$, 5 times lower than previously assumed and redid our calculations. The adjusted abundances resulted in more comparable values of $n_{H2}$. The lower abundance of HNC in contrast to HCN could be due to the destruction of HNC molecules at higher temperatures. At gas densities $n(H_2)>10^5$ $cm^{-3}$, the HNC chemistry is dominated by reactions like HNC+O⟶CO+NH which would destroy HNC at higher temperatures (Goldsmith et al., 1981; Hirota et al., 1998).

Initially, we adopted an abundance of $HCO^+$ relative to molecular hydrogen, $H_2$ that was twice

that of HCN (Acharyya & Herbst, 2015). Hence, $X_{HCO^+} \sim 4 \times 10^{-8}$. With this assumption the derived $n_{H2}$, yielding the observed ratio $T_x/T_k$, was an order of magnitude lower than expected from the excitation of the other molecular species. In order that the derived $n_{H2}$ agree, the $HCO^+$ abundance was reduced to $X_{HCO^+} \sim 4 \times 10^{-9}$. In fact, the abundance of $HCO^+$ is expected to decline at higher gas volume densities due to increased recombination in denser regions. The required low abundance may simply reflect the fact that the density of the entire nuclear gas concentration is high, not unlike core regions enveloped in a lower density medium.

The left panels in Fig. 5.5 and Fig. 5.6 show the ratio $T_x/T_k$ calculated for all the transitions in Arp 220 and NGC 6240. The observed values of $T_x/T_k$ measured for each transition are shown as diamond shaped points on the plots. For the adopted abundances in Arp 220, the required molecular hydrogen densities, $n_{H2}$ are $5 \times 10^4$ cm$^{-3}$ for HCN, $4 \times 10^4$ cm$^{-3}$ for CS, $1 \times 10^5$ cm$^{-3}$ for HNC, and $3 \times 10^4$ cm$^{-3}$ for $HCO^+$. For the adopted abundances in NGC 6240, the required densities, $n_{H2}$ are $1 \times 10^4$ cm$^{-3}$ for HCN, $7 \times 10^3$ cm$^{-3}$ for CS, $1 \times 10^4$ cm$^{-3}$ for HNC, and $2 \times 10^4$ cm$^{-3}$ for $HCO^+$.

The right panels in Fig. 5.5 and Fig. 5.6 show the line optical depth for each of the transitions as a function of density. The optical depths for the above mentioned densities are marked with diamond shaped points in the subplots. In the case of Arp 220, the optical depths, $\tau$ are 20 for HCN, 4 for CS, 8 for HNC and 4 for $HCO^+$. For NGC 6240, the optical depth $\tau$ is 40 for HCN, 10 for CS, 3 for HNC and 6 for $HCO^+$. Thus, these lines are optically thick as assumed earlier for both galaxies. $^{13}CO$ intensity measurements did not fit the model used for the other lines and yielded optical depth, $\tau \approx 1$ and $n_{H2} \sim 10^2$. This may imply either that the $^{13}CO/CO$ abundance is much lower than the galactic abundances or that the $^{13}CO$ emission is originating from a clumpy medium.

In Arp 220, measurements and calculations for all species produced similar molecular gas densities for the assumed abundances. As already described, the assumed abundances of HNC and $HCO^+$ were adjusted to fit the molecular hydrogen densities. Since $n_{H2}$ should be constant regardless of which molecular species was used to make the estimate, this suggests that the abundances in galactic sources may not apply to ULIRGs.

In the case of NGC 6240, we adopted the abundances derived for Arp 220. All the transitions indicate molecular gas densities within a factor of 2 of these assumed abundances. As in the case of Arp 220, the values of $n_{H2}$ calculated from HNC and $HCO^+$ measurements, suggests a difference between abundances of these species in ULIRGs and galactic clouds.

#### 5.4.1.1 Reduced Abundances of HNC and $HCO^+$ in ULIRGs

In summary, the consistent $H_2$ density is $5 \times 10^4$ cm$^{-3}$ in Arp 220 and $10^4$ cm$^{-3}$ in NGC 6240. This value was obtained for both the $2''$ and 0.5 - $0.8''$ resolution observations. The initial abundances we adopted were typical of Galactic sources. However, in the case of HNC, this adopted abundance

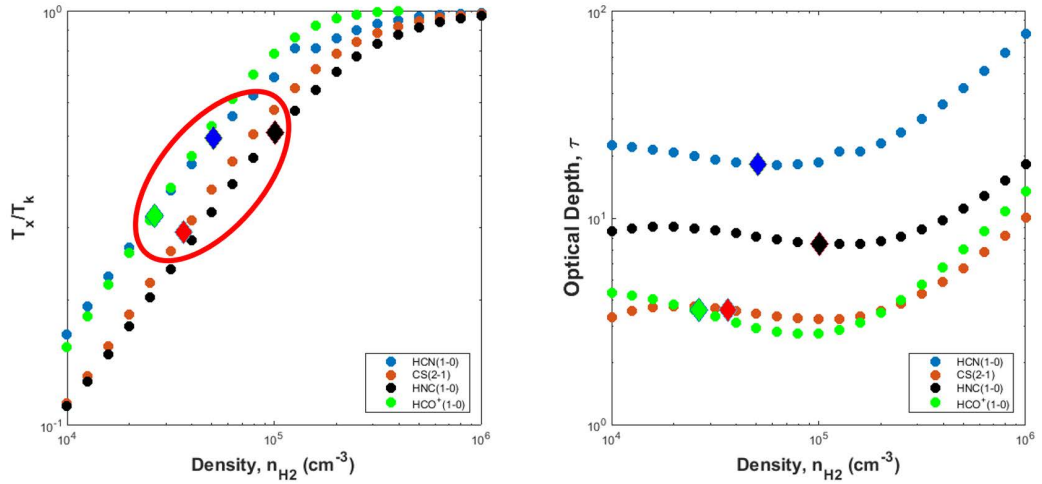


Figure 5.5: Arp 220: On the left, the ratio of the level excitation temperature to the gas kinetic temperature ($T_x/T_k$) on the abscissa and the density of HCN(1-0), CS(2-1), HNC(1-0) and $HCO^+$(1-0) lines. On the right, optical depths of each of the lines is shown.

(Graninger et al., 2014) led to the $H_2$ densities 5 times lower than those measured using HCN. For $HCO^+$, the assumed Galactic abundance (Acharyya & Herbst, 2015), implied an $H_2$ density an order of magnitude lower than for HCN. These discrepancies imply that the HNC and $HCO^+$ abundances in the ULIRGs Arp 220 and NGC 6240 are very significantly reduced from what is implied for standard Galactic GMC cloud cores. The disagreement in the values are probably rooted in the physical conditions in the molecular gas in these galaxies. HNC is preferentially destroyed at higher temperatures than HCN, therefore, would result in lower abundances of HNC. $HCO^+$ abundances might be diminished as a result of recombination in very dense conditions.

The mean gas density in the nuclei of Arp 220 is 5 times higher than that in NGC 6240, although the dynamical masses of the galaxies are similar $\sim$5 x $10^9$ $M_\odot$ in the disk of NGC 6240 (Tacconi et al., 1999) and $2 \times 10^9$ $M_\odot$ in each of the disks of Arp 220 (Scoville et al., 1997, 2015). The denser molecular gas in Arp 220 compared to NGC 6240 may reflect the fact that Arp 220 is very likely more advanced in the merging process and the gas is concentrated in the two nuclear disks rather than in the interaction zone between the nuclei as in NGC 6240.

### 5.4.2 HCN and HNC line ratios: XDR vs PDR regions

The HCN and HNC abundance ratios provide constraints on the temperature, density, and environment of the molecular gas in galaxies. An important aspect is whether the region is Photon dominated (PDR) or X-ray dominated (XDR). Differentiating between these is insightful; a PDR would imply that the molecular gas is mainly radiated by extreme star formation while an XDR would imply that the molecular gas is irradiated by an AGN nucleus. Since it is not always clear

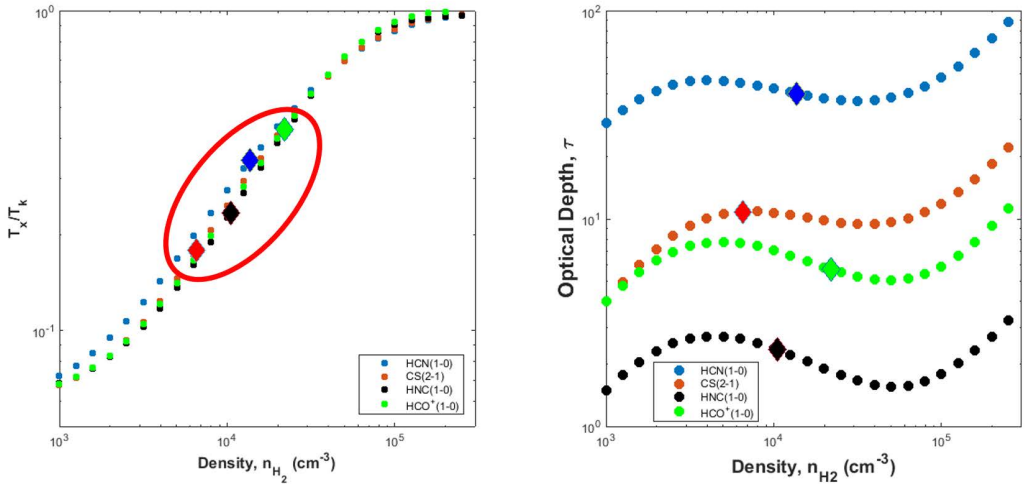


Figure 5.6: NGC 6240: On the left, the ratio of the level excitation temperature to the gas kinetic temperature ($T_x/T_k$) on the abscissa and the density of HCN(1-0), CS(2-1), HNC(1-0) and $HCO^+$(1-0) lines. On the right, optical depths of each of the lines is shown.

if there is an obscured AGN nuclei in the core of a galaxy, this can provide important information about the nature of the luminosity source.

PDRs are characterized by the irradiation of molecular gas clouds in star forming regions by far ultraviolet (FUV) radiation emitted by young, nearby, OB type stars. O and B stars dominate the radiation from starbursts, which is mostly in the far-ultraviolet, 6.0<E<13.6 eV (Tielens & Hollenbach, 1985). Since a starburst galaxy will be populated by a large number of OB stars, it is expected that the molecular gas in such regions will be dominated by PDR chemistry. FUV photons dominate the ionization and spectral properties and physical conditions such as temperature and densities especially on the surface of the molecular clouds.

XDRs are characterized by the irradiation of molecular gas clouds by intense X-ray fluxes. Molecular gas can be irradiated by X-rays in a number of different astrophysical scenarios, near Active Galactic Nuclei (AGNs), supernovae remnants and X-ray binaries. The dominant source of X-rays in ULIRGs such as Arp 220 and NGC 6240, which may have supermassive accreting black holes, would be AGNs. These are capable of producing hard X-ray photons with energies $> 1$ keV, which can penetrate through large column densities, $\sim 10^{22}$ cm$^{-2}$, before being absorbed by the molecular gas because of the large energy per photon present in the radiation (Maloney et al., 1996). This can strongly alter the chemical and thermal properties of the clouds that are opaque to other kinds of radiation.

The effects of X-ray irradiation can also result in infrared and submillimeter emission from the irradiated molecular clouds. By observing these effects, the presence of a XDR (indicating perhaps the existence of an obscured AGN) can be deduced. Many investigations into the properties of

XDRs have been carried out over the years (Krolik & Kallman, 1983; Lepp & McCray, 1983; Bakes & Tielens, 1994; Maloney et al., 1996). Recent studies (Meijerink & Spaans, 2005; Meijerink et al., 2007), employ updated models, including vast range of densities and temperatures, to predict the properties of emission lines of molecular species such as $HCO^+$, HCN, HNC, and CS. These models and our new emission line observations enable us to probe the molecular gas environment and the nature of the energy source both Arp 220 and NGC 6240.

X-ray observations of both Arp 220 and NGC 6240, studies have suggested the presence of AGNs. Since both galaxies are merging systems, it appears that they both have Supermassive Black Holes (SMBHs). While these systems are at different merging states, they have not gone through the coalescing stage which would include the merger of the black holes at their cores. In Arp 220, we clearly observe two counter-rotating disks of gas, both of which probably have black holes at their centers. The presence of at least one black hole has been indicated from X-ray observations (Clements et al., 2002; McDowell et al., 2003), the other has yet to be detected. In the case of NGC 6240, the two black holes have been detected (Komossa et al. 2003) using Chandra X-Ray Observatory.

Using the molecular emission line measurements, we might be able to detect the presence of SMBHs in the midst of the molecular gas if the molecular clouds are being irradiated under XDR conditions. Given the very high column densities of dust, the absence of the optical emission line ratios characteristic of AGN does not preclude the presence of a SMBH. Line ratio measurements for the molecular species consistent with the XDR models would be a very strong indicator of its presence.

The densities of molecular gas that we are probing using high density gas tracers like HCN, HNC and CS are expected to be of the order of $10^4$ cm$^{-3}$ to $10^6$ cm$^{-3}$. HCN and HNC molecules have very similar critical densities because of their similar dipole moments. Therefore, the line ratios should be strong indicators of their abundance and the environment of the molecular gas. The models of XDRs indicate that the HCN/HNC column density ratio is diminished (and lower than unity) compared to PDRs and quiescent cloud regions for gas densities around $10^5$ cm$^{-3}$. Steady-state excitation models show that the abundance of HCN and its isotopomer HNC decreases with increasing density and temperature (Schilke et al., 1992). Values for the HCN/HNC abundance ratio above unity are consistent with steady-state models for higher-density gas at higher temperatures (Meijerink et al., 2007). An HNC/HCN abundance ratio lower than unity suggests a rather quiescent, low temperature gas.

At higher temperatures HNC tends to be selectively destroyed in favor of HCN as long as the medium is not highly ionized. Therefore, HCN/HNC is roughly unity in PDR sources, but lower than unity in XDR sources. The HNC/HCN abundance ratio is expected to be around 0.9, if the standard neutral production paths are followed (Goldsmith et al., 1981). In a highly ionized

Table 5.3: HCN and HNC Line Ratios for Arp 220 and NGC 6240

| Galaxy | $\frac{\text{HCN(1–0)}}{\text{HNC(1–0)}}$ | Reference |
|---|---|---|
| NGC 3079 | 2.15 ± 0.67 | Pérez-Beaupuits et al. (2007) |
| NGC 1068 | 2.01 ± 0.65 | Pérez-Beaupuits et al. (2007) |
| NGC 2623 | 1.4 | Aalto et al. (2002) |
| NGC 1365 | 1.35 ± 0.37 | Pérez-Beaupuits et al. (2007) |
| NGC 7469 | 1.50 ± 0.57 | Pérez-Beaupuits et al. (2007) |
| L1489 | 0.83 ± 0.17 | Hirota et al. (1998) |
| L1521B | 0.5 ± 0.12 | Hirota et al. (1998) |
| ARP 220 | 0.79 ± 0.1 | This Work |
| NGC 6240 | 1.39 ± 0.2 | This Work |

medium, high HCN/HNC ratios would be prevented since $HCNH^+$ can form HCN and HNC with equal probability (Aalto et al., 2002; Wang et al., 2004). Shocks can selectively destroy HNC and could significantly increase the steady-state HCN/HNC abundance ratio (Schilke et al., 1992). Both HCN and HNC may also be pumped by an intense mid-IR radiation field boosting the emission from low density regions where the lines would not be collisionally excited. For HNC the interaction with the IR radiation is even stronger than for HCN, thus increasing the likelihood for IR pumping in extreme IR galaxies

Table 5.3 displays the HCN/HNC line intensity ratios for the 1–0 transition for Arp 220 and NGC 6240 compiled using values from other sources such as Seyferts, Liners and Galactic Molecular Clouds (GMCs) for comparison. The uncertainty in the line ratios for our measurements are based on the uncertainty in our basic flux observations.

The dichotomy in the measurements for Arp 220 and NGC 6240 can be clearly seen. While the HCN/HNC ratio is less than unity for Arp 220, that is not the case for NGC 6240. The ratio for Arp 220 is clearly less than unity. As discussed earlier, a ratio less than unity indicates the presence of a strongly irradiated XDR, possibly by an AGN, at the cores of Arp 220. Since HNC is a strong line in both nuclei as compared to HCN, there is a clear indication that both may house an AGN irradiating the molecular gas.

In contrast, NGC 6240, where two have been AGN detected in other observations, displays a line ratio higher than unity. Such a ratio is expected from molecular gas with PDR conditions. That is not to say that a XDR does not exist within the galaxy but certainly indicates that the molecular gas clouds we are observing have been mostly been irradiated by radiation originating from star forming regions. The ratio observed in NGC 6240 is very similar to other known star forming galaxies as shown in Table 5.3. This is consistent with the fact that the molecular gas peak lies between the two nuclei and not on top of them.

In summary, the diminished HCN/HNC ratio in both nuclei of Arp 220 may indicate the presence

of an XDR being associated with an AGN. NGC 6240 does not show a diminished HCN/HNC ratio, despite confirmed AGN detections, presumably because the molecular gas lies between the two nuclei and is not irradiated by the AGN.

## 5.5 Summary

We present a unique set of observations where we observed the high density gas tracers HCN, CS, HNC, and $HCO^+$ along with CO and their isotopomers at high resolution and high sensitivity in Arp 220 and NGC 6240. Such an interferometric data set provides an excellent probe into the dense molecular gas cores of these galaxies wherein lie the answers to many questions about star formation and the correlation between starbursts, AGN activity, and merging. We used CARMA to image these galaxies at $2''$ and 0.5 - $0.8''$ resolutions.

Using the Large Velocity Gradient formalism, we derived the molecular hydrogen densities and optical depth at measured brightness temperatures for each of the molecular species. The $H_2$ densities were of the order of $5 \times 10^4$ cm$^{-3}$ for the assumed abundances for each of the molecular species in Arp 220 and $10^4$ cm$^{-3}$ in NGC 6240. The abundances we assumed were taken from observations of Galactic sources. Initially, in the case of HNC, calculations using these assumed abundance (Graninger et al., 2014), resulted in $H_2$ densities 5 times lower than those measured using HCN. In the case of $HCO^+$, the assumed abundance (Acharyya & Herbst, 2015), gave $H_2$ densities an order of magnitude lower than HCN.

This discrepancy leads us to suggest that the abundances we measure for HNC and $HCO^+$ in our galaxy do not hold for ULIRGs such Arp 220 and NGC 6240. The disagreement in the values is probably rooted in the physical conditions in the molecular gas in these galaxies. HNC is preferentially destroyed at higher temperatures in comparison to HCN, and therefore would result in lower abundances of HNC. $HCO^+$ abundances might be diminished as a result of recombination in very dense conditions. In fact, the abundances of these molecular species could be as much 10 times different from Milky Way like galaxies.

Understanding the chemistry of HCN and HNC molecules has allowed theorists to model their behavior in XDR vs PDR regions in galaxies. These models predict a HCN/HNC ratio of less than one in XDR conditions in the molecular gas. We find the ratio in Arp 220 to be significantly less than unity. Arp 220 does not have confirmed X-ray detections of AGN in either nucleus. Our measurement of the HCN and HNC ratio in Arp 220, at both resolutions, strongly indicates an XDR, which is probably being irradiated by an AGN. For the first time, both Arp 220 nuclei show AGN signatures.

In contrast, we did not get indications of an XDR in NGC 6240, which does have two X-ray confirmed AGN. The majority of the nuclear gas lies between the two AGN in NGC 6240 and is

presumably not as irradiated by the AGN. Therefore, the molecular gas does not show XDR conditions in the molecular gas but shows PDR conditions. This indicates that the molecular gas in merging systems go through phases of XDR and PDR conditions as the merger goes through and this changes the abundances in the merging systems with time.

We gratefully acknowledge the assistance of Anneila Sargent for suggestions and improvements on the manuscript. We thank the staff of CARMA for their help with carrying out the observations and calibrations. We thank Marc W. Pound and Peter Teuben for their invaluable help with data reduction. CARMA development and operations were supported by the National Science Foundation grants AST-0838260 and AST-1140063 under a cooperative agreement, and by the CARMA partner universities. We acknowledge student support from NRAO under grants AST-0956545 and AST-0836064. We thank Jin Koda for lending us the LVG modeling code.

# Chapter 6

# Summary

The goal of this thesis has been to better understand the molecular gas properties of two galaxies, the ULIRGs Arp 220 and NGC 6240, that are at different stages of merging. We used CARMA to image these galaxies at 2″ and 0.5 - 0.8″ resolutions. The methods used for observations and reduction of the data are presented in Chapter 2. This unique set of high resolution, high sensitivity observations of gas tracers HCN, CS, HNC, and $HCO^+$ along with CO and their isotopomers provides a new probe of the dense molecular gas cores of these galaxies. Detailed results and analysis of the observations are described in Chapters 3 and 4. Chapter 5 is comprised of a paper that has recently been submitted to the Astrophysical Journal.

Our study of the physical properties of the gas using these high density tracers, applied two level excitation analysis with photon trapping and Large Velocity Gradient formalism and measured the molecular hydrogen densities, optical depth, and temperatures for each of the molecular species. For Arp 220 and NGC 6240, the $H_2$ densities derived from HCN and CS, assuming abundance typical of galactic sources, were of the order of $5 \times 10^4$ cm$^{-3}$ and $10^4$ cm$^{-3}$ respectively. However, adopting the galactic abundace for HNC, resulted in $H_2$ densities 5 times lower than those measured using HCN. In the case of $HCO^+$, the assumed galactic abundance led to $H_2$ densities an order of magnitude lower than HCN.

This discrepancy suggests that the abundances measured for HNC and $HCO^+$ in our galaxy do not apply to ULIRGs such as Arp 220 and NGC 6240. The disagreement in the values is probably rooted in the physical conditions in the molecular gas in these galaxies. HNC is preferentially destroyed at higher temperatures than HCN. This would result in lower abundances of HNC. Similarly, $HCO^+$ abundances might be diminished as a result of recombination in very dense conditions. The abundances of these molecular species could be as much 10 times different from Milky Way-like galaxies.

The molecular gas density of Arp 220 is an order of magnitude higher than that in NGC 6240, although the dynamical masses of the galaxies are similar ($\sim$5 x $10^9$ $M_\odot$ in the disk of NGC 6240 and 2 x $10^9$ $M_\odot$ in each of the rotating disks of Arp 220. This is a strong indicator that the molecular

gas in a galaxy at the merger stage represented by Arp 220 is much denser than a galaxy in a stage represented by NGC 6240. The dust temperatures and hence the kinetic temperatures of these ULIIRGs are comparable at $\sim$ 45 K. However, the excitation temperatures of each of the molecules for Arp 220 are consistently higher than for NGC 6240. Again the differences can be explained by the different merger stages. For similar reasons, optical depths were higher for each of the transitions in NGC 6240 as compared to Arp 220.

We found surprisingly strong and broad HNC and $HCO^+$ emissions in both Arp 220 and NGC 6240. Observing all these lines simultaneously at similar resolutions and sensitivity allowed us to use line ratios as a probe of the physical properties of the molecular gas. In particular modeling the behavior of HCN and HNC molecules may distinguish between XDR and PDR regions in galaxies. An HCN/HNC ratio of less than unity is predicted in XDR conditions. Our measured ratio in Arp 220 is significantly less than unity, strongly indicating an XDR, which is probably being irradiated by an AGN. However,the presence of an AGN has not been confirmed by X-ray observations in either nuclei of Arp 220. This is the first suggestion of AGNs in Arp 220.

In contrast, there were no indications of an XDR in NGC 6240, which does have two X-ray confirmed AGN. Most of the molecular gas lies between the two AGN in NGC 6240 and is presumably not as irradiated by the AGN. The molecular gas, which shows a high level of star forming activity exhibits clear PDR conditions. Evidently, molecular gas in merging systems goes through phases of XDR and PDR conditions as the merger continues changing the abundances with time.

In summary, the molecular gas properties of merging galaxies evolve as the merger proceeds. The physical properties, the abundances, and kinematics are all a function of the merger stage. A deeper and wider study of these properties in mergers in various stages of merging is required to make a more general deduction.

# Bibliography

Aalto, S., Booth, R. S., Black, J. H., & Johansson, L. E. B. 1995, A&A, 300, 369

Aalto, S., Polatidis, A. G., Hüttemeister, S., & Curran, S. J. 2002, A&A, 381, 783

Acharyya, K. & Herbst, E. 2015, ApJ, 812, 142

Anantharamaiah, K. R., Viallefond, F., Mohan, N. R., Goss, W. M., & Zhao, J. H. 2000, ApJ, 537, 613

Bakes, E. L. O. & Tielens, A. G. G. M. 1994, ApJ, 427, 822

Barnes, J. E. & Hernquist, L. 1992, ARA&A, 30, 705

Bergin, E. A., Goldsmith, P. F., Snell, R. L., & Langer, W. D. 1997, ApJ, 482, 285

Bergin, E. A., Snell, R. L., & Goldsmith, P. F. 1996, ApJ, 460, 343

Beswick, R. J., Pedlar, A., Mundell, C. G., & Gallimore, J. F. 2001, MNRAS, 325, 151

Bryant, P. M. & Scoville, N. Z. 1999, AJ, 117, 2632

Caputi, K. I., Lagache, G., Yan, L., Dole, H., Bavouzet, N., Le Floc'h, E., Choi, P. I., Helou, G., & Reddy, N. 2007, ApJ, 660, 97

Casoli, F., Dupraz, C., & Combes, F. 1992, A&A, 264, 55

Clements, D. L., McDowell, J. C., Shaked, S., Baker, A. C., Borne, K., Colina, L., Lamb, S. A., & Mundell, C. 2002, ApJ, 581, 974

Colbert, E. J. M., Wilson, A. S., & Bland-Hawthorn, J. 1994, ApJ, 436, 89

Curran, S. J. 2000, A&AS, 144, 271

Downes, D. & Eckart, A. 2007, A&A, 468, L57

Downes, D. & Solomon, P. M. 1998, ApJ, 507, 615

Dumouchel, F., Faure, A., & Lique, F. 2010, MNRAS, 406, 2488

Engel, H., Davies, R. I., Genzel, R., Tacconi, L. J., Hicks, E. K. S., Sturm, E., Naab, T., Johansson, P. H., Karl, S. J., Max, C. E., Medling, A., & van der Werf, P. P. 2010, A&A, 524, A56

Engel, H., Davies, R. I., Genzel, R., Tacconi, L. J., Sturm, E., & Downes, D. 2011, ApJ, 729, 58

Goldreich, P. & Kwan, J. 1974, ApJ, 189, 441

Goldsmith, P. F., Langer, W. D., Ellder, J., Kollberg, E., & Irvine, W. 1981, ApJ, 249, 524

Graciá-Carpio, J., García-Burillo, S., Planesas, P., & Colina, L. 2006, ApJ, 640, L135

Graninger, D. M., Herbst, E., Öberg, K. I., & Vasyunin, A. I. 2014, ApJ, 787, 74

Greve, T. R., Papadopoulos, P. P., Gao, Y., & Radford, S. J. E. 2009, ApJ, 692, 1432

Güsten, R. 1989, in IAU Symposium, Vol. 136, The Center of the Galaxy, ed. M. Morris, 89

Hirota, T., Yamamoto, S., Mikami, H., & Ohishi, M. 1998, ApJ, 503, 717

Huettemeister, S., Henkel, C., Mauersberger, R., Brouillet, N., Wiklind, T., & Millar, T. J. 1995, A&A, 295, 571

Imanishi, M. & Nakanishi, K. 2006, PASJ, 58, 813

Imanishi, M., Nakanishi, K., & Kohno, K. 2006, AJ, 131, 2888

Imanishi, M., Nakanishi, K., Kuno, N., & Kohno, K. 2004, AJ, 128, 2037

Imanishi, M., Nakanishi, K., Tamura, Y., Oi, N., & Kohno, K. 2007, AJ, 134, 2366

Iwasawa, K., Sanders, D. B., Evans, A. S., Trentham, N., Miniutti, G., & Spoon, H. W. W. 2005, MNRAS, 357, 565

Kohno, K. 2005, in American Institute of Physics Conference Series, Vol. 783, The Evolution of Starbursts, ed. S. Hüttmeister, E. Manthey, D. Bomans, & K. Weis, 203–208

Kohno, K., Matsushita, S., Vila-Vilaró, B., Okumura, S. K., Shibatsuka, T., Okiura, M., Ishizuki, S., & Kawabe, R. 2001, in Astronomical Society of the Pacific Conference Series, Vol. 249, The Central Kiloparsec of Starbursts and AGN: The La Palma Connection, ed. J. H. Knapen, J. E. Beckman, I. Shlosman, & T. J. Mahoney, 672

Komossa, S., Burwitz, V., Hasinger, G., Predehl, P., Kaastra, J. S., & Ikebe, Y. 2003, ApJ, 582, L15

Krips, M., Neri, R., García-Burillo, S., Martín, S., Combes, F., Graciá-Carpio, J., & Eckart, A. 2008, ApJ, 677, 262

Krolik, J. H. & Kallman, T. R. 1983, ApJ, 267, 610

Lahuis, F. & van Dishoeck, E. F. 2000, A&A, 355, 699

Langer, W. D. & Penzias, A. A. 1993, ApJ, 408, 539

Le Floc'h, E., Papovich, C., Dole, H., Bell, E. F., Lagache, G., Rieke, G. H., Egami, E., Pérez-González, P. G., Alonso-Herrero, A., Rieke, M. J., Blaylock, M., Engelbracht, C. W., Gordon, K. D., Hines, D. C., Misselt, K. A., Morrison, J. E., & Mould, J. 2005, ApJ, 632, 169

Lepp, S. & Dalgarno, A. 1996, A&A, 306, L21

Lepp, S. & McCray, R. 1983, ApJ, 269, 560

Lintott, C. & Viti, S. 2006, ApJ, 646, L37

Magnelli, B., Elbaz, D., Chary, R. R., Dickinson, M., Le Borgne, D., Frayer, D. T., & Willmer, C. N. A. 2009, A&A, 496, 57

Maloney, P. R., Hollenbach, D. J., & Tielens, A. G. G. M. 1996, ApJ, 466, 561

McDowell, J. C., Clements, D. L., Lamb, S. A., Shaked, S., Hearn, N. C., Colina, L., Mundell, C., Borne, K., Baker, A. C., & Arribas, S. 2003, ApJ, 591, 154

Meijerink, R. & Spaans, M. 2005, A&A, 436, 397

Meijerink, R., Spaans, M., & Israel, F. P. 2007, A&A, 461, 793

Nakanishi, K., Okumura, S. K., Kohno, K., Kawabe, R., & Nakagawa, T. 2005, PASJ, 57, 575

Paglione, T. A. D., Jackson, J. M., Ishizuki, S., & Rieu, N.-Q. 1995, AJ, 109, 1716

Papadopoulos, P. P. 2007, ApJ, 656, 792

Papadopoulos, P. P., Zhang, Z.-Y., Xilouris, E. M., Weiss, A., van der Werf, P., Israel, F. P., Greve, T. R., Isaak, K. G., & Gao, Y. 2014, ApJ, 788, 153

Pérez-Beaupuits, J. P., Aalto, S., & Gerebro, H. 2007, A&A, 476, 177

Pirogov, L. 1999, A&A, 348, 600

Radford, S. J. E., Delannoy, J., Downes, D., Guélin, M., Guilloteau, S., Greve, A., Lucas, R., Morris, D., & Wink, J. 1991, in IAU Symposium, Vol. 146, Dynamics of Galaxies and Their Molecular Cloud Distributions, ed. F. Combes & F. Casoli, 303

Sakamoto, K., Aalto, S., Wilner, D. J., Black, J. H., Conway, J. E., Costagliola, F., Peck, A. B., Spaans, M., Wang, J., & Wiedner, M. C. 2009, ApJ, 700, L104

Sakamoto, K., Scoville, N. Z., Yun, M. S., Crosas, M., Genzel, R., & Tacconi, L. J. 1999, ApJ, 514, 68

Sanders, D. B., Mazzarella, J. M., Kim, D.-C., Surace, J. A., & Soifer, B. T. 2003, AJ, 126, 1607

Sanders, D. B. & Mirabel, I. F. 1996, ARA&A, 34, 749

Sanders, D. B., Scoville, N. Z., & Soifer, B. T. 1991, ApJ, 370, 158

Sanders, D. B., Soifer, B. T., Elias, J. H., Madore, B. F., Matthews, K., Neugebauer, G., & Scoville, N. Z. 1988, ApJ, 325, 74

Schilke, P., Walmsley, C. M., Pineau Des Forets, G., Roueff, E., Flower, D. R., & Guilloteau, S. 1992, A&A, 256, 595

Scoville, N., Sheth, K., Walter, F., Manohar, S., Zschaechner, L., Yun, M., Koda, J., Sanders, D., Murchikova, L., Thompson, T., Robertson, B., Genzel, R., Hernquist, L., Tacconi, L., Brown, R., Narayanan, D., Hayward, C. C., Barnes, J., Kartaltepe, J., Davies, R., van der Werf, P., & Fomalont, E. 2015, ApJ, 800, 70

Scoville, N. Z., Evans, A. S., Dinshaw, N., Thompson, R., Rieke, M., Schneider, G., Low, F. J., Hines, D., Stobie, B., Becklin, E., & Epps, H. 1998, ApJ, 492, L107

Scoville, N. Z., Evans, A. S., Thompson, R., Rieke, M., Hines, D. C., Low, F. J., Dinshaw, N., Surace, J. A., & Armus, L. 2000, AJ, 119, 991

Scoville, N. Z., Sargent, A. I., Sanders, D. B., & Soifer, B. T. 1991, ApJ, 366, L5

Scoville, N. Z. & Solomon, P. M. 1974, ApJ, 187, L67

Scoville, N. Z., Yun, M. S., & Bryant, P. M. 1997, ApJ, 484, 702

Shirley, Y. L., Evans, II, N. J., Young, K. E., Knez, C., & Jaffe, D. T. 2003, ApJS, 149, 375

Solomon, P. M., Downes, D., & Radford, S. J. E. 1992a, ApJ, 387, L55

—. 1992b, ApJ, 398, L29

Solomon, P. M., Downes, D., Radford, S. J. E., & Barrett, J. W. 1997, ApJ, 478, 144

Stacey, G. J., Townes, C. H., Geis, N., Madden, S. C., Herrmann, F., Genzel, R., Poglitsch, A., & Jackson, J. M. 1991, ApJ, 382, L37

Tacconi, L. J., Genzel, R., Tecza, M., Gallimore, J. F., Downes, D., & Scoville, N. Z. 1999, ApJ, 524, 732

Tecza, M., Genzel, R., Tacconi, L. J., Anders, S., Tacconi-Garman, L. E., & Thatte, N. 2000, ApJ, 537, 178

Tielens, A. G. G. M. & Hollenbach, D. 1985, ApJ, 291, 722

Turner, B. E. & Thaddeus, P. 1977, ApJ, 211, 755

Usero, A., García-Burillo, S., Fuente, A., Martín-Pintado, J., & Rodríguez-Fernández, N. J. 2004, A&A, 419, 897

van der Tak, F. F. S., Black, J. H., Schöier, F. L., Jansen, D. J., & van Dishoeck, E. F. 2007, A&A, 468, 627

Veilleux, S., Kim, D.-C., & Sanders, D. B. 2002, ApJS, 143, 315

Wang, M., Henkel, C., Chin, Y.-N., Whiteoak, J. B., Hunt Cunningham, M., Mauersberger, R., & Muders, D. 2004, A&A, 422, 883

Wilson, C. D., Harris, W. E., Longden, R., & Scoville, N. Z. 2006, ApJ, 641, 763

Wolfire, M. G., Hollenbach, D., & Tielens, A. G. G. M. 1989, ApJ, 344, 770